EFFECTS OF FUEL TYPE ON THE SAFETY CHARACTERISTICS OF A SODIUM COOLED FAST REACTOR

A Thesis
Presented to
The Academic Faculty

by

Tyler Sumner

In Partial Fulfillment
of the Requirements for the Degree
Doctor of Philosophy in
Nuclear Engineering

Woodruff School of Mechanical Engineering
Georgia Institute of Technology
December 2010

EFFECTS OF FUEL TYPE ON THE SAFETY CHARACTERISTICS OF A SODIUM COOLED FAST REACTOR

Approved by:

Dr. S. M. Ghiaasiaan, Advisor
Woodruff School of Mechanical Engineering
Georgia Institute of Technology

Dr. Weston M. Stacey
Nuclear and Radiological Engineering
Georgia Institute of Technology

Dr. Hamid Garmestani
School of Materials Science and Engineering
Georgia Institute of Technology

Dr. C. K. Wang
Nuclear and Radiological Engineering
Georgia Institute of Technology

Dr. Bojan Petrovic
Nuclear and Radiological Engineering
Georgia Institute of Technology

Dr. John Zino
Nuclear Energy
GE-Hitachi

Date Approved: November 15, 2010

ACKNOWLEDGMENT

I wish to thank my advisor, Dr. Ghiaasiaan, for all his help throughout this project and providing me the opportunity to do it. I would also like to thanks the other members of my committee, Dr. Zino from General Electric and Dr. Petrovic, Dr. Wang and Dr. Garmestani from Georgia Tech. I want to especially thank Dr. Stacey for everything he has done since I started grad school. Special thanks to Dr. van Rooijen for his help in the beginning stages of this project. A big thanks goes out to Chris Sommer for helping me work through ideas, even the bad ones, for the past four years. Finally and most importantly I want to thanks my parents for their continued support and encouragement and always being there for me.

TABLE OF CONTENTS

LIST OF TABLES

LIST OF FIGURES

LIST OF SYMBOLS

Notations

t	Time	64
v	Velocity	20

Superscripts

G	Group g	17
$melt$	Melting	65
$*$	Bulk interface mass transfer	20
$'$	Wall interface mass transfer	20

Subscripts

B	Boron	19
$cool$	Coolant	65
f	Liquid phase	20
g	Vapor phase	20
i	Region i	17
j	Region j	17
k	Subgroup k	17
l	Region l	18
n	Legendre order	18
t	Total	18
x	Cross-section type	17
X	Coordinate direction	20

Abbreviations

ACS	Auxiliary Cooling System	13
ANS	American Nuclear Society	53
$ALMR$	Advanced Liquid Metal Reactor	12
BOC	Beginning of Cycle	13
DF	Driver fuel	59
DFR	Dounreay Fast Reactor	4
DOE	Department of Energy	12
EBR	Experimental Breeder Reactor	4
EM	Electromagnetic pump	13
EOC	End of Cycle	13
GE	General Electric	12
GEM	Gas Expansion Module	33
GFR	Gas-Cooled Fast Reactor	1
IB	Internal blanket	59
IHX	Intermediate Heat Exchanger	13
IFR	Integral Fast Reactor	51
$LMFR$	Liquid Metal Fast Reactor	1
$LOFA$	Loss of Flow Accident	15
$LOHSA$	Loss of Heat Sink Accident	15
$LOHSA-SL$	Loss of Heat Sink Accident of Secondary Loop	67
$LOPA$	Loss of Power Accident	67
MOC	Middle of Cycle	13
ODS	Oxide Dispersion Strengthened steel	43
$PRISM$	Power Reactor Innovative Small Module	12
RB	Radial blanket	59
ΔRFT	Relative fuel temperature increase	65

$RVACS$	Reactor Vessel Auxiliary Cooling System	13
$S-PRISM$	Super Power Reactor Innovative Small Module	11
$SHRS$	Shutdown Heat Removal System	13
$TOPA$	Transient Over Power Accident	15
TRU	Transuranics	32
$UTOPA$	Unprotected Transient Over-Power Accident	72

SUMMARY

A series of accident simulations were performed using INL's thermal hydraulics code RELAP5-3D to analyze steady-state and transient behavior of a sodium cooled fast reactor. The reactor chosen for this study was General Electric's S-PRISM, which is a 1,000 MWt pool-type sodium-cooled fast reactor, designed for either an Oxide or Metal fueled core. Once key core characteristics including power profiles, reactivity feedback coefficients and delayed neutron parameters were calculated, S-PRISM was redesigned for a Nitride fueled core to take advantage of the Nitride fuel's high thermal conductivity and melting temperature. Loss of flow, loss of heat sink, loss of power and inadvertent control rod withdrawal accidents were simulated for each core at beginning, middle and end of cycle to determine if one fuel type provides significant safety advantages over the others.

CHAPTER I

INTRODUCTION

The design and production of fast reactors represents one of the next major steps in the area of nuclear energy generation. The first fast reactor, CLEMENTINE was built in 1946 in Los Alamos, NM., and since then, more than 20 fast reactors have been built and operated, providing over 300 reactor-years of operating experience. Fast reactors offer distinct advantages over the more traditional light water nuclear reactors. For example, the fission-to-capture ratio of the actinides is higher for fast neutron energies than thermal neutron energies allowing for the destruction of long-lived transuranics such as neptunium, americium and curium, which dominate the radiotoxicity of spent nuclear fuel. Fast reactors can function as breeder or burner reactors, utilizing spent fuel from thermal reactors and they are capable of operating on a closed fuel cycle minimizing the amount of high level waste generation. Fast reactors also have technical challenges to overcome including material radiation damage and proliferation risk.

Interest in fast reactors has increased recently due to the possibility of operating on a closed fuel cycle. Of the six reactor technologies selected by the Generation IV International Forum, three are fast reactors and a fourth can operate on a fast or thermal spectrum [3]. These designs include a Gas-Cooled Fast Reactor (GFR), a Supercritical-Water-Cooled Reactor and two Liquid Metal Fast Reactors (LMFR).

Among the various fast reactor designs, Liquid Metal Fast Reactors show the most promise for safe and sustained energy generation. Various coolants have been proposed with sodium being the most popular. Sodium-cooled fast reactors operate at near atmospheric pressures and higher coolant temperatures, allowing for greater

thermal efficiencies. However, sodium-cooled fast reactors require a second sodium loop to prevent activated sodium from contaminating water in the steam generator and also to prevent sodium-water reactions in the primary loop.

Although there is considerable interest and experience with LMFRs, several aspects of the design and safety of these reactors have not been sufficiently studied and require further investigation. One major area of research that requires attention is the fuel type. Two fuel types have been successfully utilized, oxide and metal, and a third, nitride fuel, appears to be feasible. However, it has not been determined whether any of these fuel types provide superior safety characteristics over the others in LMFRs. The purpose of this study is to examine the impact of the fuel type on the inherent safety characteristics of a Liquid Metal Fast Reactor.

CHAPTER II

BACKGROUND

High fluxes, burn-ups, power densities and temperatures are all characteristics of fast reactors that make the selection of materials more important than in traditional thermal reactors. Fuel materials must be able to withstand the high flux of extremely energetic neutrons while providing adequate safety characteristics over the lifetime of the reactor. To keep fast reactors economical compared to thermal reactors, high burn-ups must be employed leading to concerns over radiation damage. Major aspects of fast reactors will be discussed in the forthcoming paragraphs.

2.1 Coolant

Many coolants have been proposed for fast reactors including a variety of liquid metals such as sodium, sodium-potassium, mercury, bismuth, lead and lead-bismuth. The choice of coolant is important to minimize neutron moderation and parasitic absorption and to remove heat adequately. Mercury, bismuth, lead and lead-bismuth are often discarded because of their high densities, which require large mass flow rates and thus large pumping powers. On the other hand, it can be shown that natural circulation is improved with a more dense coolant [44]. Because potassium is a strong neutron absorber, sodium-potassium is generally discarded as well, leaving sodium as a leading coolant for fast reactor systems. Steam is often ruled out as a coolant mostly due to its corrosive properties and issues related to high pressures.

Sodium, the coolant most often used in fast reactors, provides excellent thermal properties and is compatible with many standard cladding materials. Sodium can operate at temperatures near 800 K, approximately 200 K greater than traditional

thermal reactors leading to higher steam temperatures and thus higher thermal efficiencies. However, sodium has a few disadvantages that must be considered. First, sodium's melting temperature is high (371 K), so the reactor must include heaters in the sodium loops to prevent freezing during down periods. Second, sodium activation necessitates an intermediate coolant loop to prevent radioactive contamination of the steam generator from occurring [46]. Finally, sodium reacts violently with water and air requiring stronger coolant flow pipes and reactor vessels.

2.2 Fuel Type and Reactivity Control

Early liquid metal fast reactor designs in the U.S. tended to use metallic fuel because of its compatibility with sodium. Metallic fuel has been successfully used in the Fermi-I reactor, the Dounreay Fast Reactor (DFR) in the U.K and both EBR-I and EBR-II (Experimental Breeder Reactor). More recent fast reactor designs throughout the world such as Phénix, Super-Phénix, Monju and Joyo have favored oxide fuel [4].

When considering which fuel type to choose for an LMFR, a few key differences should be examined. For example, how good is the thermal conductivity, what is the melting temperature, what natural feedbacks does the fuel provide, does one fuel provide better natural circulation characteristics. A desired feature of the fuel type is that an increase in the fuel temperature leads directly to a prompt negative reactivity feedback. A high density fuel is also desirable to improve heat transfer characteristics as well as increase the fuel ratio

Reactivity control is extremely important in fast reactors where the benefits of delayed neutrons are less than in thermal reactors. Delayed neutrons are born at lower energies than prompt neutrons. At these lower energies the importance of delayed neutrons to k_{eff} is lower and these neutrons are more likely to be absorbed rather than to fission, thus diminishing their contribution to reactivity control in the reactor. The delayed neutron problem is compounded further if Pu^{239} or U^{233} is substituted

for U^{235} because Pu^{239} and U^{233} have delayed neutron fractions nearly three times smaller than U^{235}. Due to higher enrichments of fissile isotopes, fast reactors have less fertile isotopes, which often have extraordinarily high delayed neutron fractions. All of these factors contribute to a smaller delayed neutron fraction in a fast reactor providing a smaller margin to prompt criticality than in a thermal reactor.

Because control rod mechanisms are too slow to counter the effects of accidentally reaching supercriticality, prompt reactivity feedback effects must exist to prevent rapid power increases. There are three major reactivity feedback effects to consider when examining fast reactors: Doppler, coolant thermal expansion, and core expansion. As temperatures increase in the reactor, the thermal motion of nuclei increase, altering the nuclei motion relative to impinging neutrons and changing the cross-section that neutrons experience. This phenomenon is referred to as the Doppler effect. Doppler broadening of cross-sections is of much importance for neutron fluxes in the resonant energy regions; as these cross-sections broaden, their corresponding reaction rates will increase. In softer neutron spectra, more neutrons are in the resonant energy range and are more likely to see Doppler broadened cross-sections. Thus, softer spectra provide larger Doppler reactivity feedback effects.

As the temperature of the coolant, most likely sodium for fast reactors, increases during a transient, the coolant becomes less dense and four primary reactivity effects occur: spectrum hardening, increased leakage, elimination of sodium parasitic absorption and changes in energy self-shielding in the flux. Decreasing coolant density leads to decreased neutron moderation and thus more energetic neutrons. Because the number of neutrons released per fission increases with increasing energy, this effect leads to a positive reactivity insertion. With less coolant in the flow channels, however, neutrons are more likely to stream out of the core leading to a negative reactivity insertion. The reactivity feedbacks from a reduction of parasitic absorption and changes in energy self-shielding are not usually very significant. Because neutron

leakage is not a significant factor in the center of the core, coolant thermal expansion is generally positive in the inner regions of the reactor. The leakage component of coolant thermal expansion tends to dominate at the edges of the reactor leading to negative reactivity insertions. Something that must also be considered is that the spectral hardening due to coolant thermal expansion leads to less effective Doppler feedback.

The third major reactivity feedback effect is axial and radial expansion of the reactor core. Increasing fuel temperatures in the reactor result in fuel pin growth and an increase in the reactor's height. A taller reactor will have more radial leakage, which leads to a negative reactivity feedback effect. The reactivity feedback due to radial expansion of the core is a function of the temperature of the structural material holding the fuel assemblies in place. As the temperature of the grids holding the assemblies in place increases, the assemblies will move radially outward, increasing axial neutron leakage in the core.

Metallic fuels have very low melting temperatures compared with nitride and oxide fuels, generally lower than 1,500 K depending on the alloy. However, a very high thermal conductivity, on the order of 20 $W/m \cdot K$, leads to fairly low fuel centerline temperatures [10]. Because the fuel is composed of heavy metal, the fuel provides little moderation for the neutrons and thus a very hard spectrum. A hard spectrum is important in Fast Reactors to increase the breeding gain in fertile material, providing more fuel for the reactor. But a harder neutron spectrum also leads to decreased Doppler feedback effects due to fewer neutrons at resonant energies. One effect to compensate for the lack of Doppler feedback in metallic cores is axial expansion of the fuel.

Pin swelling in metallic fueled fast reactors due to irradiation is also an important consideration. As metallic fuel undergoes irradiation in a fast spectrum, vacancies are formed when atoms are knocked out of their lattice positions by fast neutrons.

These vacancies tend to migrate together forming fission gas bubbles in the fuel pin. It is difficult for the fission gas to escape metal fuels leading to swelling of the fuel pin. As the pin expands radially, it comes in contact with and increases the stresses on the cladding.

According to Reference [10], experience with metal fuels has demonstrated that up to 20% atomic burn-up is feasible under normal operating conditions if ferritic-martensitic stainless steel or modified-austenitic stainless steel alloys are used as cladding. EBR-II's Mark-IIIA driver fuel was only qualified up to 10% atomic burn-up; however, some assemblies were able to reach burn-ups between 15 and 19% without breach of the cladding or fission gas release [10]. Fast reactor design experience has led to the conclusion that increasing the radial gap between the cladding and the fuel can increase burn-up limits by allowing for greater fuel swelling before contacting the cladding.

The robustness of metallic fuel has been demonstrated by the numerous transients simulated during EBR-II safety tests including 40 start-ups and shutdowns, five 15% overpower transients, three 60% overpower transients and 45 loss of flow and loss of heat sink full power tests without scram [10]. Due to the compatibility of metal fuels with sodium, several EBR-II fuel pins operated successfully and safely in the reactor for 223 days after cladding breach without expansion of the breach site or damage to surrounding fuel pins or assemblies [10]. Metal fuel has consequently been concluded to be very reliable.

Oxide fuels have poor thermal conductivities, on the order of 5 $W/m \cdot K$, which lead to high fuel centerline temperatures. This is compensated for by a very high melting temperature that is greater than 3,000 K. The presence of oxygen in the fuel leads to increased moderation and a softer spectrum than in metallic cores. Due to higher fluxes in the resonant energies, oxide fuels tend to have a larger Doppler reactivity feedback providing an immediate response to transients producing temperature

changes in the fuel.

Cracking in oxide fuel due to irradiation leads to easier release of fission gas than in metallic fuel and significantly decreases the amount of fuel swelling compared to metallic fuel. The movement of grain boundaries, which results in cracking of the fuel, ultimately is what leads to structurally unsound fuel pins and is the limiting factor for oxide fuel burn-up.

Restructuring of the fuel pin due to irradiation must also be considered in an oxide fueled system as the formation of a central void region leads to changes in the thermal conductivity and density of the fuel. Central void regions form in only a few hours after start-up as the grain boundaries in the fuel shift. This central void region creates a convenient annular shape that allows the fission gas to easily vent into the upper or lower plenums. With minimal swelling of the fuel pin, the stress on the cladding is also lower than in metal fueled systems.

One major drawback to oxide fuels is its incompatibility with sodium, requiring very strong cladding materials. Unlike metal fueled cores which can withstand several fuel pin breaches, cladding failure in oxide systems can lead to violent chemical reactions between the fuel and the coolant. Because of this, reactor designers must ensure careful detection of fission product release into the coolant.

Nitride fuels have been given significantly less attention than metallic and oxide fuels but have some interesting characteristics. Due to the presence of only one moderating atom per heavy metal atom, the spectrum of nitride fuels tends to be harder than oxide fuels yet softer than metallic fuels, which leads to better breeding ratios than in oxide fuels. Nitride fuels are also chemically compatible with sodium eliminating the immediate risk of breached cladding that exists with oxide fuel.

Nitride fuels have very good thermal conductivity, generally listed at greater than 15 $\mathrm{W/m \cdot K}$, which is higher than for oxide fuels, though not quite as good as metallic fuels [27]. High densities are also possible in nitride fuels. According to Reference

[27], the theoretical density of uranium nitride is 14.32 g/cm^3, slightly lower than for metallic fuel but considerably higher than oxide fuel. Due to the limited interest in nitride fuels, reports of its melting temperature vary but most reports list melting temperatures at or above 2,800 K [49, 20].

Fission gas in nitride fuels tends to behave more similarly to metal fuel than oxide fuel with trapped fission gas bubbles that result in swelling. Reference [42] lists the volumetric swelling rates for two similar nitride fuel pins as 1.6 and 1.8% / % burn-up. Burn-up limits in nitride fuels are not well established but lower swelling rates than in metallic fuel should lead to higher burn-up limits.

The major area of concern for nitride fuels is the (n, p) reaction that N^{14}, which represents 99.6 % of natural nitrogen, undergoes to produce C^{14}, which has a half-life of 5,730 years and poses spent fuel radiotoxicity concerns [37]. N^{15} can also produce C^{14} via an (n,d) reaction but N^{15}'s C^{14} producing cross section is five times smaller than N^{14} [40]. In addition to the production of C^{14}, several other aspects must be considered to determine the proper nitrogen enrichment level. First, it is very expensive to enrich the N^{15} concentration of nitrogen. Second, the neutron spectrum for N^{14} is softer than for N^{15} due to N^{14}'s large absorption cross section resulting in diminished breeding potential. This large absorption cross section, however, results in a stronger Doppler feedback for fuel with lower N^{15} enrichments.

While metallic and oxide fast reactor fuels have been successfully developed and utilized, the technology to develop adequate nitride fuel is not at the same level. Aside from the costly N^{15} enrichment process, many current production techniques result in carbon and oxygen concentrations that are too high in nitride fuels [37]. Several fabrication processes are currently being researched, such as Spark Plasma Sintering, and show promise to produce viable fast reactor nitride fuel [37]. Although there have not been any high power level, nitride-fueled fast reactors built, several reactor systems have been investigated and proposed such as the one in Reference

[20].

Other fuel types have shown potential for fast reactor systems such as carbide and sulphide fuels. Carbide fuels have higher thermal conductivities than oxide fuels but they react in a non-favorable way with the cladding after irradiation of the fuel. Sulphide fuels have similar properties to carbide fuel; however, sulphide fuel's density is comparable to oxide fuel [46].

CHAPTER III

OBJECTIVES AND APPROACH

The purpose of this investigation is to examine the impact of the fuel type on the inherent safety characteristics of LMFRs. To perform this study, the responses to various transient conditions were examined for metallic, oxide and nitride cores of a baseline LMFR. For a proper comparison, the baseline LMFR should have the same power level, be approximately the same size and have the same heat removal system for all three fuel types. The goal was to discover whether one fuel type is superior to the others to provide a more complete understanding of fuel options for future LMFRs.

3.1 Simulation of S-PRISM as Baseline LMFR

The reactor chosen for this investigation should be representative of current fast reactor technology and have the potential for oxide, metal or nitride fueled cores. Because of the vast experience with sodium as well as its excellent thermal properties, a sodium-cooled fast reactor was used for this study. Previous fast reactors have operated at powers from as low as a few MWe up to more than 1,000 MWe, the latter for Super-Phénix. But the vast majority of fast reactors have had powers of a few hundred MWe; therefore, for this study a reactor with a medium power level was chosen. General Electric's S-PRISM design fits the above criteria and was the reference reactor selected for this study.

In 1980, General Electric (GE) initiated the design of its PRISM (Power Reactor Innovative Small Module) reactor, the precursor to GE's S-PRISM. PRISM was selected as the basis for the Department of Energy's (DOE) Advanced Liquid Metal Reactor (ALMR) in 1988. PRISM is a pool-type sodium-cooled fast reactor that

utilizes passive cooling for decay heat removal. Using a modular design with three reactor modules per standard 465 MWe power block, an overall plant net electrical rating of 1,395 MWe is achievable for three power blocks [23]. PRISM's metallic fuel is composed of Plutonium and depleted Uranium obtained from spent light water reactor (LWR) fuel and has a residence time of approximately six years in the reactor.

GE's S-PRISM, or Super-PRISM, is similar to PRISM in that it is a pool-type sodium-cooled fast reactor. Each S-PRISM power block contains two 1,000 MWt reactors connected to a single steam generator. One S-PRISM power block produces 760 MWe. In keeping with the key ALMR features, S-PRISM also boasts passive reactor shutdown, passive shutdown heat removal, and passive reactor cavity cooling [8].

S-PRISM has been designed with two different cores, an Oxide and a Metal core, that are interchangeable and both produce 1,000 MWt. This allows the two cores to operate with the same heat removal system. The Oxide core has 162 driver fuel assemblies, 73 internal blanket assemblies and 60 radial blanket assemblies. The Metal core has 138 driver fuel assemblies, 49 internal blanket assemblies and 48 radial blanket assemblies. The internal blanket assemblies protect against reactivity loss during burn-up. Driver Fuel assemblies in the Oxide core have 217 fuel pins in a triangular pitch array at an outer diameter (OD) of 7.059 mm while the Metal core has 271 pins per assembly at an OD of 5.477 mm. S-PRISM's cladding is composed of HT9(m) stainless steel. In both cores, sodium enters the core at 636 K and leaves the core at 783 K.

Figure 1 illustrates the sodium flow path through S-PRISM's containment vessel. Inside the reactor closure are two 500 MWt intermediate heat exchangers (IHX) and four electromagnetic pumps (EM) that circulate the sodium in the primary loop throughout the pool. Sodium enters the hot leg of the IHX at 758 K while sodium in the intermediate loop enters the cold leg of the IHX at 598 K. Non-radioactive

sodium circulates through the two intermediate loops to a single 1,000 MWt steam generator.

For decay heat removal S-PRISM uses two safety grade auxiliary cooling systems: the Reactor Vessel Auxiliary Cooling System (RVACS) and the Auxiliary Cooling System (ACS) that together make up S-PRISM's Shutdown Heat Removal System (SHRS). Both the RVACS and ACS utilize natural circulation of the coolant in the primary loop but heat is transferred to naturally circulating air in the RVACS while the ACS transfers heat from the primary sodium into the IHX.

The first step in this investigation was modeling and simulating the two different S-PRISM cores and verifying the models against previously published material on the reactor. This entailed proper modeling of the power profile in the core as well as the thermodynamic properties of the reactor. Information on S-PRISM is available for beginning of cycle (BOC) calculations; however, it is important to compare how transients progress at various stages of the fuel cycle. Therefore, estimations were made for the fuel compositions during a single batch in the equilibrium fuel cycle. Calculations were then performed to determine middle of cycle (MOC) and end of cycle (EOC) core properties for the transient simulations.

3.2 Redesigning S-PRISM for Alternative Fuel Types

After simulating the Oxide and Metal S-PRISM cores, S-PRISM was redesigned for a Nitride core, taking care to maintain key S-PRISM characteristics so that differences in transient progressions could be attributed directly to the fuel material. In the core redesign, the Nitride core produced 1,000 MWt and the remainder of the primary loop and Nuclear Steam Supply System remained unchanged. The same sodium mass flow rate was used to keep the demand on the pumps as constant as possible. As with the Metallic and Oxide cores, basic fuel cycle calculations for the Nitride core were made to determine the reactor's response to various transients at different points in

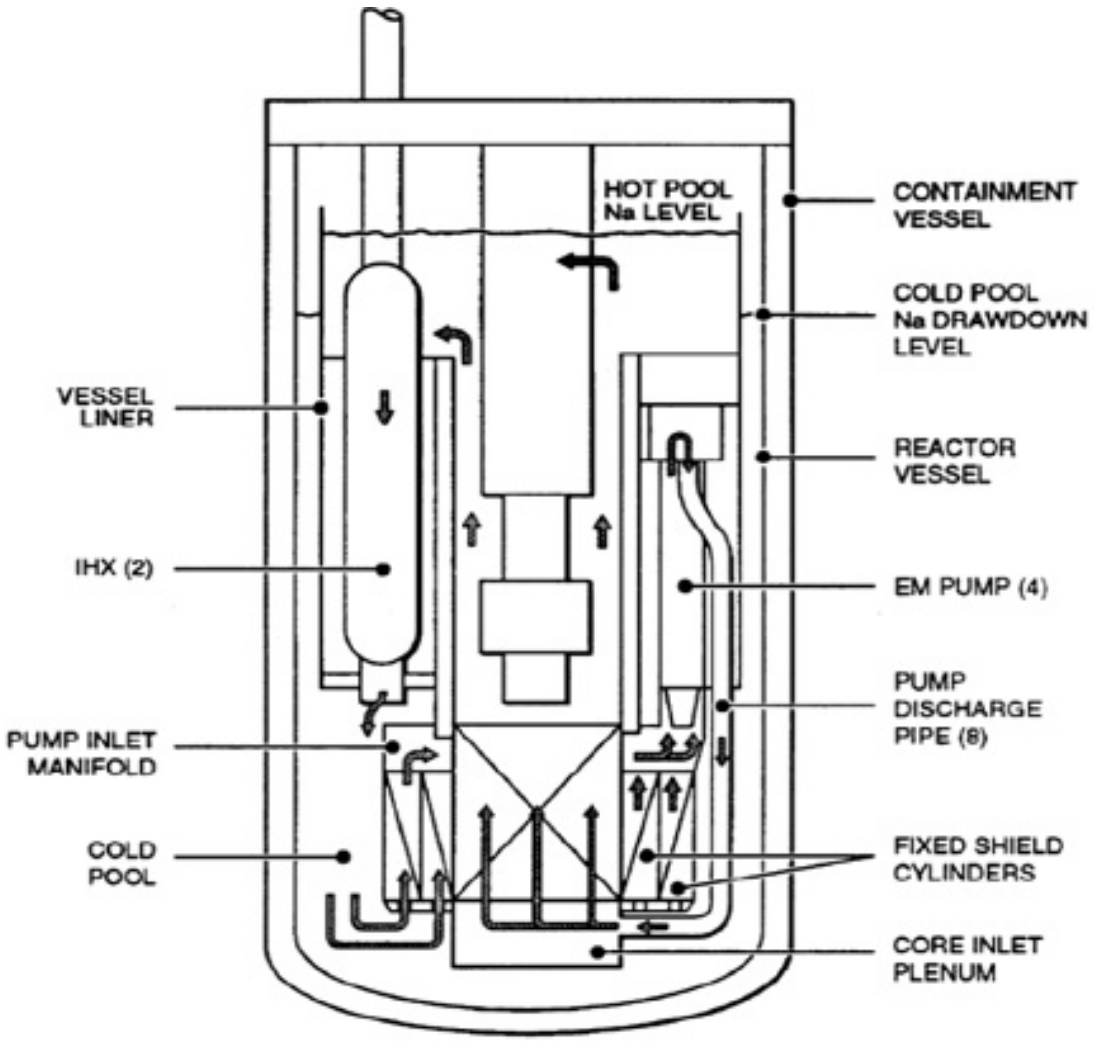

Figure 1: Sodium flow path through S-PRISM primary loop [14]

the fuel cycle.

3.3 Transients to be Simulated

This investigation focused primarily on the simulation of three types of transients:

- Loss of Flow Accident (LOFA)
- Transient Over Power Accident (TOPA), and
- Loss of Heat Sink Accident (LOHSA)

These transients were simulated for all three S-PRISM cores and the response to the transients for each core were analyzed based on the occurrence of fuel or clad melting, the length of time before critical damage to the reactor occurs, the increase or decrease of core power, and also the maximum temperature that various core components reach. A critical analysis of the differences between the simulations for each of the three cores provided a better understanding of the impact that the choice of fuel has on the safety properties of sodium-cooled fast reactors. In addition, several protected accidents were simulated to examine the effect that the various fuel types have on reactor shut down and natural circulation in the core.

CHAPTER IV

COMPUTATIONAL TOOLS

To perform the simulations required for this investigation, two primary computer codes were used: ERANOS 2.0 and RELAP5-3D/ATHENA. The ERANOS 2.0 package includes nuclear data libraries based on the JEF-2.2 nuclear data library; ECCO, a cell and lattice code; deterministic flux solvers; a burn-up module; and perturbation theory and sensitivity analysis tools. ERANOS was used to calculate power distributions, fuel burn-up and reactivity feedbacks from a 3-dimensional model of S-PRISM's various cores with homogenized fuel assemblies. Once the power distribution and various reactivity feedback effects in S-PRISM were determined, the data was input into INL's RELAP5-3D for thermal hydraulic analyses of the steady-state and transient behavior of the different S-PRISM fueled-cores.

4.1 ERANOS 2.0

CEA's European Reactor Analysis Optimized calculation System, ERANOS, was developed and validated for neutronic calculations of both thermal and fast reactor systems. The deterministic code and data system includes all the necessary tools to function as a stand alone code to model and analyze the neutronic behavior of nuclear reactors. It includes the capability to model traditional light water cores as well as advanced reactor systems such as Gas Cooled Fast Reactors, Accelerator Driven Systems and Liquid Metal Fast Reactors. A modular coding structure allows the user to link various modules together to perform various calculation routes to fit the user's speed and accuracy requirements [32].

Cross-section libraries in ERANOS 2.0 have been generated from the JEF-2.2 cross-section evaluation. The JEF-2.2 evaluation was processed for use in ERANOS

2.0 using the NJOY and CALENDF codes to produce appropriate subgroup parameters that accurately reflect the resonance cross-sections of nuclear materials. To produce problem specific cross-sections, which is very important for fast reactors due to complex geometries, ERANOS 2.0 uses the cell code ECCO to account for the neutron streaming and resonance self-shielding effects in the core and generate properly averaged multigroup cross-sections.

Using a 2-D model of the subassemblies in the reactor, ECCO uses a combination of a slowing down treatment over many groups with the subgroup method within each fine group to generate these cross-sections. For the most important nuclides, ECCO has 1,968 fine groups and it uses broader groups, either 33 or 172, for the less important nuclides [31]. ECCO uses the following formula to generate the effective group cross-section $\tilde{\sigma}_{xi}^{g}$ for region i in group g:

$$\tilde{\sigma}_{xi}^{g} = \frac{\sum_{j} S_j^g \sum_{k} \alpha_k^g \sigma_{x_k}^g P_{ij}\left(\Sigma_{t_k}^g\right)}{\sum_{j} S_j^g \sum_{k} \alpha_k^g P_{ij}\left(\Sigma_{t_k}^g\right)} \tag{1}$$

where x can be for capture, fission, elastic, inelastic or total cross-sections of Legendre order zero. S_j^g represents the source term in group g of region j, α_k^g is the probability for each partial cross section in group g. $P_{ij}(\Sigma_{t_k}^g)$ is the reduced collision probability between regions i and j for subgroup k within group g and $\Sigma_{t_k}^g$ is the total group macroscopic cross section in each region. [31].

For total cross sections of Legendre order one in region i, which require a current weighting, Equation 2 is used [31].

$$\tilde{\sigma}_{t_{1i}} = \frac{\sum_{j} S_j \sum_{k} \alpha_k \sigma_{t_{lk}} \sum_{l} P_{il}\left(\Sigma_{t_k}\right) P_{lj}\left(\Sigma_{t_k}\right)}{\sum_{j} S_j \sum_{k} \alpha_k \sum_{l} P_{il}\left(\Sigma_{t_k}\right) P_{lj}\left(\Sigma_{t_k}\right)} \tag{2}$$

The self-shielded cross-sections are used to calculate the flux and current for the system. Cross-sections in the prescribed group structure are then produced by collapsing

the self-shielded cross-sections and smearing them over each subassembly.

To perform the reactor core calculations, ERANOS utilizes a variational nodal method transport code called VARIANT, which is based on the second-order form of the even-parity transport equation [32]. The P_n transport calculations in VARIANT can be of order 1, 3 or 5 where $n = 1$ is diffusion theory [11]. The VARIANT calculations generate a flux profile as well as calculate the reactivity of the core and the reactivity swing due to burn-up in conjunction with the depletion module EVOLUTION [33]. Finally, the S_n transport module, BISTRO, can be used to calculate the effective delayed neutron fraction and various reactivity feedbacks such as the sodium thermal expansion reactivity worth.

4.2 RELAP5-3D/ATHENA

RELAP5-3D is the product of decades of research and development related to the simulation and safety analysis of nuclear reactor systems. It is capable of simulating the coupled behavior of a nuclear reactor core and its coolant system for a vast number of postulated transients such as loss of coolant or flow and anticipated transient without scram. RELAP5-3D includes a variety of liquids and vapors such as light and heavy water, helium, hydrogen, nitrogen and many others. The ATHENA version of the code includes many other fluids that were not available in previous versions of RELAP5-3D such as liquid metals including sodium. The RELAP5-3D/ATHENA package has been extensively tested and is capable of modeling the steady-state and transient behavior and interaction between fluids and heat structures that are of interest to this investigation.

Models in RELAP5-3D can include coolant flow channels, pumps, turbines, plant control systems and condensers as well as heat structures representing fuel pins, heat exchanges and other structural reactor components in multiple coolant loops. Power levels in the reactor can be user-input or modeled with either point kinetic or full

3-D kinetics. The RELAP code system was developed primarily to analyze transients and accidents in light water systems but recent additions to the code have made it a valuable tool for analyzing fast systems, specifically those cooled by liquid metals [16].

RELAP5-3D's code structure uses subroutines in a modular fashion. The three main top level blocks are used to process input data, perform the steady-state and transient calculations and extract the important data from the simulation for outputting. Inside the transient calculation subroutine are modules that calculate heat transfer across the solid structures, advance the hydrodynamic model simulation and calculate the transient response of the reactor power to hydrodynamic state changes [16].

RELAP5-3D's thermal hydraulic model uses eight primary independent state variables: pressure (P), void fraction (α_g), gas and liquid phase internal energy (U_g and U_f), noncondensable quanlity (χ_n), gas and liquid phase velocities (v_g and v_f) and boron density (ρ_B). Distance and time are the independent variables used in RELAP5-3D's solution scheme. To solve for the primary variables, a semi-implicit numerical solution scheme is utilized for eight field equations. These equations are two phasic mass continuity equations, two phasic energy continuity equations, two phasic momentum continuity equations, an equation to calculate the noncondensable quantity and finally a boron transport equation. The continuity equations listed below can be found in Reference [16].

Equations 3 and 4 are the governing equations to calculate the vapor and liquid masses of the various fluids in the system:

$$\frac{\partial}{\partial t}\left(\alpha_g \rho_g\right) + \frac{1}{A}\frac{\partial}{\partial x}\left(\alpha_g \rho_g v_g A\right) = \Gamma_g \tag{3}$$

$$\frac{\partial}{\partial t}\left(\alpha_f \rho_f\right) + \frac{1}{A}\frac{\partial}{\partial x}\left(\alpha_f \rho_f v_f A\right) = \Gamma_f \tag{4}$$

where ρ is the density, v is the velocity and Γ is the volumetric exchange rate. Note that in the absence of mass sources and sinks, mass continuity requires that the liquid mass generation in a volume be the opposite of the vapor mass generation term.

The equations to calculate the vapor and liquid internal energies are shown below in Equations 5 and 6. In these equations, P is the pressure of the volume, Q is the volumetric heat addition rate, $DISS$ is the energy dissipation term associated with wall friction, pump and turbine effects and h^* and h' are the specific enthalpies associated with bulk and wall interface mass transfer [16].

$$\begin{aligned}\tfrac{\partial}{\partial t}\left(\alpha_g\rho_g U_g\right)+\tfrac{1}{A}\tfrac{\partial}{\partial x}\left(\alpha_g\rho_g U_g v_g A\right)=-P\tfrac{\partial\alpha_g}{\partial t}-\tfrac{P}{A}\tfrac{\partial}{\partial x}\left(\alpha_g v_g A\right)\\ +Q_{wg}+Q_{ig}+\Gamma_{ig}h_g^*+\Gamma_w h_g^{'}+DISS_g\end{aligned} \tag{5}$$

$$\begin{aligned}\tfrac{\partial}{\partial t}\left(\alpha_f\rho_f U_f\right)+\tfrac{1}{A}\tfrac{\partial}{\partial x}\left(\alpha_f\rho_f U_f v_f A\right)=-P\tfrac{\partial\alpha_f}{\partial t}-\tfrac{P}{A}\tfrac{\partial}{\partial x}\left(\alpha_f v_f A\right)\\ +Q_{wf}+Q_{if}+\Gamma_{if}h_f^*+\Gamma_w h_f^{'}+DISS_f\end{aligned} \tag{6}$$

RELAP5-3D uses the final two continuity equations, Equations 7 and 8, to calculate the phasic velocities in the system. In these equations, C is the coefficient of virtual mass, B_x is the body force in the x coordinate direction, FIG and FIF are the phasic interphase drag coefficients and FWG and FWF and the phasic wall drag coefficients.

$$\begin{aligned}\alpha_g\rho_g A\tfrac{\partial v_g}{\partial t}+\tfrac{1}{2}\alpha_g\rho_g A\tfrac{\partial v_g^2}{\partial x}=-\alpha_g A\tfrac{\partial P}{\partial x}+\alpha_g\rho_g B_x A-\left(\alpha_g\rho_g A\right)FWG\left(v_g\right)\\ +\Gamma_g A\left(v_{gI}-v_g\right)-\left(\alpha_g\rho_g A\right)FIG\left(v_g-v_f\right)\\ -C\alpha_g\alpha_f\rho_m A\left[\tfrac{\partial\left(v_g-v_f\right)}{\partial t}+v_f\tfrac{\partial v_g}{\partial x}-v_g\tfrac{\partial v_f}{\partial x}\right]\end{aligned} \tag{7}$$

$$\begin{aligned}\alpha_f\rho_f A\tfrac{\partial v_f}{\partial t}+\tfrac{1}{2}\alpha_f\rho_f A\tfrac{\partial v_f^2}{\partial x}=-\alpha_f A\tfrac{\partial P}{\partial x}+\alpha_f\rho_f B_x A-\left(\alpha_f\rho_f A\right)FWF\left(v_f\right)\\ +\Gamma_g A\left(v_{fI}-v_f\right)-\left(\alpha_f\rho_f A\right)FIF\left(v_f-v_g\right)\\ -C\alpha_f\alpha_g\rho_m A\left[\tfrac{\partial\left(v_f-v_g\right)}{\partial t}+v_g\tfrac{\partial v_f}{\partial x}-v_f\tfrac{\partial v_g}{\partial x}\right]\end{aligned} \tag{8}$$

For transients in fast systems, the boron concentration and noncondensable quantity is not important to the simulation but is still calculated. Because coolant flow in a nuclear reactor is dominated by large momentum sinks and sources such as pumps or abrupt area changes, RELAP5-3D's solution to the field equations considers momentum conservation effects as secondary to the mass and energy conservation effects [16].

Once the eight primary independent variables are solved for, the remaining important thermodynamic properties such as temperature and density can be expressed as functions of the independent variables. RELAP5-3D's semi-implicit numerical solution scheme uses a system of finite difference equations, which are partially implicit in time, to represent the system of differential equations used to describe the system. A convenient feature of RELAP5-3D's solution scheme is that the field equations for each single volume can be reduced to a single difference equation of vectors and matrices. [16]

It should be noted that when working with liquid metal coolants, RELAP5-3D should only be used for single-phase flow simulations. Limited vapor-phase data is available in RELAP5-3D for liquid metals but this does not limit these investigations as the phenomena that occur after coolant boiling begins is not of interest in this study.

CHAPTER V

S-PRISM CORE PROPERTIES

5.1 S-PRISM Compositions and Assembly Layout

Limited details are available about the true compositions of the driver fuel and blanket assemblies in S-PRISM's Oxide and Metal cores. Based on data from Reference [13], which includes core inventory of Uranium, fissile Plutonium, and Transuranics at Beginning of Cycle (BOC), preliminary estimates were made for the BOC composition of the driver fuel and blanket assemblies of the Oxide and Metal cores. Several assumptions were then made, which, when applied to the preliminary composition estimates, led to initial approximations of the true S-PRISM fuel compositions. The assumptions used in the creation of BOC fuel compositions are:

1. All uranium was natural uranium,
2. the fuel did not contain any fission products,
3. the fuel's density must be less than theoretical density,
4. internal and radial blanket assemblies had the same composition at BOC,
5. minor actinide and non-fissile plutonium masses were equal,
6. the ratio of non-fissile plutonium to fissile plutonium was 0.25,
7. the minor actinide isotopic ratios were set equal to those of another sodium cooled fast reactor design [45], which was based on a fuel type being developed at Argonne National Laboratory.

Because it would not be feasible to generate accurate BOC compositions without accurate Beginning of Life (BOL) compositions or the assembly shuffling and reloading pattern, the fuel at the beginning of each cycle is assumed to be fresh. The initial approximations of the fuel compositions led to power profiles and cycle reactivity losses that were not yet acceptable. These assumptions provided constraints within which the fuel compositions could be modified to achieve feasible results.

After initial estimates for the BOC compositions were found, the compositions were modified by the total fissile plutonium mass as well as by the driver fuel to blanket ratio of plutonium and minor actinide content. BOC fuel compositions were modified until neutron multiplication factors for BOC, MOC and EOC slightly above unity and similar linear power values to the target values given in Reference [13] were obtained. The final Oxide and Metal cores found are described below followed by a description of the redesigned Nitride core.

5.1.1 Oxide Core

S-PRISM's Oxide core has 11 rings of hexagonal driver fuel and blanket assemblies surrounded by 3 rings of shield and reflector assemblies. The layout of these assemblies is shown in Figure 2. The 1.37-m-tall active region of the core is composed of 162 driver fuel assemblies, 73 internal blanket assemblies, and 60 radial blanket assemblies. Oxide driver fuel assemblies have 217 pins in a 9-ring triangular lattice with a fuel radius of 0.353 cm and a pin radius of 0.426 cm. The Oxide driver fuel pin gap is only 0.009 cm, which is about one-fourth the Metal and Nitride pin gap, but this is acceptable because Oxide pins do not experience the same amount of fuel swelling as Metal and Nitride pins. Oxide internal and radial blanket assemblies have 127 pins in a 7 ring triangular lattice, a fuel radius of 0.53795 cm and a pin radius of 0.601 cm. More dimensions for the Oxide pins and assemblies are given in Table 13.

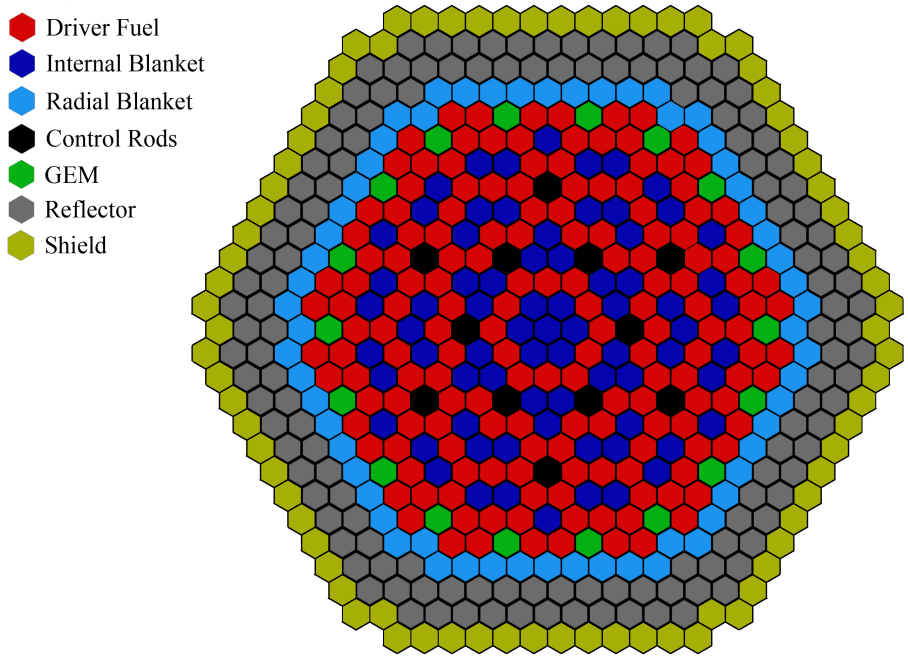

Figure 2: Assembly layout of Oxide S-PRISM core

5.1.1.1 Oxide Fuel Compositions and Power Profiles

Using stoichiometric Oxide fuel, where there are exactly two oxygen atoms per actinide atom, resulted in a density of 11.05 g/cm^3. Stoichiometric fuel was chosen because on average it has a lower thermal conductivity than hypostoichiometric fuel [25], resulting in more conservative transient results. At Beginning of Cycle the Oxide core driver fuel is composed of 65.1% Uranium, 19.2% Plutonium, 3.8% Minor Actinides and 11.8% Oxygen and the blankets are composed of 82.7% Uranium, 4.6% Plutonium, 0.9% Minor Actinides and 11.8% Oxygen. The isotopic composition of the Oxide fuel at all three reference points in the fuel cycle is given in Tables 1 and 2. The decrease in total fuel mass throughout the fuel cycle is a result of ERANOS only tracking 195 fission products, which are the strongest contributors to reactivity and long-term decay heat. Because the blanket assemblies have a much larger fuel radius than the driver fuel assemblies, they require less fissile plutonium to maintain

safe centerline temperatures.

Table 1: Driver fuel composition of S-PRISM Oxide core

	BOC		MOC		EOC	
Nuclide	Mass (kg)	%	Mass (kg)	%	Mass (kg)	%
U^{234}	0.73	0.004	0.95	0.005	1.37	0.007
U^{235}	96.50	0.463	88.36	0.427	80.96	0.393
U^{236}	0.00	0.000	1.84	0.009	3.46	0.017
U^{238}	13,475.52	64.627	13,316.95	64.281	13,155.20	63.877
Pu^{238}	19.11	0.092	46.54	0.225	76.17	0.370
Pu^{239}	2,865.40	13.742	2,769.80	13.370	2,680.50	13.016
Pu^{240}	726.37	3.484	751.09	3.626	772.92	3.753
Pu^{241}	341.36	1.637	305.46	1.474	275.42	1.337
Pu^{242}	56.21	0.270	56.23	0.271	71.03	0.345
Np^{237}	400.97	1.923	375.75	1.814	352.25	1.710
Am^{241}	332.66	1.595	320.89	1.549	308.69	1.499
Am^{243}	68.07	0.326	64.62	0.312	61.58	0.299
O	2,468.18	11.837	2,469.19	11.919	2,469.19	11.989
FPs	0.00	0.000	133.39	0.644	262.49	1.275
Other MA	0.00	0.000	15.69	0.076	23.42	0.114
Total	20,851.08	100.000	20,699.22	100.000	20,567.77	100.000

Oxide pin restructuring, which can occur in only hours after reaching full power, must be considered when analyzing the Oxide core. According to Reference [46], the boundaries of the equiaxed and columnar restructured regions that form during pin irradiation can be approximated as occurring at the radial location of 1,773 K and 2,173 K $-5\cdot(linearpower)$, respectively, in the pins. Steady-state temperatures in the Oxide core, given in Chapter 6, are below both these temperatures and consequently pin restructuring does not occur in the Oxide core. The transients simulated in this study were not of long enough time scales to maintain temperatures above 1,773 K and thus the effects of Oxide pin restructuring were not examined.

The assembly power ratings for the Oxide Core at BOC, MOC and EOC are given in Tables 3 and 4. The shift of power from the driver fuel to blanket assemblies represents the build-up of fissile plutonium from BOC to EOC in the assemblies with more fertile isotopes. Average linear powers are also plotted in Figure 3 to illustrate

Table 2: Blanket composition of S-PRISM Oxide core

	BOC		MOC		EOC	
Nuclide	Mass (kg)	%	Mass (kg)	%	Mass (kg)	%
U^{234}	1.04	0.004	1.08	0.005	1.16	0.005
U^{235}	136.78	0.588	127.17	0.547	118.36	0.510
U^{236}	0.00	0.000	2.18	0.009	4.13	0.018
U^{238}	19,100.05	82.065	18,926.21	81.445	18,749.29	80.826
Pu^{238}	5.08	0.022	11.45	0.049	18.45	0.080
Pu^{239}	761.69	3.273	864.85	3.722	957.84	4.129
Pu^{240}	193.08	0.830	201.03	0.865	210.56	0.908
Pu^{241}	90.74	0.390	82.47	0.355	75.49	0.325
Pu^{242}	14.94	0.064	14.95	0.064	18.31	0.079
Np^{237}	106.59	0.458	101.56	0.437	96.88	0.418
Am^{241}	88.43	0.380	86.56	0.372	84.54	0.364
Am^{243}	18.09	0.078	17.33	0.075	16.66	0.072
O	2,757.79	11.849	2,757.79	11.868	2,757.79	11.888
FPs	0.00	0.000	39.95	0.172	82.36	0.355
Other MA	0.00	0.000	3.58	0.015	5.38	0.023
Total	23,274.33	100.000	23,232.40	100.000	23,187.69	100.000

the shifting of power throughout the fuel cycle towards the center of the core. Because driver fuel and blanket pins have different radii, the same power levels in each pin type will result in different centerline fuel temperatures and thus should be compared only to similar pin types.

Table 3: Oxide driver fuel assembly linear powers

Ring #	# Assemblies	Ave. Linear Power (kW/m)			Power/Assembly (MW)		
		BOC	MOC	EOC	BOC	MOC	EOC
3	12	15.51	15.99	16.45	4.58	4.72	4.85
5	18	18.88	18.84	18.80	5.57	5.56	5.55
6	12	20.67	20.24	19.85	6.10	5.97	5.86
7	30	19.28	18.79	18.35	5.69	5.55	5.41
8	18	18.09	17.44	16.85	5.34	5.15	4.97
9	36	14.69	14.16	13.67	4.34	4.18	4.04
10	36	10.51	10.15	9.82	3.10	3.00	2.90

Table 4: Oxide blanket assembly linear powers

Ring #	# Assemblies	Ave. Linear Power (kW/m)			Power/Assembly (MW)		
		BOC	MOC	EOC	BOC	MOC	EOC
1	1	9.30	10.69	12.12	1.61	1.85	2.09
2	6	10.96	12.38	13.83	1.89	2.14	2.39
4	12	13.32	14.81	16.28	2.30	2.56	2.81
5	6	14.90	16.38	17.78	2.57	2.83	3.07
6	18	15.78	17.28	18.64	2.73	2.98	3.22
8	24	14.17	15.19	16.08	2.45	2.62	2.78
9	6	13.08	13.76	14.34	2.26	2.38	2.48
10	6	5.62	5.76	5.87	0.97	0.99	1.01
11	54	4.87	4.98	5.09	0.84	0.86	0.88

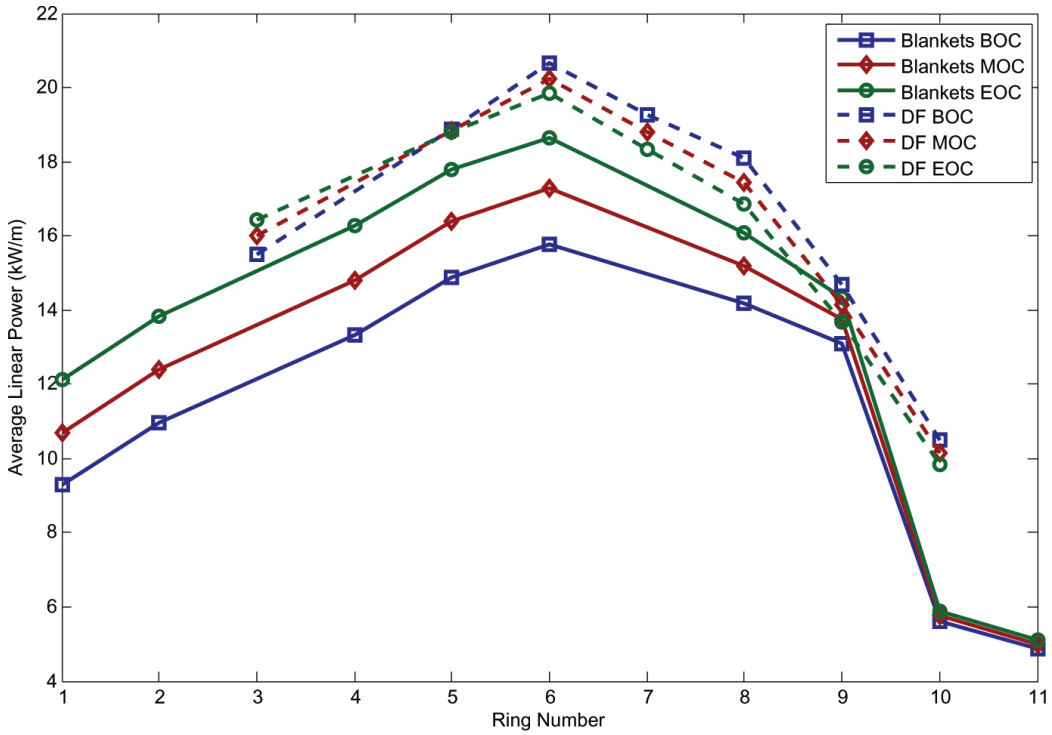

Figure 3: Average linear power of Oxide core assemblies

5.1.2 Metal Core

In the Metal S-PRISM core, there are ten rings of driver fuel and blanket assemblies surrounded by three rings of shield and reflector assemblies. The layout of these assemblies is shown in Figure 4. The 1.02-m-tall active region of the core is composed

of 138 driver fuel assemblies, 49 internal blanket assemblies, and 48 radial blanket assemblies. The Metal core can maintain criticality with fewer assemblies than the Oxide core because the fuel is denser in the Metal core. Metal driver fuel assemblies have 271 pins in a ten ring triangular lattice with a fuel radius of 0.274 cm, a pin radius of 0.372 cm, and a gap width of 0.042 cm. The internal and radial blanket assemblies have 127 pins in a seven ring triangular lattice with a fuel radius of 0.502 cm, a pin radius of 0.601 cm, and a gap width of 0.042 cm. More dimensions for the Metal pins and assemblies are given in Table 13.

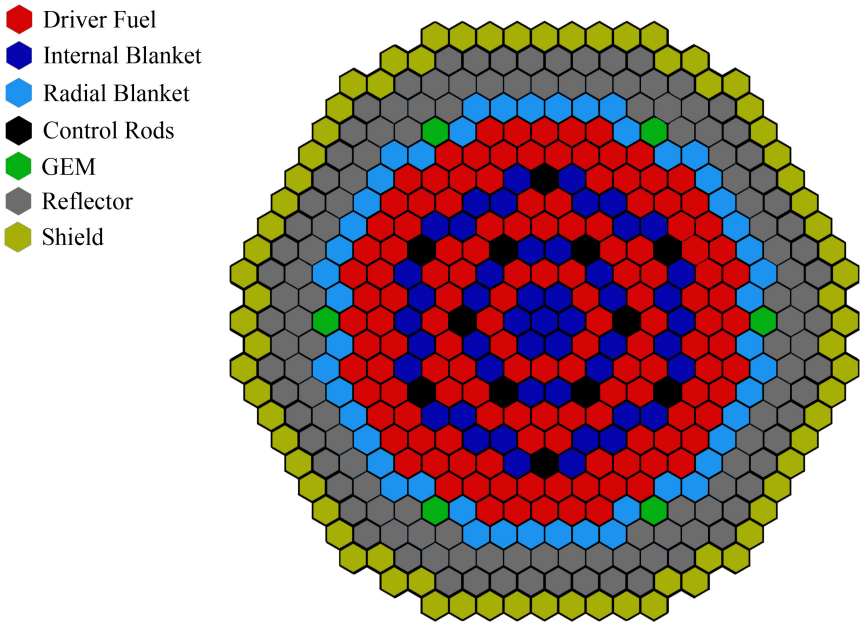

Figure 4: Assembly layout of Metal S-PRISM core

5.1.2.1 Metal Fuel Compositions and Power Profiles

The fresh fuel loaded in the Metal S-PRISM core at BOC has a driver fuel composition of 69.5% Uranium, 17.1% Plutonium, 3.4% Minor Actinides, and 10.0% Zirconium and a blanket composition of 85.1% Uranium, 4.1% Plutonium, 0.8% Minor Actinides, and 10.0% Zirconium, both at a density of 15.05 g/cm^3. The isotopic composition of

the Metal fuel at all three reference points in the fuel cycle is given in Tables 5 and 6. As with the Oxide compositions, the smaller total mass at MOC and EOC is a result of ERANOS only tracking the isotopes with a strong contribution to reactivity and long-term decay heat.

Table 5: Driver fuel composition of S-PRISM Metal core

	BOC		MOC		EOC	
Nuclide	Mass (kg)	%	Mass (kg)	%	Mass (kg)	%
U^{234}	0.51	0.004	0.64	0.005	0.93	0.007
U^{235}	66.57	0.494	58.07	0.435	50.72	0.384
U^{236}	0.00	0.000	1.71	0.013	3.14	0.024
U^{238}	9295.73	68.955	9131.63	68.414	8970.60	67.852
Pu^{238}	11.01	0.082	32.49	0.243	54.35	0.411
Pu^{239}	1650.19	12.241	1568.57	11.752	1496.13	11.316
Pu^{240}	418.28	3.103	431.95	3.236	443.14	3.352
Pu^{241}	196.42	1.457	167.58	1.256	145.04	1.097
Pu^{242}	32.37	0.240	39.13	0.293	44.59	0.337
Np^{237}	230.90	1.713	209.72	1.571	190.72	1.443
Am^{241}	191.56	1.421	176.98	1.326	163.14	1.234
Am^{243}	39.20	0.291	36.26	0.272	33.82	0.256
Zr	1348.08	10.000	1348.08	10.100	1348.08	10.197
FPs	0.00	0.000	131.89	0.988	258.04	1.952
Other MA	0.00	0.000	12.85	0.096	18.44	0.140
Total	13480.81	100.000	13347.55	100.000	13220.90	100.000

The assembly power ratings for the Metal Core at BOC, MOC and EOC are given in Tables 7 and 8. Average linear powers for driver fuel and blanket assemblies are plotted in Figure 5 but, as before, should only be compared to assemblies of similar dimensions. Figure 5 illustrates the shift of power towards the center of the core at MOC and EOC, with a greater power increase in the blanket assemblies due to fissile plutonium build-up.

Table 6: Driver fuel composition of S-PRISM Metal core

	BOC		MOC		EOC	
Nuclide	Mass (kg)	%	Mass (kg)	%	Mass (kg)	%
U^{234}	0.69	0.005	0.70	0.005	0.76	0.005
U^{235}	90.34	0.605	80.52	0.484	71.91	0.484
U^{236}	0.00	0.000	2.03	0.014	3.76	0.025
U^{238}	12615.41	84.462	12439.26	82.605	12265.96	82.605
Pu^{238}	2.93	0.020	8.13	0.092	13.59	0.092
Pu^{239}	438.56	2.936	538.51	4.204	624.32	4.204
Pu^{240}	111.16	0.744	116.87	0.838	124.46	0.838
Pu^{241}	52.20	0.349	45.61	0.272	40.44	0.272
Pu^{242}	8.60	0.058	10.18	0.077	11.50	0.077
Np^{237}	61.36	0.411	57.20	0.360	53.45	0.360
Am^{241}	50.91	0.341	48.02	0.305	45.22	0.305
Am^{243}	10.42	0.070	9.76	0.062	9.21	0.062
Zr	1493.62	10.000	1493.62	10.059	1493.62	10.059
FPs	0.00	0.000	41.32	0.581	86.30	0.581
Other MA	0.00	0.000	3.03	0.020	4.42	0.030
Total	14936.20	100.000	14894.76	100.000	14848.92	100.000

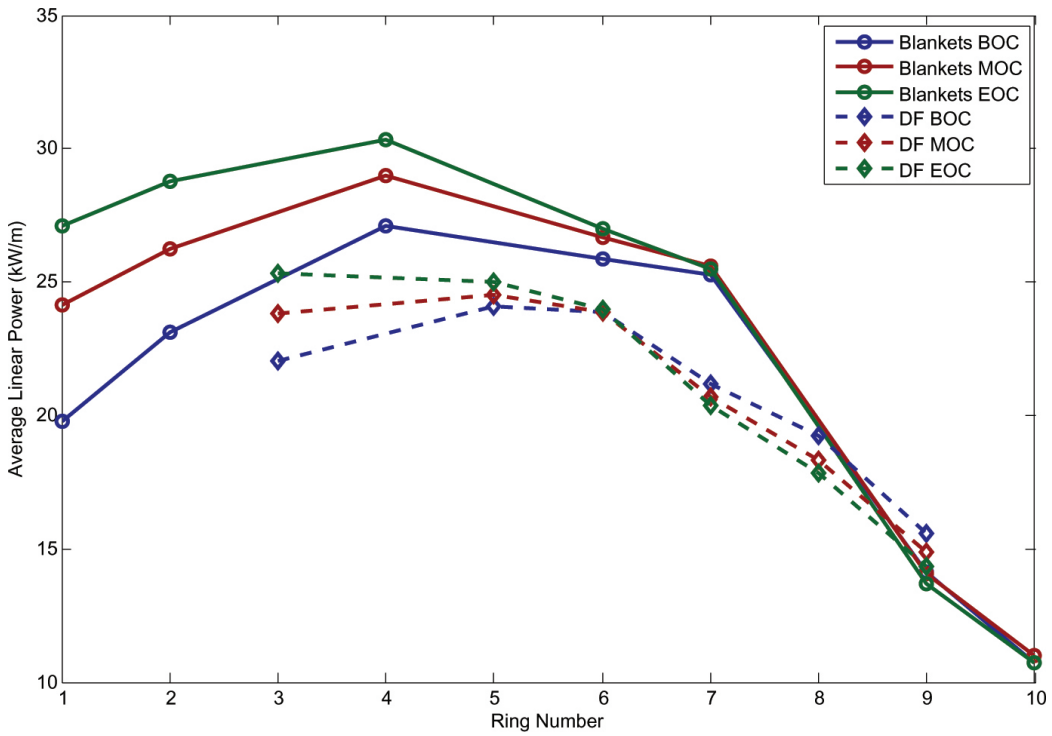

Figure 5: Average linear power of Metal core assemblies

Table 7: Metal driver fuel assembly linear powers

Ring #	# Assemblies	Ave. Linear Power (kW/m)			Power/Assembly (MW)		
		BOC	MOC	EOC	BOC	MOC	EOC
3	12	22.05	23.82	25.34	6.07	6.47	6.88
5	24	24.07	24.54	25.04	6.63	6.66	6.79
6	12	23.88	23.90	24.00	6.58	6.49	6.52
7	18	21.18	20.68	20.36	5.83	5.61	5.53
8	42	19.22	18.35	17.83	5.29	4.98	4.84
9	30	15.57	14.85	14.36	4.29	4.03	3.90

Table 8: Metal blanket assembly linear powers

Ring #	# Assemblies	Ave. Linear Power (kW/m)			Power/Assembly (MW)		
		BOC	MOC	EOC	BOC	MOC	EOC
1	1	19.78	24.17	27.08	2.55	3.08	3.45
2	6	23.11	26.23	28.76	2.98	3.34	3.66
5	12	27.13	28.97	30.36	3.50	3.69	3.86
6	18	25.86	26.70	27.02	3.34	3.40	3.44
7	12	25.28	25.59	25.50	3.26	3.26	3.24
9	12	14.11	14.09	13.70	1.82	1.79	1.74
10	36	10.72	10.98	10.71	1.38	1.40	1.36

5.1.3 Nitride Core

An S-PRISM Nitride core was designed to take advantage of the high melting temperature and thermal conductivity of nitride fuels while maintaining the major characteristics of the Oxide and Metal cores, specifically the thermal power and cycle length. The first step was to identify characteristics of the Oxide and Metal cores that were the same. Preliminary designs of the Nitride core maintained pin and assembly dimensions that were the same in both the Oxide and Metal cores. Assembly dimensions that were fixed in this way include the pitch, duct gap thickness, inner and outer flat-to-flat distance and duct wall thickness. In the blanket assemblies, all three core types had 127 pins in seven rings per assembly, as well as the same pin pitch and clad inner and outer radii. Because Nitride fuels experience similar swelling to Metal fuels due to fission gas build-up, the Nitride blanket pin gap thickness was

set equal to the Metal blanket pin gap thickness of 0.042 cm. The gap thickness and inner clad radius determined that the fuel radius of the blanket pins in the Nitride core was 0.502 cm.

Because of the high melting temperature and thermal conductivity of Nitride fuels, the Nitride driver fuel pins were put into a nine ring arrangement, which allows for thicker fuel pins and better fuel packing. Oxide pins also used a nine ring arrangement so an outer pin radius of 0.426 cm, the same as in Oxide pins, was chosen for Nitride driver fuel pins. Because Nitride fuels are compatible with the sodium coolant, the larger clad thickness for Oxide pins was not necessary. But Oxide pins have a small gap thickness that would not allow for adequate pin swelling during irradiation in Nitride pins. Therefore, the gap and cladding thicknesses used for Metal driver fuel pins were also chosen for Nitride driver fuel pins. The required large gap thickness led to Nitride driver fuel pins having a cross-sectional area of 73.05 cm^2/assembly, smaller than for Oxide pins at 84.93 cm^2/assembly, but larger than for Metal pins at 63.85 cm^2/assembly.

Assuming 95% of theoretical density of Nitride fuel, which is 14.32 g/cm^3 [34], gives a density of 13.60 g/cm^3. An active core height of 119.38 cm, which is the average of the Oxide and Metal core heights, gave a total fuel mass of 33,300 kg. An initial guess of 2,750 kg of fissile plutonium and 4,500 kg of transuranics (TRU) produced reasonable reactivities at BOC, MOC and EOC. Eventually the fissile plutonium content was increased to 3,000 kg before being fixed. The TRU content remained at 4,500 kg. This left 26,950 kg for natural uranium and 1,850 kg for nitrogen.

Future studies on Nitride fuels will need to determine the optimal level of N^{15} enrichment necessary during fuel fabrication. These studies must balance decreased C^{14} production from decreasing N^{14} levels with the considerable expense of the enrichment process. Since the neutron spectrum using N^{15} is harder than for N^{14}, lower N^{15} enrichment levels will provide greater safety characteristics in the reactor. For

this study, an enrichment level of 10% N^{15} by atom percent was chosen to represent a compromise between the economic concerns, radiotoxicity safety concerns and Doppler feedback, with the Doppler feedback being the most important concern for this study. Future work must determine if this enrichment level is satisfactory.

An appropriate Nitride core assembly layout was designed concurrently with the fuel composition to ensure acceptable reactivity and minimize power peaking throughout the cycle. Compared to the driver fuel assemblies in the Metal core, the Nitride fuel had a lower density but a higher volume fraction so the Nitride core was set to ten rings of driver fuel and blanket assemblies, the same as for the Metal core. The Control Rod and Gas Expansion Module (GEM) assemblies in Ring 9 were maintained in the Nitride core. Next, all driver fuel and blanket assembly positions that were the same in both the Oxide and Metal cores were set to the same assembly type in the Nitride core. This included all assemblies in Rings 1, 2, 3, 4, and 6. In the Metal and Oxide cores, Rings 5, 7, 8, and 9 had 6, 12, 24, and 18 assemblies, respectively, which were of a different type. Changes to the Nitride core design were iterated within several key areas until acceptable core reactivity levels and power profiles at all stages of the fuel cycle were found. These areas were the classification of the 60 assemblies in Rings 5, 7, 8 and 9 as driver fuel or blanket, the non-Uranium content in the blanket and driver fuel assemblies, and also the assumptions listed at the beginning of this chapter. The final assembly layout of the Nitride core is shown in Figure 6.

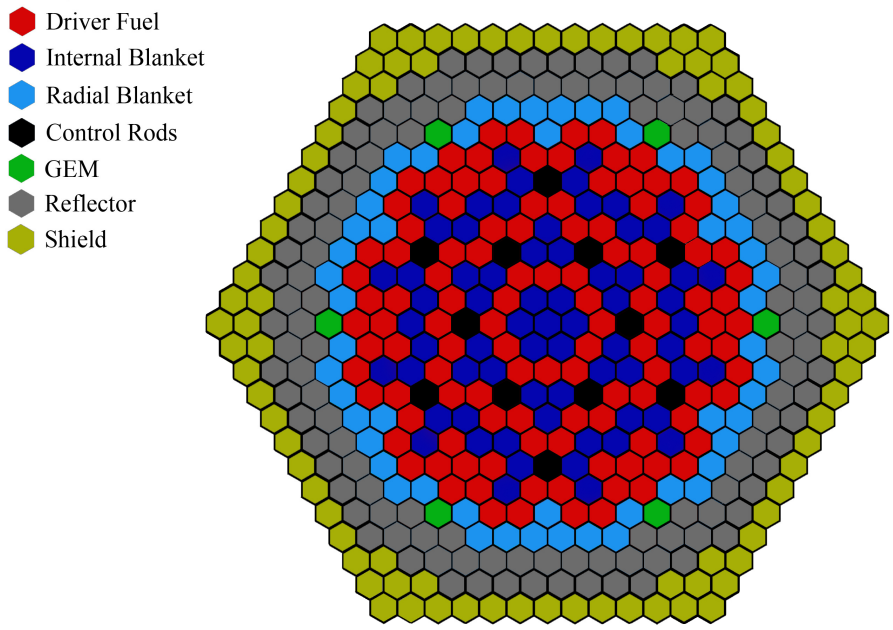

Figure 6: Assembly layout of Nitride S-PRISM core

5.1.3.1 Nitride Fuel Compositions and Power Profiles

Fresh fuel at BOC in the Nitride S-PRISM core has a driver fuel composition of 68.1% Uranium, 21.9% Plutonium, 4.4% Minor Actinides, and 5.6% Nitrogen. Blanket assemblies are composed of 89.6% Uranium, 4.0% Plutonium, 0.8% Minor Actinides, and 5.6% Nitrogen. The isotopic composition of the Nitride blanket and driver fuel assemblies at BOC, MOC and EOC are given in Tables 9 and 10. As with the Oxide and Metal compositions, ERANOS only tracks isotopes with a strong contribution to reactivity and long-term decay heat so the total mass at MOC and EOC is slightly lower than at BOC.

Power per assembly for each assembly type at BOC, MOC and EOC is given in Tables 11 and 12 below. Figure 7 illustrates the changing power profile for driver fuel and blanket assemblies from BOC to EOC.

Table 9: Driver fuel composition of S-PRISM Nitride core

	BOC		MOC		EOC	
Nuclide	Mass (kg)	%	Mass (kg)	%	Mass (kg)	%
U^{234}	0.50	0.004	0.66	0.005	1.00	0.008
U^{235}	65.46	0.484	58.69	0.439	52.68	0.397
U^{236}	0.00	0.000	1.44	0.011	2.69	0.020
U^{238}	9141.42	67.647	9006.19	67.291	8873.14	66.912
Pu^{238}	14.11	0.104	37.44	0.280	61.91	0.467
Pu^{239}	2115.66	15.656	2007.18	14.997	1909.51	14.400
Pu^{240}	536.32	3.969	554.01	4.139	568.74	4.289
Pu^{241}	252.05	1.865	221.00	1.651	195.81	1.477
Pu^{242}	41.51	0.307	48.50	0.362	54.35	0.410
Np^{237}	296.07	2.191	273.23	2.042	252.40	1.903
Am^{241}	245.62	1.818	232.40	1.736	219.41	1.655
Am^{243}	50.26	0.372	47.13	0.352	44.46	0.335
N^{14}	674.18	4.989	674.18	5.037	674.18	5.084
N^{15}	80.26	0.594	80.26	0.600	80.26	0.605
FPs	0.00	0.000	128.04	0.957	250.42	1.890
Other MA	0.00	0.000	13.60	0.102	19.94	0.150
Total	13513.42	100.000	13383.97	100.000	13260.93	100.000

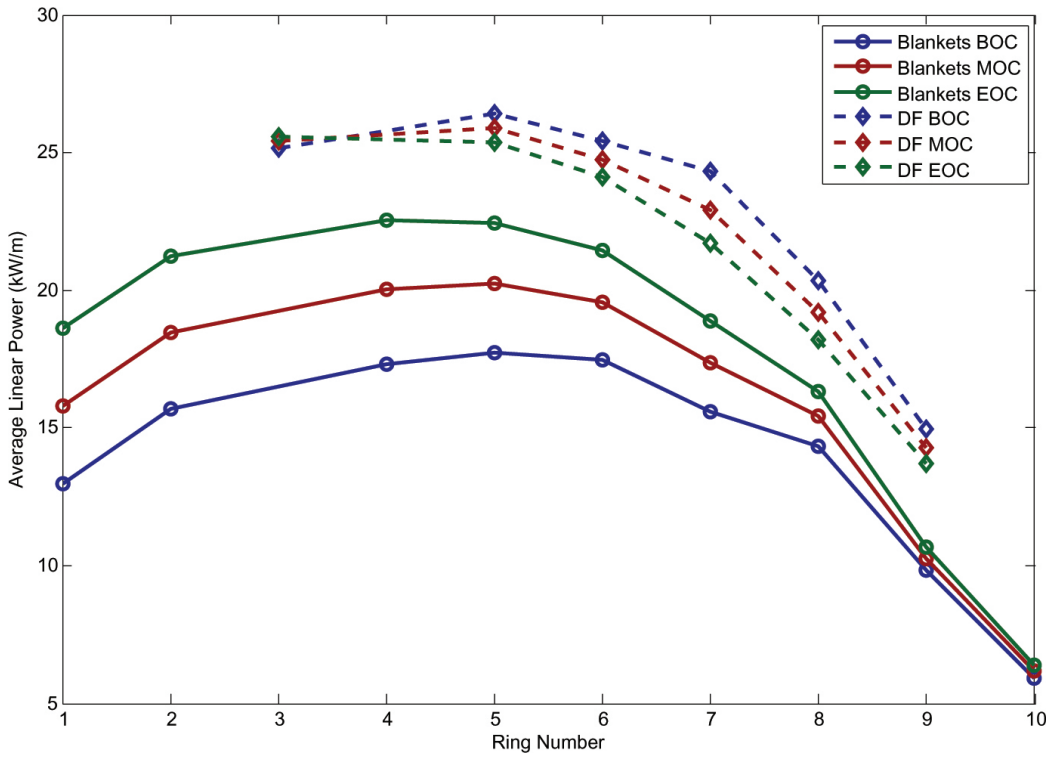

Figure 7: Average linear power of Nitride core assemblies

Table 10: Blanket composition of S-PRISM Nitride core

	BOC		MOC		EOC	
Nuclide	Mass (kg)	%	Mass (kg)	%	Mass (kg)	%
U^{234}	0.96	0.005	0.98	0.005	1.04	0.005
U^{235}	126.08	0.637	114.40	0.580	103.99	0.528
U^{236}	0.00	0.000	2.55	0.013	4.75	0.024
U^{238}	17604.98	88.990	17392.61	88.118	17183.29	87.278
Pu^{238}	3.75	0.019	9.73	0.049	16.12	0.082
Pu^{239}	562.81	2.845	690.45	3.498	802.63	4.077
Pu^{240}	142.67	0.721	150.41	0.762	160.62	0.816
Pu^{241}	67.05	0.339	59.81	0.303	54.01	0.274
Pu^{242}	11.04	0.056	12.76	0.065	14.23	0.072
Np^{237}	78.76	0.398	74.15	0.376	69.96	0.355
Am^{241}	65.34	0.330	62.59	0.317	59.87	0.304
Am^{243}	13.37	0.068	12.63	0.064	12.01	0.061
N^{14}	988.58	4.997	988.58	5.009	988.58	5.021
N^{15}	117.69	0.595	117.69	0.596	117.69	0.598
FPs	0.00	0.000	45.16	0.229	94.28	0.479
Other MA	0.00	0.000	3.38	0.017	5.00	0.025
Total	19783.07	100.000	19737.89	100.000	19688.07	100.000

5.1.4 Assembly and Pin Geometric Summary

Table 13 below includes all major dimensions of the pin and assemblies in the Metal, Oxide, and Nitride S-PRISM cores.

Radial power peaking values for blanket and driver fuel assemblies in the three cores are given below in Table 14. With the exception of the Oxide driver fuel assemblies, which remain nearly constant, the radial power peaking values change as expected, increasing throughout the cycle as more fissile isotopes are bred in the center of the core.

5.2 Material Thermal Property Data

Thermal hydraulics simulations in RELAP5-3D require thermal property data for all solid compositions modeled in the system. The two necessary pieces of data are thermal conductivity, in $W/m \cdot K$, and volumetric heat capacity, which is the product of density and specific heat capacity and has units of J/m^3-K. Thermal conductivities

Table 11: Nitride driver fuel assembly linear powers

Ring #	# Assemblies	Ave. Linear Power (kW/m)			Power/Assembly (MW)		
		BOC	MOC	EOC	BOC	MOC	EOC
3	12	25.18	25.42	25.59	7.79	7.49	7.54
5	18	26.42	25.89	25.37	7.49	7.63	7.48
6	12	25.40	24.73	24.09	7.17	7.29	7.10
7	18	24.31	22.91	21.69	6.00	6.75	6.39
8	30	20.37	19.20	18.18	4.41	5.66	5.36
9	24	14.97	14.29	13.69	7.79	4.21	4.04

Table 12: Nitride blanket assembly linear powers

Ring #	# Assemblies	Ave. Linear Power (kW/m)			Power/Assembly (MW)		
		BOC	MOC	EOC	BOC	MOC	EOC
1	1	12.97	15.80	18.65	2.24	2.73	3.22
2	6	15.67	18.48	21.23	2.70	3.19	3.66
4	12	17.31	20.03	22.54	2.99	3.46	3.89
6	6	17.76	20.23	22.46	3.06	3.49	3.88
7	18	17.45	19.58	21.43	3.01	3.38	3.70
9	12	15.61	17.35	18.86	2.69	2.99	3.25
10	12	14.33	15.42	16.34	2.47	2.66	2.82

and volumetric heat capacities can be input as either constant or temperature dependent properties. RELAP5-3D interpolates between temperature dependent data, which are input as individual values for as many or as few temperatures as the user wishes. Thermal property data for the available coolants are included within RELAP5-3D and do not need to be input by the user.

Because of uncertainties in the thermal property data, driver fuel and blanket assemblies had the same thermal conductivity and heat capacity values during the RELAP5-3D transient simulations. Data for some fuel compositions such as Uranium Oxide are more widely known but for others the data may not be known or in some cases is not available outside of certain national laboratories. Correlations taking stoichiometry or plutonium and minor actinide content into account are often not available either. More accurate transient simulations can be performed when material

Table 13: Assembly and pin geometry

	Oxide	Metal	Nitride
Driver Fuel Assemblies			
Pin Count	217	271	217
Number of Pin Rings Per Assembly	9	10	9
Assembly Pitch (cm)	16.142	16.142	16.142
Duct Gap (cm)	0.432	0.432	0.432
Assembly Flat-to-Flat (cm)	15.71	15.71	15.71
Duct Wall Thickness (cm)	0.394	0.394	0.394
Assembly Inner Flat-to-Flat (cm)	14.922	14.922	14.922
Pin Pitch (cm)	1.01356	0.90687	1.01356
Fuel Radius (cm)	0.35295	0.27385	0.32735
Gap Thickness (cm)	0.00905	0.04225	0.04225
Clad Thickness (cm)	0.0635	0.0559	0.0559
Clad Inner Radius (cm)	0.362	0.3161	0.3696
Clad Outer Radius (cm)	0.4255	0.372	0.4255
Coolant Thickness Per Pin (cm)	0.16256	0.16287	0.16256
Blanket Assemblies			
Pin Count	127	127	127
Number of Pin Rings Per Assembly	7	7	7
Assembly Pitch (cm)	16.142	16.142	16.142
Duct Gap (cm)	0.432	0.432	0.432
Assembly Flat-to-Flat (cm)	15.71	15.71	15.71
Duct Wall Thickness (cm)	0.394	0.394	0.394
Assembly Inner Flat-to-Flat (cm)	14.922	14.922	14.922
Pin Pitch (cm)	1.32542	1.32542	1.32542
Fuel Radius (cm)	0.53795	0.5023	0.5023
Gap Thickness (cm)	0.00665	0.0423	0.0423
Clad Thickness (cm)	0.0559	0.0559	0.0559
Clad Inner Radius (cm)	0.5446	0.5446	0.5446
Clad Outer Radius (cm)	0.6005	0.6005	0.6005
Coolant Thickness Per Pin (cm)	0.12442	0.12442	0.12442

Table 14: Radial power peaking during fuel cycle

	Driver Fuel Assemblies			Blanket Assemblies		
	Oxide	Metal	Nitride	Oxide	Metal	Nitride
BOC	1.19	1.30	1.21	1.46	1.59	1.45
MOC	1.23	1.30	1.23	1.49	1.61	1.49
EOC	1.28	1.30	1.26	1.54	1.64	1.53

property data that takes into account the effects of specific isotopic composition, stoichiometry, radiation damage, burn-up, fuel fabrication techniques and impurity content becomes available.

5.2.1 Oxide Fuel

Thermal property data for Oxide fuels is available due to extensive experience with Oxide fuels in thermal reactors. The thermal conductivity of oxide fuels tends to be U-shaped with a minimum in the vicinity of 1,500 °C [25]. Data is very well known at low temperatures and most Oxide correlations match up very well at temperatures below 1,500 °C. At temperatures near the melting point, however, data becomes very sparse and correlations tend to predict different values. Washington's Correlation from Reference [25] was used for the thermal conductivity of the MOX fuel. For stoichiometric UO_2, where the ratio of Oxygen to Uranium is exactly 2, the thermal conductivity is predicted by Equation 9 and is valid between 773 and 3073 K.

$$k(W/m \cdot K) = (0.035 + 2.25 \cdot 10^{-4} \cdot T)^{-1} + 83.0 \cdot 10^{-12} \cdot T^3 \tag{9}$$

To account for Plutonium content between 12 and 30% in the Oxide fuel, Washington recommends that over the entire range of the correlation, the thermal conductivity should be assumed to be 5% lower than for pure stoichiometric UO_2. For Plutonium contents less than 12%, the reduction should be proportionally less. With 11.5% Plutonium in the MOX fuel, this results in a decrease in the thermal conductivity by 4.2%. Equation 10 was used to calculate the thermal conductivity of the Oxide fuel

as a function of temperature. Equation 10 was extrapolated on in the RELAP5-3D models to cover the small fraction of fuel that falls below the 773 K lower limit.

$$k(W/m \cdot K) = 0.958 \left[(0.035 + 2.25 \cdot 10^{-4} \cdot T)^{-1} + 83.0 \cdot 10^{-12} \cdot T^3 \right] \quad (10)$$

The heat capacity of Oxide fuel can be approximated by the Leibowitz correlation [39], which is valid in the temperature range between 298 and 3023 K.

$$c_p(J/kg \cdot K) = 194.189 + 26.277 \cdot 10^{-2} \cdot T - 18.135 \cdot 10^{-5} \cdot T^2 + 4.737 \cdot 10^{-8} \cdot T^3 \quad (11)$$

Equation 11 shows good agreement with the correlation in Reference [17], although that correlation is for UO_2, not Mixed Oxide. The UO_2 correlation is only valid up to 2,670 K, which is where it and the Leibowitz correlation begin to deviate significantly. With a density of 11.05 g/cm^3, the volumetric heat capacity of the Oxide fuel is given by:

$$C_p(J/m^3 \cdot K) = 2.146 \cdot 10^6 + 2.903 \cdot 10^3 \cdot T - 2.003 \cdot T^2 + 5.234 \cdot 10^{-2} \cdot T^3 \quad (12)$$

Oxide fuel melting temperatures have been suggested as high as 3,120 K [17] for UO_2 and as low as 3,023 K [39] for MOX fuel. For the transient simulations, the more conservative value of 3,023 K was used as the melting temperature for S-PRISM's MOX fuel.

5.2.2 Metal Fuel

Metal fuels have not been used as much as Oxide fuels and thus have less available thermal property data. There has been a considerable amount of research performed on 10% Zirconium Mixed-Metal Fuel but most of that information is unavailable to

the public in its entirely. Argonne National Laboratory has been at the center of much of this work. Requests for portions of this data were granted in the form of point-wise temperature dependent thermal conductivity and heat capacity data (M. A. Smith, personal communication, January 6, 2010). There is a transition in the thermal conductivity data at 1,000 K that is due to the crystalline phase transformations occurring in the fuel. Thermal conductivity and heat capacity data are given in Tables 15 and 16. The melting temperature of this composition of Metal fuel is 1,350 K.

Table 15: Thermal conductivity of Metal fuel

Temperature (K)	Thermal Conductivity (W/m · K)
298	8.1
500	9.6
800	11.6
868	15.8
1,000	25.4
1,200	28.0

Table 16: Heat capacity of Metal fuel

Temperature (K)	Heat Capacity (J/kg · K)	Volumentric Heat Capacity ($J/m^3 \cdot K$)
298	122.1	1.838E6
500	145.8	2.194E6
800	181.6	2.733E6
868	190.5	2.867E6
1,000	155.6	2.342E6
1,200	178.9	2.672E6

5.2.3 Nitride Fuel

Reactor experience with Nitride fuels is even more limited than with Metal fuels. With only a handful of Nitride fueled reactors completing the design stage, thermal property data is not available for different compositions. Predictions suggest that the thermal conductivity for Mixed Nitride is slightly lower than for Uranium Nitride.

Reference [50] includes plots of the thermal conductivity for 20% Plutonium Mixed Nitride fuel. Best estimates for a curve fit for Sample #1, which was sintered to 95% of theoretical density, produced Equation 13:

$$k(W/m \cdot K) = 7.1728 \cdot ln\,[T(K)] - 33.813 \tag{13}$$

This correlation resulted in a lower thermal conductivity than the Uranium Nitride correlation in Reference [36], which was to be expected. Even though the Nitride Core has a smaller Plutonium content than the correlation for 20% Pu Mixed Nitride fuel, the thermal conductivity correlation in Equation 13 was used as a conservative estimate.

As with Mixed Nitride thermal conductivity, heat capacity data is also not readily available. Reference [22] includes a plot of the heat capacity of 20% Pu Mixed Nitride fuel found with Molecular Dynamics calculations. A best guess curve fit to the data resulted in Equation 14 for the Nitride fuel's heat capacity and Equation 15 for the Nitride fuel's volumetric heat capacity:

$$c_p(J/K \cdot mol) = 13.013 \cdot ln\,[T(K)] - 35.384 \tag{14}$$

With a density of 13.61 g/cm^3, the Nitride fuel's volumetric heat capacity is given by:

$$C_p(J/m^3 \cdot K) = 1.771 \cdot 10^6 \cdot ln\,[T(K)] - 4.816 \cdot 10^6 \tag{15}$$

The melting temperature of the Nitride fuel is 3,035 K [34].

5.2.4 Cladding

Because data on HT9 and HT9(m), the structural and cladding materials used in S-PRISM, is closely protected, thermal property data is not readily available. Oxide Dispersion Strengthened (ODS) steels have shown similar properties to the low-swelling ferritic-martensitic HT9 and have available thermal property data. The transient results will not be very sensitive to the choice of cladding so an ODS steel, MA956, with available thermal property data was chosen for the transient calculations. Comparison with the limited HT9 data suggests that MA956 has a similar melting temperature and thermal conductivity.

The thermal conductivity and specific heat of MA956 is given in Table 17. The volumetric heat capacity uses MA956's density of 7.25 g/cm^3. The melting temperature of MA956 is 1,753 K

Table 17: Thermal property data for MA956

Temp (K)	Thermal Conductivity (W/m · K)	Specific Heat (J/kg · K)	Volumetric Heat Capacity (J/m^3· K)
293	10.9	469	3.400E6
373	12.2	491	3.560E6
473	13.9	519	3.763E6
573	15.4	547	3.966E6
673	16.9	575	4.169E6
773	18.4	602	4.365E6
873	19.8	630	4.568E6
973	21.2	658	4.771E6
1073	22.6	686	4.974E6
1173	24.1	714	5.177E6
1273	25.5	741	5.372E6
1373	27.0	769	5.575E6

Figures 8 and 9 illustrate the thermal conductivities and volumetric heat capacities for all three fuel types and the cladding material. The low thermal conductivity of the Oxide fuel and melting temperature of the Metal fuel were expected to be obstacles to transient performance during the RELAP5-3D simulations. The Nitride fuel's higher

thermal conductivity and melting temperature were expected to provide significant advantages during transient simulations.

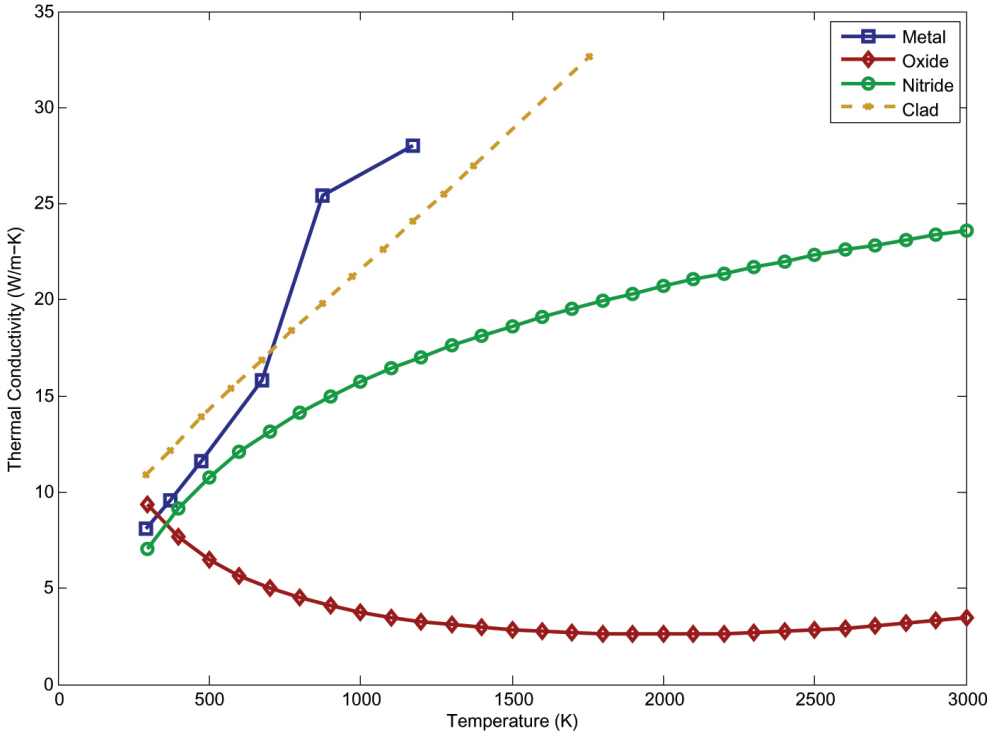

Figure 8: Thermal conductivities of Oxide, Metal and Nitride fuel and cladding

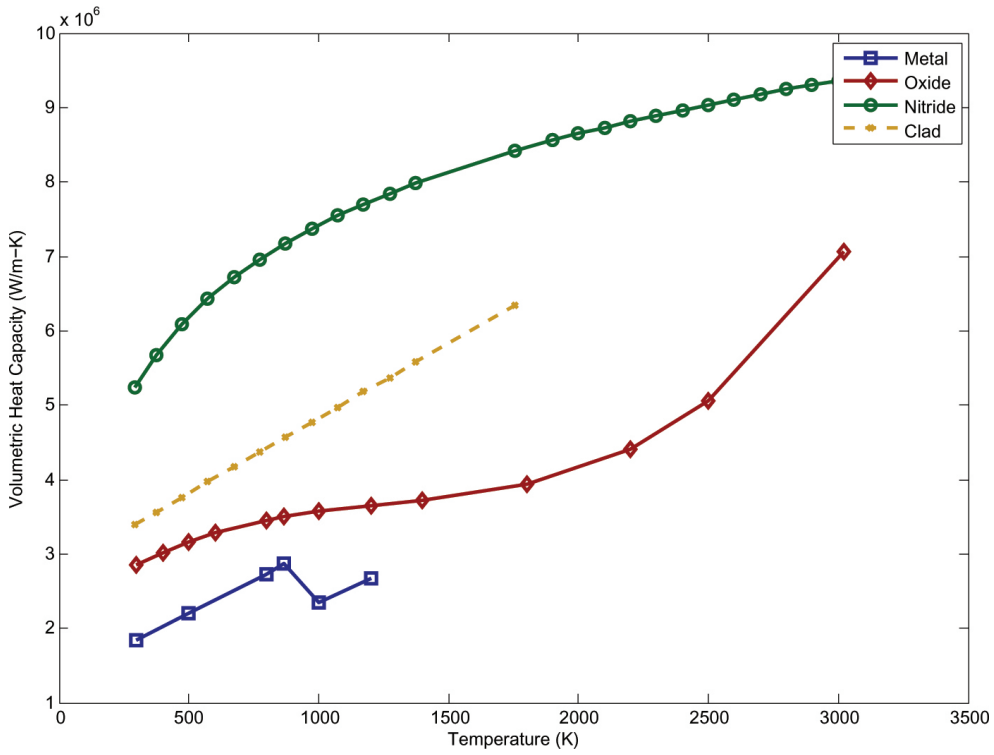

Figure 9: Volumetric heat capacities of Oxide, Metal and Nitride fuel and cladding

5.3 Reactivity Feedbacks

Prompt reactivity feedbacks are the primary counter to sudden changes in the three S-PRISM cores. The reactivity feedbacks that were expected to have the greatest effect on the fission power level are Doppler of the fuel and coolant, axial and radial expansion of the core and coolant thermal expansion. The two Doppler effects provide negative reactivity feedbacks due to large amounts of U^{238} in the system. Axial and radial expansion of the core due to increased core temperatures leads to greater neutron leakage. Thermal expansion of the coolant leads to several competing reactivity effects: spectrum hardening, increased neutron leakage, lower parasitic absorption by the coolant and changes in the energy self-shielding in the flux. The first two effects are the primary components of coolant thermal expansion and are generally of opposing sign. In S-PRISM, the positive reactivity effect of spectrum hardening dominated the other coolant thermal expansion effects.

Feedback coefficients related to the fuel are a function of the fuel temperature while feedbacks related to the coolant are a function of either coolant temperature or density. RELAP5-3D requires the coolant feedbacks to be input as a function of coolant density. However, because the change in sodium density as a function of change in temperature is nearly linear at constant pressure, the coolant feedbacks are listed below as a function of coolant temperature so as to easily illustrate the isothermal reactivity coefficient, the feedback found when temperatures are changing at the same rate throughout the core. The isothermal reactivity coefficient is generally important at very low powers where temperatures throughout the core are increasing at similar rates. Each of the feedbacks is listed in units of pcm/K, where the change in temperature refers to either the fuel or coolant temperature.

Feedbacks are entered in RELAP5-3D as pairs of reactivities and temperatures or densities. The user specifies the fuel temperature or coolant density of one or more components and a weighting factor associated with each component to determine a characteristic value. RELAP5-3D interpolates the characteristic temperature or density within the feedback tables to determine the reactivity insertion due to feedbacks.

5.3.1 Fuel Doppler

The Doppler reactivity feedback of the fuel is dominated by the broadened resonance absorption cross-section in U^{238}. The softer spectra in the Oxide and Nitride cores, due to the presence of oxygen or nitrogen atoms not present in the Metal core, leads to more neutrons reaching resonance energies where the Doppler broadened absorption resonances in U^{238} provide a greater negative feedback. The Oxide and Nitride cores also have larger densities of U^{238} compared with the Metal core. The Metal core's harder spectrum leads to fewer neutrons reaching those important resonant energies and combined with its smaller quantity of U^{238}, the Metal core has the weakest

Doppler feedback coefficient. Doppler coefficients were determined with ERANOS by finding the change in reactivity associated with each core at a series of fuel temperatures. The results are given in Table 18.

Table 18: Fuel Doppler reactivity feedback coefficients (pcm/K)

	BOC	MOC	EOC
Metal	-0.3401	-0.3438	-0.3467
Oxide	-0.5581	-0.5635	-0.5686
Nitride	-0.5532	-0.5650	-0.5727

5.3.2 Axial Expansion of the Core

Increasing fuel temperatures will initiate an expansion of the fuel, which results in an increase of the height of the core active region, leading to increased radial neutron leakage and a negative reactivity feedback. Whereas in the radial core expansion feedback the expansion is determined by the thermal expansion coefficients of the structural components, axial core expansion is determined by the thermal expansion coefficients of the fuel. The Metal fuel has the largest coefficient of thermal expansion and thus experiences a stronger feedback from axial expansion than the other two cores [34], which compensates for the Metal core's lower Doppler feedback.

Table 19: Fuel thermal expansion coefficients (1/K)

Metal	Oxide	Nitride
17E-6	12E-6	10E-6

Axial expansion calculations were performed in ERANOS by increasing the height of the pins while keeping mass constant and comparing the resulting change in reactivity with the corresponding change in temperature that would produce that axial expansion. As expected, the Metal core experienced the largest axial expansion feedback and the Nitride core, with the smallest expansion coefficient, experienced the smallest feedback of the three fuel types. The results are given in Table 20.

Table 20: Axial thermal expansion reactivity feedback coefficients (pcm/K)

	BOC	MOC	EOC
Metal	-0.4655	-0.5818	-0.4386
Oxide	-0.2875	-0.3662	-0.3520
Nitride	-0.2452	-0.2969	-0.2690

5.3.3 Radial Expansion of the Core

Radial expansion of the core leads to a negative reactivity insertion from two primary components: increased axial neutron leakage and increased coolant volume fraction. Even though expanded structural components will occupy an increased volume in the core, the radial expansion of the assembly support structure will result in an even larger increase in the cross-sectional area of the core, increasing the coolant flow area. Increased coolant volume will lead to more neutron parasitic absorption as well as stronger neutron moderation and a softer spectrum, all providing a negative feedback effect.

Because detailed diagrams or descriptions of the structure restraining the fuel assemblies are not available, it is assumed that there is a structural grid at the top of the active fuel region that will push the fuel assemblies radially outward during periods of increased temperatures. This structure will expand as coolant outlet temperatures increase. The lower grid plate will not expand immediately during a transient because there is a large delay before the now hotter outlet coolant travels through the primary loop and returns to the inlet of the core. Only expansion at the outlet of the core will be considered but a delayed negative reactivity feedback due to radial expansion at the inlet should be noted.

Core models in ERANOS were generated in hexagonal 3-D geometry as vertical assemblies with a hexagonal cross-section. With the coolant inlet temperature remaining constant during the beginning of transients, the outlet of the core will experience more radial expansion than the rest of the core. Because the core geometry

could not be generated to reflect the increasing radial expansion along the height of the core, these calculations simulated uniform radial expansion, which produces a reactivity feedback approximately twice what the core would actually experience.

As with other HT9 and HT9(m) material data, a thermal expansion coefficient for the S-PRISM structural material was not available so data for MA956 was again used. The thermal expansion coefficient of MA956 as a function of temperature is given in Table 21 [2]. Table 22 lists the radial thermal expansion feedback coefficients for all three cores.

Table 21: Thermal expansion data for MA956

Temperature (K)	Expansion Coefficient (10^{-6} K)
773	12.7
873	13.0
973	13.4
1073	13.9
1173	14.4

Table 22: Radial thermal expansion reactivity feedback coefficients (pcm/K)

	BOC	MOC	EOC
Metal	-0.1950	-0.1978	-0.1978
Oxide	-0.1515	-0.1490	-0.1472
Nitride	-0.1493	-0.1497	-0.1482

5.3.4 Coolant Doppler and Coolant Thermal Expansion

Because both of these feedbacks have strong effects on the neutron spectrum, the coolant Doppler and coolant thermal expansion reactivity feedbacks were calculated simultaneously in ERANOS to fully capture the secondary neutron spectrum effects that would be otherwise lost. These feedbacks were also calculated individually to get an approximate value of the individual effect of each feedback. All three cores had a very strong positive feedback individually from coolant thermal expansion with the Metal core having a larger feedback effect than the Oxide and Nitride cores.

As illustrated in Figures 3, 5 and 7, the Metal core's power profile peaks closest to the center of the core in Assembly Ring 4. The Nitride and especially the Oxide cores peak power occurs radially further outward, which contributes to the increased leakage term in the coolant thermal expansion feedback. The more negative leakage term in the Oxide and Nitride cores counteracts the positive spectral hardening term and consequently the total coolant feedback effect is more positive in the Metal core than in the Oxide and Nitride cores.

These effects were calculated in ERANOS by simultaneously changing the coolant density and temperature to determine the resulting change in reactivity. The reactivity feedback coefficients for these combined feedback effects are given in Table 23.

Table 23: Coolant Doppler and thermal expansion reactivity feedback coefficients (pcm/K)

	BOC	MOC	EOC
Metal	0.7577	0.8007	0.8366
Oxide	0.5572	0.5878	0.6160
Nitride	0.4985	0.5350	0.5614

5.3.5 Reactivity Feedbacks Summary

Table 24 lists the feedback coefficients for all three cores as well as the isothermal reactivity feedback coefficients. While the isothermal feedback coefficient was not used in the full-power transient simulations, it is a good indicator of each core's transient performance. In all cores the isothermal feedback coefficient was negative and each fuel type experienced its most negative isothermal reactivity coefficient during MOC operation. The isothermal feedback coefficient was most negative in the Oxide and Nitride cores, due to a weaker coolant thermal expansion feedback. In most cases the fuel will have a larger temperature change than the coolant so the feedback coefficient of the fuel will have more weight during transients.

The reactivity feedback associated with fuel bowing was not addressed for these S-PRISM calculations. Depending on the structural constraints imposed on the fuel pins, it is possible that thermally expanding pins can be constrained in such a way as to induce an outwardly bowed shape, resulting in a negative reactivity insertion. The magnitude of this effect can be changed depending on the constraints imposed on the fuel pins. In a reactor where the fuel assemblies are restrained only at the bottom of the core, the fuel will bow outward at the top of the reactor in a 'flowering' fashion producing a negative reactivity feedback similar to the radial expansion feedback. It is also possible to restrain the assembly ducts in such a way that the fuel assemblies bow inward at increased temperatures producing a positive reactivity feedback.

In EBR-II, different axial contact locations for the assembly ducts as well as the looseness or tightness at these contact locations determined the sign of the reactivity feedback[26]. For smaller fast reactors such as EBR-II, fuel bowing is a dominant reactivity feedback effect. However, as fast reactors increase in size, the relative impact of bowed fuel decreases[24]. The increased axial leakage induced from radial expansion of the core must still be considered but for fast reactors with a similar or larger thermal power to S-PRISM, the feedback effect from fuel bowing is rarely considered. In a report on the knowledge gained from the Integral Fast Reactor (IFR) and Advanced Liquid Metal Reactor programs, it was assumed that the fuel does not bow during safety analyses of Sodium Cooled Fast Reactors[43, 12]. Given that the exact design of the restraints imposed on the S-PRISM fuel assemblies at various axial locations in the reactor was unavailable, there is significant uncertainty in the proper calculation method for fuel bowing, and the effect is assumed to be small for larger fast reactors, the reactivity feedback due to fuel bowing was not included for the transient simulations.

Table 24: Reactivity feedback coefficient summary (pcm/K)

	Fuel Doppler	Axial Expansion	Coolant Doppler and Thermal Expansion	Radial Expansion	Isothermal Coefficient
BOC					
Metal	-0.3401	-0.4655	0.7577	-0.1950	-0.2429
Oxide	-0.5581	-0.2875	0.5572	-0.1515	-0.4399
Nitride	-0.5532	-0.2452	0.4985	-0.1493	-0.4492
MOC					
Metal	-0.3438	-0.5818	0.8007	-0.1978	-0.3227
Oxide	-0.5635	-0.3662	0.5878	-0.1490	-0.4909
Nitride	-0.5650	-0.2969	0.5350	-0.1497	-0.4766
EOC					
Metal	-0.3467	-0.4386	0.8366	-0.1978	-0.1465
Oxide	-0.5686	-0.3520	0.6160	-0.1472	-0.4518
Nitride	-0.5727	-0.2690	0.5614	-0.1482	-0.4285

5.4 Delayed Neutron Parameters

The delayed neutron parameters for each S-PRISM core were found using ERANOS's Sn transport module, BISTRO [5]. BISTRO uses perturbation theory to calculate the delayed neutron parameters in six groups, the effective delayed neutron fraction, and mean neutron lifetime over the entire core. These values are given in Tables 25, 26 and 27 where β_i is the delayed neutron fraction of the i^{th} group, λ_i is the delayed neutron half-life of the i^{th} group and Λ is the mean neutron lifetime in the reactor.

5.5 Decay Heat

The 1994 ANS Standard for Decay Heat Power was used to calculate the decay heat power of the S-PRISM cores [1]. This standard, which includes decay data for U^{235}, U^{238}, Pu^{239}, and Pu^{241}, is included within RELAP5-3D. While this standard was generated for thermal spectra, there is not a decay heat standard available for fast systems at this time and the effect of the neutron energy spectrum on short term decay heat generation is assumed to be small. ANS decay heat standards assume that the fuel has been burned for an infinite amount of time allowing for all fission products to reach their equilibrium state. While the fuel cycle calculations did not burn the fuel

Table 25: Delayed neutron parameters for the Metal S-PRISM core

	Metal		
	BOC	MOC	EOC
β_1	8.238E+00	8.335E+00	8.331E+00
β_2	6.999E+01	7.083E+01	7.079E+01
β_3	6.088E+01	6.164E+01	6.162E+01
β_4	1.385E+02	1.405E+02	1.404E+02
β_5	7.078E+01	7.191E+01	7.188E+01
β_6	2.542E+01	2.585E+01	2.585E+01
β_{eff}	3.738E+02	3.791E+02	3.789E+02
λ_1	1.331E-02	1.331E-02	1.331E-02
λ_2	3.055E-02	3.056E-02	3.056E-02
λ_3	1.191E-01	1.191E-01	1.191E-01
λ_4	3.178E-01	3.178E-01	3.178E-01
λ_5	9.636E-01	9.635E-01	9.635E-01
λ_6	3.022E+00	3.023E+00	3.023E+00
Λ	2.670E-07	2.707E-07	2.704E-07

for an infinite amount of time, this is a valid assumption when looking at the decay heat over the first few minutes or hours following a transient as the short-lived fission products are the largest contributors to short-term decay heat and reach equilibrium concentrations very quickly. In the case of BOC operation after several hours or days, long-lived fission products that do not provide noticeable contributions to short-term decay heat will not have had a chance to build up in the fresh fuel. However, using the infinite irradiation decay heat standard is a conservative approximation.

Transient simulation models in RELAP5-3D require the fraction of total power that is generated in each of the four key isotopes. The fraction of power attributed to each isotope is proportional to the fission rate per isotope. There will be a small error associated with the power generated by the minor actinides. Table 28 lists the normalized isotopic fission rates for each core at all reference points in the fuel cycle.

This data was entered into RELAP5-3D transient simulation models. Decay heat as a function of time was very similar for all cores. The average of these nine decay heat curves as a percentage of nominal reactor power is summarized in Table 29 and

Table 26: Delayed neutron parameters for the Oxide S-PRISM core

	Oxide		
	BOC	MOC	EOC
β_1	8.038E+00	8.122E+00	8.121E+00
β_2	6.883E+01	6.956E+01	6.955E+01
β_3	5.911E+01	5.974E+01	5.974E+01
β_4	1.319E+02	1.335E+02	1.335E+02
β_5	6.617E+01	6.699E+01	6.698E+01
β_6	2.329E+01	2.359E+01	2.359E+01
β_{eff}	3.574E+02	3.615E+02	3.615E+02
λ_1	1.330E-02	1.330E-02	1.330E-02
λ_2	3.051E-02	3.051E-02	3.051E-02
λ_3	1.189E-01	1.189E-01	1.189E-01
λ_4	3.176E-01	3.177E-01	3.177E-01
λ_5	9.711E-01	9.710E-01	9.710E-01
λ_6	3.016E+00	3.016E+00	3.016E+00
Λ	2.870E-07	2.907E-07	2.906E-07

includes power generation from delayed neutrons.

Table 27: Delayed neutron parameters for the Nitride S-PRISM core

	Nitride		
	BOC	MOC	EOC
β_1	8.222E+00	8.349E+00	8.348E+00
β_2	7.019E+01	7.130E+01	7.130E+01
β_3	6.072E+01	6.167E+01	6.167E+01
β_4	1.372E+02	1.395E+02	1.395E+02
β_5	6.971E+01	7.088E+01	7.087E+01
β_6	2.484E+01	2.526E+01	2.526E+01
β_{eff}	3.709E+02	3.769E+02	3.769E+02
λ_1	1.331E-02	1.331E-02	1.331E-02
λ_2	3.054E-02	3.054E-02	3.054E-02
λ_3	1.191E-01	1.191E-01	1.191E-01
λ_4	3.178E-01	3.178E-01	3.178E-01
λ_5	9.658E-01	9.659E-01	9.659E-01
λ_6	3.019E+00	3.019E+00	3.019E+00
Λ	2.410E-07	2.462E-07	2.462E-07

Table 28: Normalized isotopic fission rates

	Metal			Oxide			Nitride		
	BOC	MOC	EOC	BOC	MOC	EOC	BOC	MOC	EOC
Pu^{241}	0.105	0.105	0.087	0.115	0.115	0.101	0.1095	0.109	0.094
Pu^{239}	0.682	0.678	0.707	0.694	0.692	0.712	0.6856	0.683	0.707
U^{238}	0.160	0.164	0.161	0.142	0.143	0.143	0.1545	0.157	0.156
U^{235}	0.053	0.054	0.045	0.049	0.049	0.044	0.0504	0.051	0.044

Table 29: Average decay heat power generation

Time (s)	Average Decay Heat Power (%)
1	7.737
5	5.918
10	5.086
50	3.520
100	2.971
500	2.109
1,000	1.782

CHAPTER VI

RELAP5-3D SIMULATIONS

6.1 RELAP5-3D Computational Model

Steady-state models were created in RELAP5-3D for Metal, Oxide and Nitride cores at BOC, MOC and EOC for a total of nine models. Using the point kinetics method, RELAP5-3D simulates the fission, actinide decay and fission product decay power generation at each time step during the simulation period. RELAP5-3D automatically determines the necessary time step size as a function of the stable or changing conditions of the simulation. For the S-PRISM transient simulations the minimum time step was 10-7 seconds.

The schematic in Figure 10 illustrates the coolant flow path throughout the S-PRISM reactor in the RELAP5-3D simulation model. In the primary coolant loop, sodium exiting the upper plenum in the core travels more than eight meters up around the control rod mechanism before traveling back down through one of the two intermediate heat exchangers (IHX). At the bottom of the reactor vessel the coolant reverses direction to travel up through the shield and reflector assemblies, which are not modeled in the thermal hydraulics model, towards one of four electromagnetic pumps. The sodium exits from the pumps in one of four discharge pipes and heads back towards the lower plenum of the core where it is distributed among the five representative assembly types, which are discussed below. The sodium pressure on the outlet side of the primary loop pumps is 1.1 MPa.

The model of the intermediate sodium coolant loop is simpler than the primary loop. The intermediate loop includes the IHX, intermediate EM pumps, and the Steam Generator. The secondary water loop has an inlet boundary condition of

water at 499.1 K and an outlet boundary condition of a vapor-liquid mixture at 624.0 K.

The RELAP5-3D simulation model accounts for all fuel pins in five representative assembly types: average and hot driver fuel, average and hot internal blanket and average radial blanket assemblies. The driver fuel and internal blanket assemblies experience stronger radial peaking than the radial blanket assemblies and were split into two assembly types to track peak behavior. The mesh used in the modeling of fuel pins divides each fuel pin into eight axial heat structures and nine radial mesh points. The nine mesh points encompass five meshes for the fuel, one for the gap and two for the cladding with symmetric boundary conditions at the center of the pin.

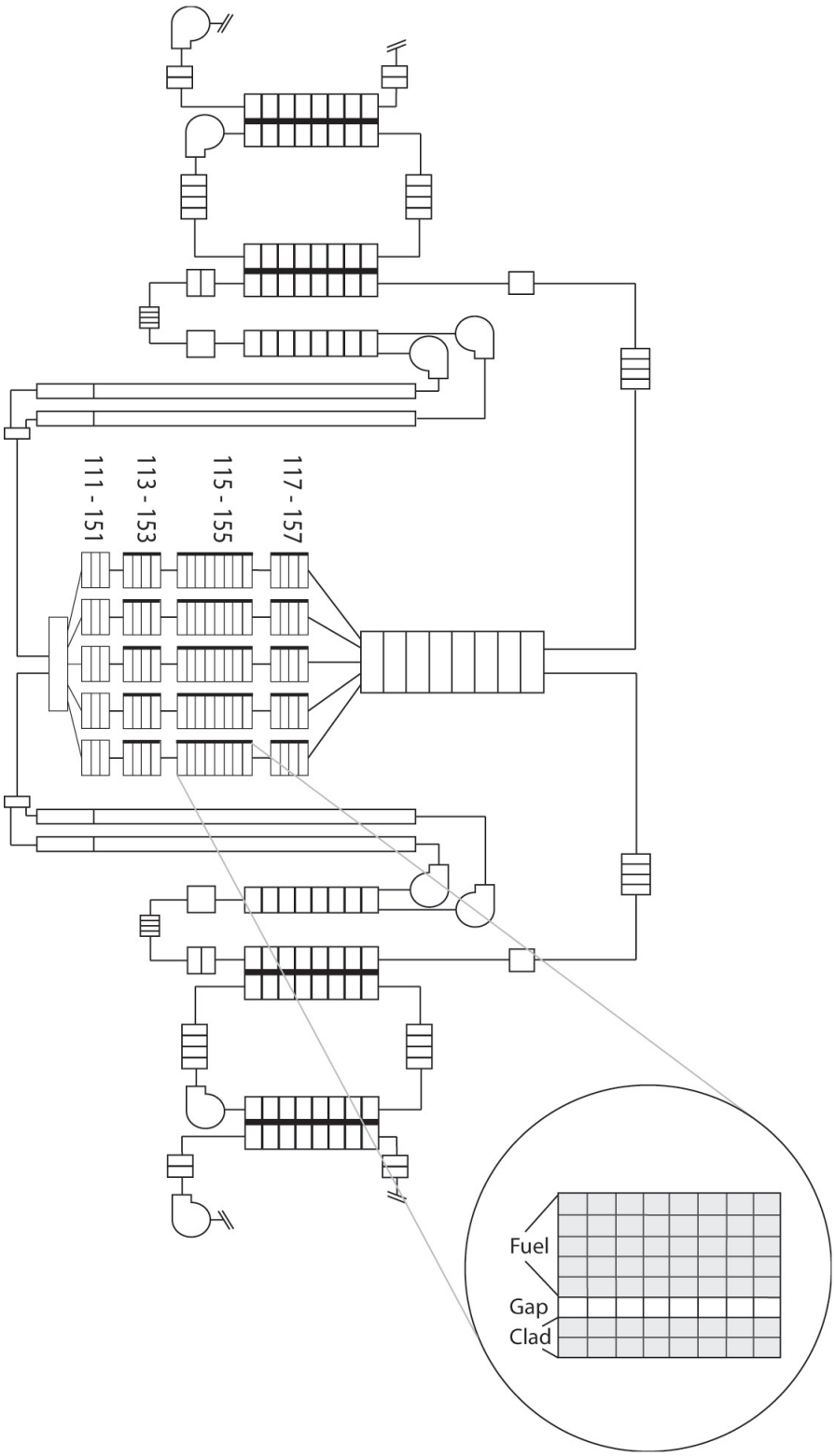

Figure 10: RELAP5-3D calculational model

Outside of the lower plenum, core and upper plenum, the heat removal system is identical in all core models. Data from Section 5.1 on the geometry and power per assembly was used to generate the nine different cores in RELAP5-3D. Important driver fuel (DF), internal blanket (IB) and radial blanket (RB) assembly parameters and temperatures for the nine cores are given in Tables 30, 31 and 32. Linear power values listed represent the average over all assemblies covered by that representative assembly type.

Table 30: Steady-state core parameters of the Metal core

	Metal		
	BOC	MOC	EOC
# Ave. DF Assemblies	114	114	114
# Hot DF Assemblies	24	24	24
# Ave. IB Assemblies	37	37	37
# Hot IB Assemblies	12	12	12
# Ave. RB Assemblies	48	48	48
Ave. DF Linear Power	19.28	18.88	18.68
Hot DF Linear Power	24.07	24.54	25.01
Ave. IB Linear Power	25.06	26.19	26.81
Hot IB Linear Power	27.13	28.97	30.36
Ave. RB Linear Power	11.57	11.76	11.46
Ave. DF Outlet Temp.	793.82	795.35	793.66
Hot DF Outlet Temp.	763.61	759.00	761.33
Ave. IB Outlet Temp.	757.13	760.49	763.37
Hot IB Outlet Temp.	761.77	766.74	772.92
Ave. RB Outlet Temp.	835.22	830.74	825.86
Ave. DF Peak Fuel Temp.	885.33	884.07	881.59
Hot DF Peak Fuel Temp.	891.23	890.63	895.12
Ave. IB Peak Fuel Temp.	868.88	877.12	882.30
Hot IB Peak Fuel Temp.	882.80	895.69	907.04
Ave. RB Peak Fuel Temp.	881.59	877.97	872.05

In a fast reactor the inlet nozzle at the base of the fuel assembly allows for fine control of how much coolant flows through each assembly. The size of these nozzles cannot be changed during normal operation and must be set during a reactor refueling period and maintained throughout the fuel batch cycle. In RELAP5-3D simulations, there is not an inlet nozzle component that allows for fine control over the inlet flow

Table 31: Steady-state core parameters of the Oxide core

	Oxide		
	BOC	MOC	EOC
# Ave. DF Assemblies	150	150	150
# Hot DF Assemblies	12	12	12
# Ave. IB Assemblies	55	55	55
# Hot IB Assemblies	18	18	18
# Ave. RB Assemblies	60	60	60
Ave. DF Linear Power	15.58	15.23	14.90
Hot DF Linear Power	20.67	20.24	19.85
Ave. IB Linear Power	13.50	14.69	15.80
Hot IB Linear Power	15.78	17.28	18.64
Ave. RB Linear Power	4.95	5.06	5.16
Ave. DF Outlet Temp.	795.30	791.73	788.43
Hot DF Outlet Temp.	762.83	760.22	757.88
Ave. IB Outlet Temp.	751.17	761.17	770.51
Hot IB Outlet Temp.	745.52	755.74	765.05
Ave. RB Outlet Temp.	846.39	851.24	855.57
Ave. DF Peak Fuel Temp.	1,196.0	1,180.5	1,166.4
Hot DF Peak Fuel Temp.	1,346.3	1,327.7	1,311.2
Ave. IB Peak Fuel Temp.	1,070.6	1,117.1	1,161.2
Hot IB Peak Fuel Temp.	1,137.6	1,196.0	1,251.5
Ave. RB Peak Fuel Temp.	921.90	929.11	935.56

conditions. Instead, when the coolant splits in the thermal hydraulics model into individual assembly flow paths at the lower plenum, proper flow conditions are imposed on the coolant by modifying the hydraulic diameter and flow area of the coolant pipes to create the necessary hydraulic resistance for each assembly inlet. Since these flow conditions must be maintained at BOC, MOC and EOC, conditions which produced low coolant outlet and peak fuel temperatures across the five assemblies during the fuel cycle were chosen. The hot driver fuel and hot internal blanket assemblies were given a larger fraction of the total mass flow than the other assemblies due to higher linear powers which lead to higher centerline temperatures.

Table 32: Steady-state core parameters of the Nitride core

	Nitride		
	BOC	MOC	EOC
# Ave. DF Assemblies	96	96	96
# Hot DF Assemblies	18	18	18
# Ave. IB Assemblies	61	61	61
# Hot IB Assemblies	6	6	6
# Ave. RB Assemblies	54	54	54
Ave. DF Linear Power	20.99	20.14	19.38
Hot DF Linear Power	26.42	25.89	25.37
Ave. IB Linear Power	16.20	18.24	20.08
Hot IB Linear Power	17.76	20.23	22.46
Ave. RB Linear Power	7.23	7.54	7.82
Ave. DF Outlet Temp.	791.32	785.11	779.56
Hot DF Outlet Temp.	778.01	775.17	772.40
Ave. IB Outlet Temp.	761.19	776.76	790.77
Hot IB Outlet Temp.	750.65	766.39	780.66
Ave. RB Outlet Temp.	820.75	828.48	835.38
Ave. DF Peak Fuel Temp.	968.29	955.79	944.59
Hot DF Peak Fuel Temp.	1,014.4	1,007.4	1,000.6
Ave. IB Peak Fuel Temp.	888.17	917.73	944.11
Hot IB Peak Fuel Temp.	895.16	928.37	958.14
Ave. RB Peak Fuel Temp.	858.96	868.15	876.33

6.1.1 Designing the Intermediate Heat Exchanger and Steam Generator

The S-PRISM literature does not include a detailed design of the intermediate heat exchanger so it was necessary to design a new one for the transient simulations. While the final IHX design did not match the inlet and outlet temperatures on the intermediate side of the IHX that were given in the S-PRISM literature, these temperatures were used as a guideline in the design of the new IHX. Primary loop IHX inlet and outlet temperatures were conserved.

The IHX design used in the modeling and simulation of S-PRISM transients is loosely based on the PFBR IHX design detailed in Reference [28]. Differences include the mass flow rate of sodium in the intermediate loop and number of coolant tubes in the IHX to account for a higher thermal output. PFBR's IHX is a counter-flow U-shaped heat exchanger with intermediate sodium entering from the top, passing

through a central tube and then returning up through 3600 tubes. The simplified S-PRISM IHX design is purely counter-flow with intermediate hot sodium entering the IHX from the bottom and traveling upward through 5700 tubes, while the primary loop sodium entering from the top travels down across the coolant tubes. The primary loop IHX inlet and outlet temperatures have been preserved at 783.9 K and 636.7 K. The sodium inlet temperature in the intermediate loop is 591.8 K and the outlet temperature is 755.1 K. Important intermediate heat exchanger parameters are given in Table 33. During steady-state operation the sodium takes 71 seconds to travel the primary loop and 24 seconds for the intermediate loop.

Table 33: Intermediate heat exchanger parameters

# Pipes	5700
Thermal Requirement (MWt)	500
Primary Mass Flow Rate (kg/s)	2901.8
Intermediate Mass Flow Rate (kg/s)	2620.0
Pipe Inner Radius (m)	0.0087
Pipe Outer Radius (m)	0.0095
IHX Length (m)	8.305
Primary Inlet Temperature (K)	783.9
Primary Outlet Temperature (K)	636.7
Intermediate Inlet Temperature (K)	591.8
Intermediate Outlet Temperature (K)	755.1
Primary Loop Temperature Change (K)	147.2
Intermediate Loop Temperature Change (K)	163.3

The Steam Generator design is based on the IHX design with changes to account for feed water as the working fluid in the secondary loop and its lower inlet temperature. While in the IHX the cold leg temperatures of the primary and intermediate loops differ by only 45 K, the temperature difference jumps to nearly 100 K in the steam generator. The parameters of the steam generator are given in Table 34.

6.1.2 Control Rods and Gas Expansion Modules

When fully inserted into the core, S-PRISM's control rods are expected to provide negative \$13 of reactivity [14]. A physical maximum withdrawal rate is imposed on the

Table 34: Steam generator parameters

# Pipes	2280
Thermal Requirement (MWt)	500
Intermediate Mass Flow Rate (kg/s)	2620.0
Secondary Mass Flow Rate (kg/s)	450.6
Pipe Inner Radius (m)	0.0089
Pipe Outer Radius (m)	0.0095
IHX Length (m)	8.305
Secondary Inlet Temperature (K)	493.1
Secondary Outlet Temperature (K)	624.0
Secondary Loop Temperature Change (K)	130.9

control rods by the rod stop mechanism and for conservatism this rate was also applied to control rod insertion with the drive mechanism. The electronically positioned rod stop mechanism is attached to the control rod drive mechanism preventing reactivity insertions during control rod withdrawal in excess of \$0.20. To be safe this limit is generally assumed to be \$0.30 [7].

The scram point used by S-PRISM's reactor protection system is set at 113% of nominal full power [14]. When 113% power is achieved, the control rods are fully inserted following an assumed two second delay. If instead of being inserted by the drive mechanism the control rods are gravity-fed into the core, full insertion is required to occur in less than two seconds, even with full coolant mass flow. Transients simulating this rapid scram also used a more conservative insertion rate, assuming that gravity feeding of the control rods occurs in four seconds.

The reactivity insertion provided by the Gas Expansion Modules (GEM) during loss of primary coolant flow accidents was examined in several transient scenarios. Following a trip of the primary sodium pumps, the GEM assemblies rapidly void, increasing neutron leakage in the core. The reactivity insertion due to complete voiding of the GEM assemblies is negative \$1.4 [14]. Transients that included the reactivity insertion from GEM modules used a feedback that is proportional to the decrease in the coolant mass flow rate. Equation 16 was used to determine the

reactivity insertion due to a reduction in primary coolant mass flow.

$$\rho_{GEM} = \frac{\dot{m}_0 - \dot{m}(t)}{\dot{m}_0} \cdot (-\$1.4) \tag{16}$$

6.2 Transient Simulations

A series of transient simulations were performed in RELAP5-3D to determine which S-PRISM core is most capable of surviving serious accidents. Transients ranging from loss of pumping power to control rod withdrawal were simulated for the Metal, Oxide and Nitride S-PRISM cores at BOC, MOC and EOC.

Each S-PRISM core was evaluated based on its capability to withstand three failure criteria: fuel melting, clad melting and coolant boiling. While coolant boiling would not necessarily result in catastrophic damage to the reactor, it is a good indicator that the transient is progressing towards a much worse outcome. Fuel and clad melting, however, will necessitate core shut down and costly repairs, if not permanent reactor shut down, and are considered unacceptable for all anticipated transients. There are interesting phenomena that occur following fuel or clad melting but RELAP5-3D is unable to model these processes, which must be considered in future work.

At atmospheric pressure sodium boils at 1,156 K. With pressures at or below 1.1 MPa in the primary loop, coolant boiling occurs at higher temperatures. Clad melting occurs at 1,755 K and fuel melting occurs at 1,350 K, 3,023 K and 3,035 K in the Metal, Oxide and Nitride cores, respectively. These were the limits imposed on the S-PRISM cores during the transient simulations.

For each transient, the total increase or decrease in the thermal power was tracked as was the fuel temperature increase relative to the melting temperature. Δ RFT, given by Equation 17, represents the smallest margin to fuel melting reached during a

transient divided by the steady-state margin to fuel melting. This parameter reflects that a 200 K fuel temperature increase in the Metal core would be far more severe than a 200 K increase in the other cores due to different melting temperatures. A value of zero indicates that the peak fuel temperature did not increase during the transient and a value of one indicates fuel melting has occurred.

$$\Delta RFT = max_{t \geq 0} \left[\frac{T_{fuel}^{max}(t) - T_{fuel}^{max}(0)}{T_{fuel}^{melt} - T_{fuel}^{max}(0)} \right] \tag{17}$$

Figures illustrating each core's performance during a transient use data from one of BOC, MOC or EOC simulations, whichever point in the fuel cycle experienced the most severe temperatures. cores at steady-state. Because of the clad's high melting temperature, maximum clad temperatures are only noted in the event that clad melting occurs. In each case, the maximum coolant temperature occurs at the outlet of the radial blanket assembly because, with a lower linear power, those assemblies can maintain an acceptable centerline temperature with a smaller mass flow rate leading to high outlet temperatures. In seven of the cores, the peak fuel temperature occurred in the hot driver fuel assemblies. The exceptions were the MOC and EOC Metal cores where the peak fuel temperature occurred in the hot internal blanket assembly.

Table 35: Transient comparison criteria for S-PRISM cores at steady-state

	T_{fuel}^{max} (K)	Δ RFT	T_{cool}^{max} (K)	Δ P (MWt)
Metal (BOC)	891.2	0.0	835.2	0.0
Metal (MOC)	895.7	0.0	830.7	0.0
Metal (EOC)	907.0	0.0	825.9	0.0
Oxide (BOC)	1,346.3	0.0	846.4	0.0
Oxide (MOC)	1,327.7	0.0	851.2	0.0
Oxide (EOC)	1,311.2	0.0	855.6	0.0
Nitride (BOC)	1,014.4	0.0	820.7	0.0
Nitride (MOC)	1,007.4	0.0	828.5	0.0
Nitride (EOC)	1,000.6	0.0	835.4	0.0

Each of the simulated transients can be classified in one of three categories: anticipated transients with scram, anticipated transients without scram and beyond design

basis accidents. Anticipated transients with scram are designed to test the reactor's response to transients where the reactor operators can scram the core at any moment. Anticipated transients without scram are expected transients where reactivity insertions from scram are unavailable but GEM reactivity insertions are available for failures of primary coolant pumps. Finally, Beyond Design Basis Accidents include transients where both GEM and scram reactivity insertions are unavailable. The transients listed below are described in detail in the following sections. All transients were simulated without the aid of the Reactor Vessel Auxiliary Cooling System.

1. Anticipated Transients With Scram
    (a) Over-power to scram
    (b) Establishment of natural circulation tests
        i. LOFA with scram
        ii. LOFA + LOHSA with scram.
2. Anticipated Transients Without Scram
    (a) Unprotected all-rods withdrawal
    (b) LOFA with GEM
        i. Single/multiple pump failure
    (c) LOHSA
        i. Single/multiple pump failure
        ii. Single pump seizure/blockage
    (d) LOHSA-SL
3. Beyond Design Basis Events:
    (a) Unprotected transient over-power accident
    (b) LOFA without GEM or scram
        i. Single/multiple pump failure

ii. Single pump seizure/blockage

(c) LOPA without GEM or scram

6.2.1 Control Rod Transients

Three different transients related to an accidental withdrawal of the control rods were simulated. The first transient simulates the control rods withdrawing until the 113% of full power scram point is reached. The control rods are subsequently fully inserted into the core. The second transient simulates the control rods withdrawing the rod stop limit of \$0.30 and stopping. The third transient simulates the control rods withdrawing past the rod stop.

Rapid control rod ejection was not examined based on information in Reference [7]. As the control rods are inserted into the core, they are closely followed by their driving motors which contain the rod stop mechanism, preventing control rods from withdrawing back out of the core. Because the reactor will remain shut down with a single secondary control rod or two primary control rods inserted into the core, eleven or twelve control rods would need to simultaneously eject past their individual rod stop mechanisms for supercriticality to be possible, a very implausible event.

6.2.1.1 Over-power to scram

The first anticipated transient with scram is the Over-power to scram accident. In this transient the control rods are withdrawn at the physical maximum rate of \$0.02/s until the reactor protection system recognizes that 113% of nominal full-power has been reached. After a two second delay to trip the control rods, a full scram is simulated at negative \$0.02/s. 113% of full-power was reached between 4.5 and 4.9 seconds after the start of the transients in the various cores. Therefore, control rod reinsertion occurs 6.5-6.9 seconds after the start of the transient. With each core experiencing the same power increase prior to scram, this transient was run to

determine which core would experience the smallest temperature increases before the control rods reinsert. The temperature and power increases experienced during the Over-power to scram transient are summarized in Table 36.

Due to its low thermal conductivity, the Oxide core experienced the highest peak fuel temperature at 1,492.2 K at BOC, versus 957.1 for the Metal core at EOC and 1,079.8 K for the Nitride core at BOC. The maximum coolant temperatures were 855.6, 862.8 and 851.2 for the Metal, Oxide and Nitride cores, respectively. While the Oxide core experienced the greatest increase in fuel and coolant temperatures, its reactivity feedbacks limited the thermal power increase during the two seconds following 113% power more than the other two cores.

The Nitride core also performed well with a relative fuel temperature increase of only three percent, much lower than the eight percent and ten percent values for the Oxide and Metal cores, respectively. This is due to the high melting temperature and thermal conductivity of the Nitride fuel. The Metal core experienced the largest increases in relative fuel temperature and thermal power during this transient. Figure 11 illustrates maximum fuel temperatures during the first fifty seconds of the Over-power to scram transient.

Table 36: Results of over-power to scram transient

	T_{fuel}^{max} (K)	Δ RFT	T_{cool}^{max} (K)	Δ P (MWt)
Metal (BOC)	939.1	0.104	855.6	210.2
Metal (MOC)	941.0	0.100	850.5	205.0
Metal (EOC)	957.1	0.113	846.2	214.7
Oxide (BOC)	1,494.2	0.088	853.5	192.7
Oxide (MOC)	1,463.9	0.080	858.2	187.1
Oxide (EOC)	1,443.7	0.077	862.8	190.3
Nitride (BOC)	1,079.8	0.032	835.7	204.1
Nitride (MOC)	1,071.0	0.031	843.8	202.0
Nitride (EOC)	1,063.4	0.031	851.2	202.1

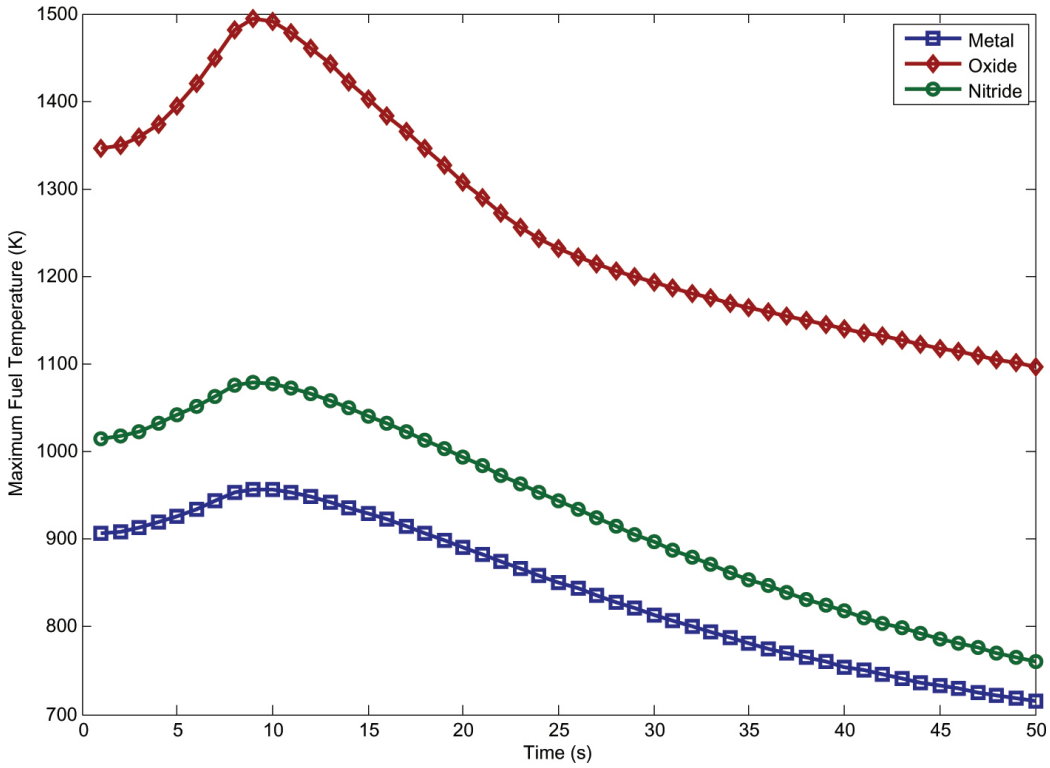

Figure 11: Maximum fuel temperature during over-power to scram transient

6.2.1.2 Unprotected All-Rods Withdrawal

In the anticipated transient without scram Unprotected All-Rods Withdrawal, the control rods are withdrawn to the rod stop limit of \$0.3 at the physical maximum rate of \$0.02/s. In this transient there is no control rod scram and reactivity feedbacks are solely responsible for bringing the transient under control. The purpose of this transient is to determine which core would experience the smallest increase in thermal power due to a large reactivity insertion.

The results of the Unprotected All-Rods Withdrawal are summarized in Table 37. While the Oxide core experienced the highest fuel temperatures during this transient, its reactivity feedbacks provided the strongest counter to the \$0.3 of reactivity from the control rod withdrawal. The 555 MW increase in the BOC Oxide core is far less than the 1,001 and 1,609 MW increases in the Nitride and Metal cores, respectively. However, relative to its melting temperature, the Nitride core experienced the smallest

increase in fuel temperature at less than 20%. The Oxide core also performed well in this area with a reduction in the margin to fuel melting of only 30%.

The Metal core clearly underperformed compared to the other two fuel types. While the BOC and MOC cores did not exceed any of the failure criteria, the thermal power of the fission core more than doubled in both cases. The EOC Metal core, however, experienced fuel melting in the Hot Internal Blanket Assembly 88 seconds after the start of the transient. With an increase of more than 1,604 MW, the EOC Metal core's reactivity feedbacks were not able to counter the \$0.3 of reactivity from the control rod withdrawal.

Table 37: Results of unprotected all-rods withdrawal

	T_{fuel}^{max} (K)	Δ RFT	T_{cool}^{max} (K)	Δ P (MWt)
Metal (BOC)	1,260.8	0.806	1,156.9	1,353.6
Metal (MOC)	1,207.0	0.685	1,099.6	1,154.3
Metal (EOC)	$>$ 1,350.0	$>$ 1.000	$>$ 1,175.4	$>$ 1,604.2
Oxide (BOC)	1,895.6	0.328	972.7	555.4
Oxide (MOC)	1,825.0	0.293	971.4	519.5
Oxide (EOC)	1,812.0	0.293	981.7	535.3
Nitride (BOC)	1,351.8	0.167	1,029.3	961.8
Nitride (MOC)	1,328.8	0.159	1,036.5	933.5
Nitride (EOC)	1,342.6	0.168	1,065.2	1,000.7

Figure 12 illustrates the thermal power increase during the transient. Maximum reactivity is achieved at 15 seconds when the control rods reach the rod stop followed by a rapid decrease in reactivity provided by the feedbacks. After 1,000 seconds, the power and temperatures in the Oxide and Nitride cores have leveled off. At this time, the Nitride core is at 1,627 MW with a maximum fuel temperature of 1,311 K while the Oxide core is at 1,410 MW and a maximum fuel temperature of 1,845 K. While unacceptable for prolonged periods of operation, both cores are still a safe margin from fuel melting. Figure 13 includes the maximum fuel temperatures, illustrating the Metal core's progression to fuel melting during the Unprotected All Rods Withdrawal transient.

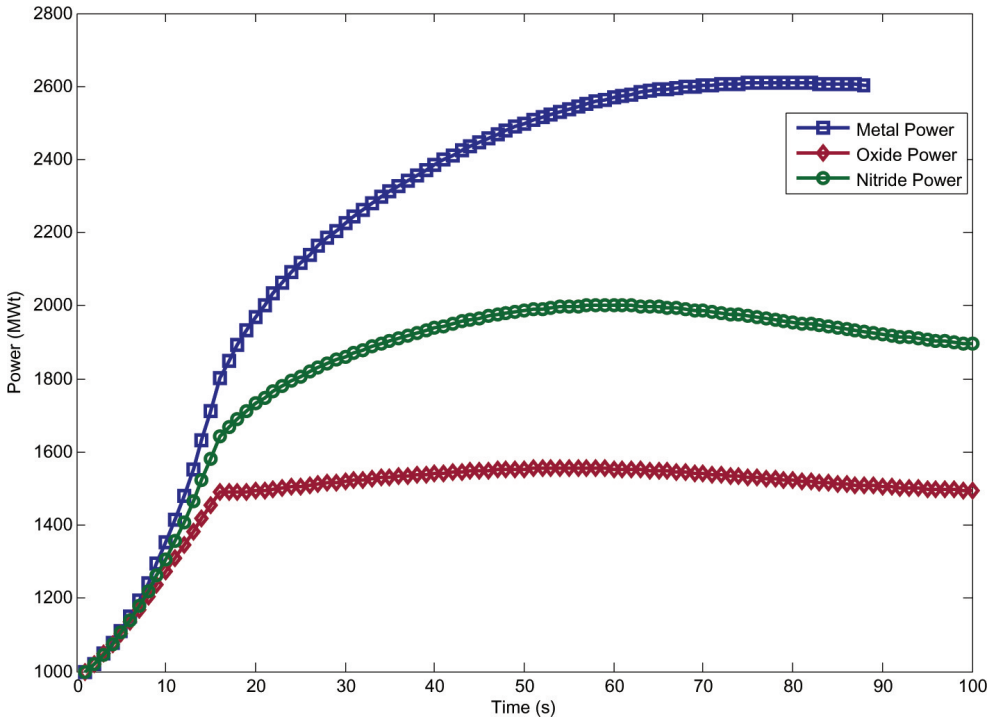

Figure 12: Power during unprotected all-rods withdrawal. Metal simulation ends when fuel melting occurs.

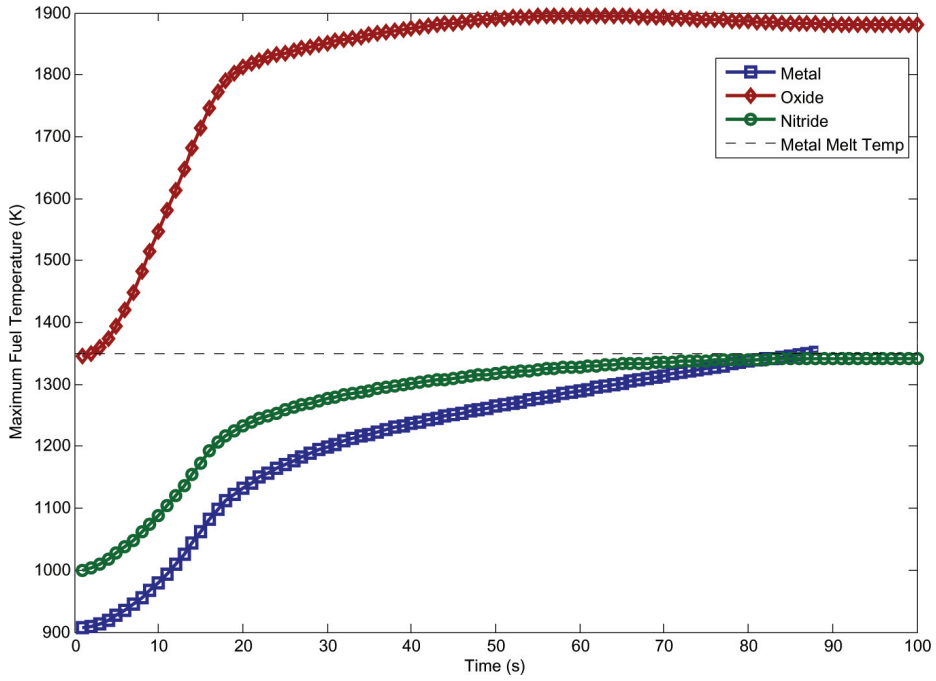

Figure 13: Peak fuel temperatures during unprotected all-rods withdrawal. Metal simulation ends when fuel melting occurs.

6.2.1.3 Unprotected Transient Over-Power Accident

The final control rod transient, Unprotected Transient Over-Power Accident (UTOPA), is considered beyond design basis because the rod stop at \$0.3 is assumed to fail and the control rods continue to withdraw at \$0.02/s past that limit. Melting of either the fuel or cladding is guaranteed in this accident simulation because reactivity feedbacks can only provide a limited negative reactivity and the control rods are assumed to withdraw at the constant rate until melting occurs. This transient is designed to see how long each core can withstand a continuous external reactivity insertion.

The Metal core was fastest to fail during the Unprotected Transient Over-Power Accident with fuel melting occurring approximately 30 seconds after the start of the transient. The Oxide core was able to sustain the transient for nearly twice as long. On average, fuel melting in the Oxide core occurred 57 seconds after the start of the transient. Unlike in the Metal core where different assemblies were first to fail at

the different fuel cycle points, the Hot Driver Fuel assembly was first to fail for all three Oxide cores. A few extra seconds before fuel melting occurs could probably be achieved with a modified coolant flow distribution but the benefits would not be enough to improve Oxide core performance to the level of the Nitride core.

The Nitride core was the strongest during the UTOPA with clad melting occurring an average of 70 seconds after the start of the transient. Because of the very high thermal conductivity and melting temperature of the Nitride fuel, the clad melting temperature was surpassed before the Nitride fuel's melting temperature. The largest Nitride temperature, 2,567 K, was achieved during MOC operation in the Hot Driver Fuel assembly. With a margin of almost 500 K, the Nitride core could withstand a UTOPA for several additional tens of seconds if a clad with a higher melting temperature was used. Figures 14 and 15 illustrate the progression of this transient in the different cores.

Table 38: Results of unprotected transient over-power accident

	Time to Failure (s)	Failure Mode	Which Assembly
Metal (BOC)	30.4	Fuel Melting	Hot Driver Fuel
Metal (MOC)	33.2	Fuel Melting	Average Driver Fuel
Metal (EOC)	27.3	Fuel Melting	Hot Internal Blanket
Oxide (BOC)	53.1	Fuel Melting	Hot Driver Fuel
Oxide (MOC)	58.6	Fuel Melting	Hot Driver Fuel
Oxide (EOC)	58.7	Fuel Melting	Hot Driver Fuel
Nitride (BOC)	70.9	Clad Melting	Average Driver Fuel
Nitride (MOC)	73.3	Clad Melting	Radial Blanket
Nitride (EOC)	66.8	Clad Melting	Radial Blanket

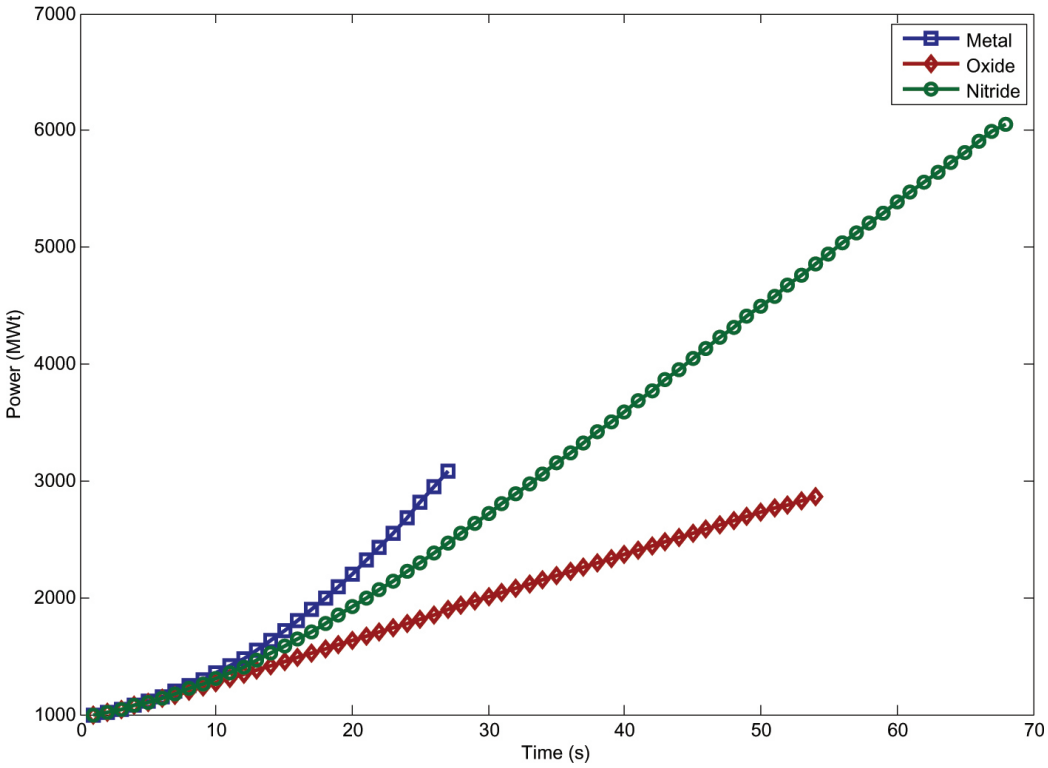

Figure 14: Power during unprotected transient over-power accident. The simulation ends when fuel or clad melting occurs.

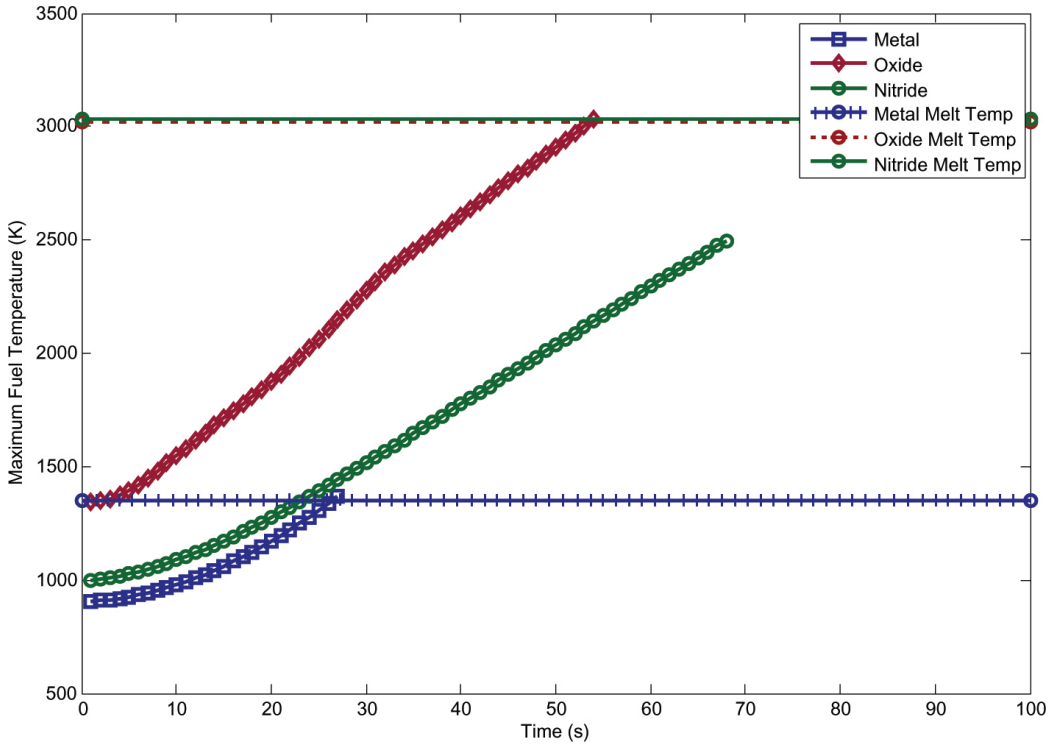

Figure 15: Peak fuel temperatures during unprotected transient over-power accident. The simulation ends when fuel or clad melting occurs.

6.2.1.4 Control Rod Transients Summary

During the three control rod withdrawal transients, Over-power to scram, Unprotected All-Rods Withdrawal and Unprotected Transient Over-Power, the Metal experienced fuel melting faster than the other cores. In the Over-Power to scram transient, the Metal core experienced the largest power and relative fuel temperature increases. In the Unprotected All-Rods Withdrawal accident, the EOC Metal core achieved fuel melting while the Oxide and Nitride cores were closer to their steady-state temperatures than their melting temperatures. Finally, in the Unprotected Transient Over-Power Accident, the Metal core experienced fuel melting in only 30 seconds.

The Oxide and Nitride cores performed very well during the control rod transients. The Oxide core's reactivity feedbacks provided a stronger counter to the positive control rod reactivity insertions while the Nitride core's much higher thermal

conductivity created a larger margin to fuel melting. The difference between the Oxide and Nitride cores is illustrated in the final control rod accident where the Nitride core can withstand a constant reactivity addition for a longer period of time. While both cores performed acceptably, the Nitride core demonstrated larger limits to fuel or clad melting during control rod withdrawal transients.

6.2.2 Loss of Flow Accidents

Several transients related to the loss of primary pumping power were simulated. These range from transients designed to test the reactor's ability to establish effective decay heat removal via natural circulation to accidents where the core receives no external reactivity assistance to help counter decreases in coolant mass flow. Because power to the electromagnetic pumps is not guaranteed by safety grade systems, there is a high enough probability of failure of the EM pumps. Therefore, Loss of Flow and also Loss of Heat Sink transients are considered anticipated transients.

Two different coolant flow decay schemes were implemented for the primary coolant loop. In the first scheme, power to the coolant pumps is terminated allowing RELAP5-3D to determine how the mass flow rate decays due to hydraulic resistance in the coolant loop. In the primary loop, this resulted in a coolant flow coast down that was much more rapid than expected and is considered conservative as there is little information available about the flow conditions at the inlet and outlet to the reactor core so pressure losses do not necessarily reflect the true reactor conditions. Consequently, in the event that this rapid coolant flow coast down resulted in fuel melting, a second scheme was implemented to determine if a slower mass flow rate decay would allow the reactor to endure that transient. This decay scheme, given in Equation 18, specifies a mass flow rate halving time of six seconds to represent the slower coast down of the coolant mass flow rate.

$$\dot{m}(t) = \frac{\dot{m}_0}{1 + t/6} \tag{18}$$

It should be noted that with traditional centrifugal pumps, a flywheel is used to maintain pump rotation temporarily following a lost of pumping power. This guarantees a slower coast down of the coolant mass flow rate. Because there are no moving parts in an EM pump, the solution of using flywheel in the pump to provided limited pumping power after pump failure is not possible. However, one possibility is to provide power to the pump through a generator that is attached to a flywheel, slowing down the coolant mass flow rate decay.

6.2.2.1 Establishment of Natural Circulation Tests

Before Loss of Flow Accidents were simulated, several natural circulation tests were performed where coolant pumps were tripped simultaneously with a control rod scram to examine the core's ability to progress to and remove decay heat with limited coolant mass flow. These anticipated transients with scram were simulated as a complete loss of flow in either the primary loop or both the primary and intermediate loops accompanied by either a gravity-fed four second scram or a scram at the physical maximum insertion rate of negative \$0.02/s.

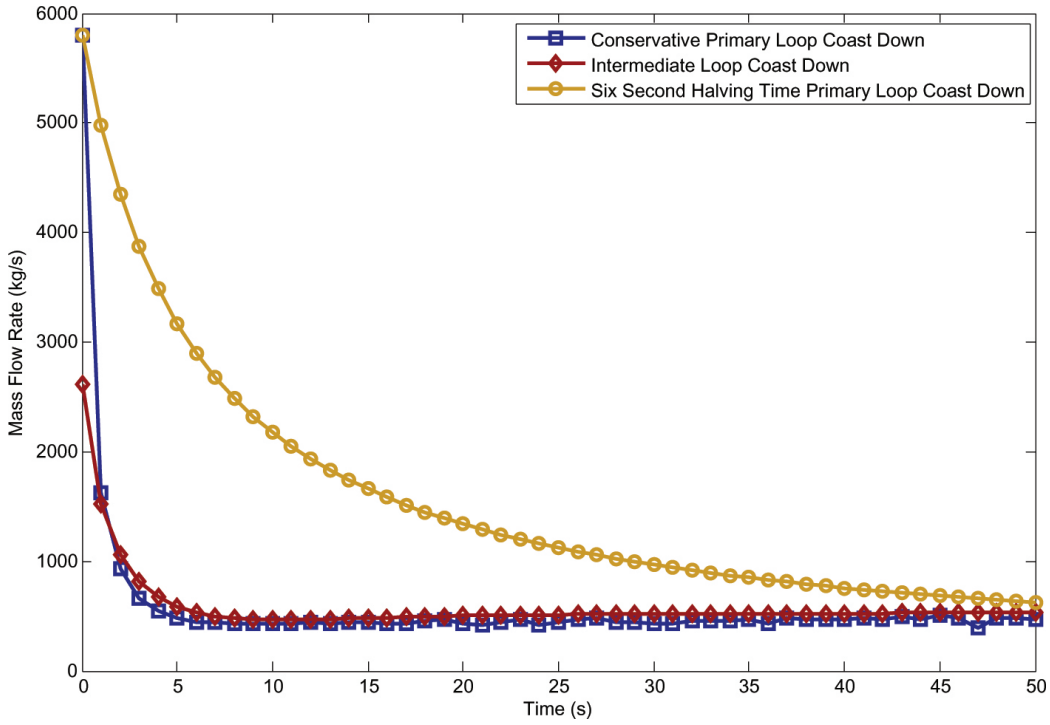

Figure 16: Coolant flow coast down during natural circulation tests

The first natural circulation test simulated a trip of the primary loop coolant pumps along with a gravity-fed four second scram. The conservative coolant mass flow rate coast down, which was used in this transient, represented an instantaneous loss of pumping power and is plotted in Figure 16. Because the mass flow rate decays for all cores were similar, the coolant profiles plotted in Figure 16 are an average over all cores. Very quickly, the flow rate dropped to about 8% of nominal as natural circulation in the primary loop is established. In this transient scenario with an immediate scram, the fission power, illustrated in Figure 17, drops to decay heat levels so rapidly that the fuel temperatures never rise above their nominal values during the transient. After 1,000 seconds, there was an average of 21.4 MW of decay heat power production and coolant outlet temperatures were at approximately 560 K in the fission core. All cores were successfully able to remove decay heat production as the reactor transitioned to purely decay heat production.

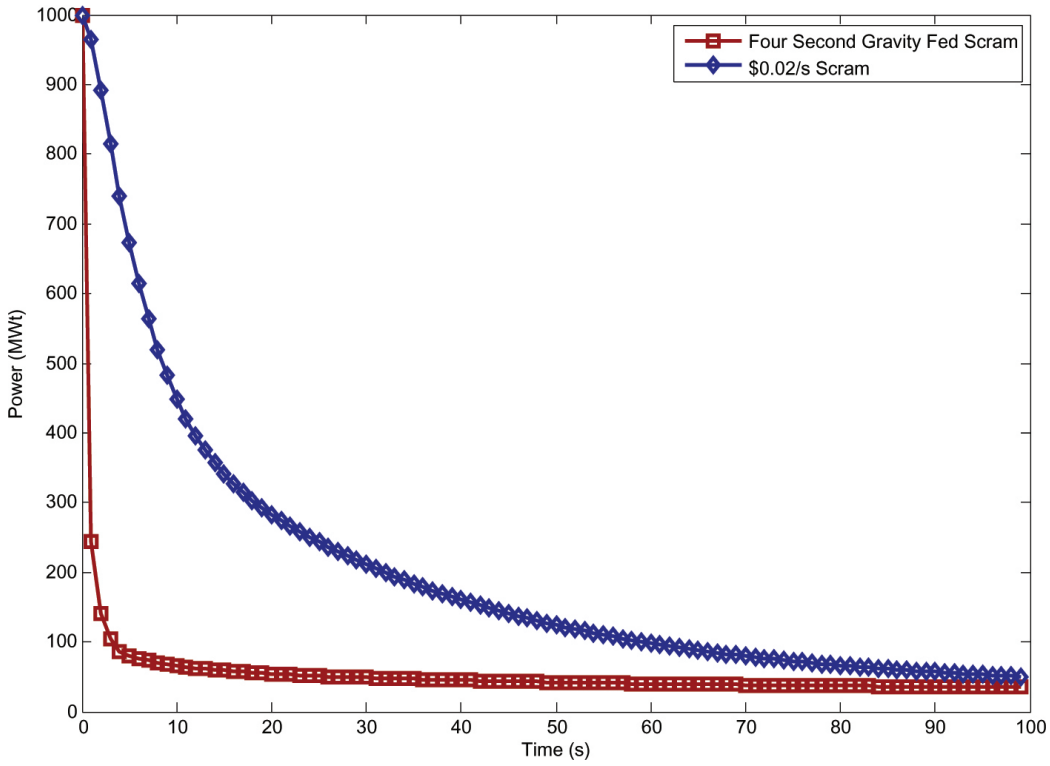

Figure 17: Thermal power following control rod scram and complete loss of pumping power

The second natural circulation test expanded the pump trip to include not just the primary loop pumps but also the intermediate loop pumps. This transient is a test of whether natural circulation in the primary and intermediate loops is sufficient to remove decay heat from the reactor core. The flow rate coast down in one of the intermediate loops following a pump trip is illustrated in Figure 16. There is less hydraulic resistance in the intermediate loop so the flow coasts down slower than in the primary loop. All cores were able to provide adequate decay heat removal from natural circulation in the primary and intermediate coolant loops. After 1,000 seconds the coolant mass flow rate in the intermediate loop is less than 6% of its nominal value. The average coolant outlet temperature is 565 K, five degrees higher than in the previous test.

In the third natural circulation test, the pumps were tripped simultaneously with

a control rod scram at the physical maximum rate of \$0.02/s. This test was designed to determine if a slower drop in power is enough to limit core temperatures in the initial stages of a pump trip or if the much faster gravity-fed scram is required. The Oxide and Nitride cores performed acceptably but the Metal core did not. Because the power does not drop fast enough during a \$0.02/s control rod scram, the Metal core was unable to maintain acceptable fuel temperatures. At six seconds, the Metal fuel's temperature has increased so quickly that the fuel melting temperature was exceeded. Unlike in the Oxide and Nitride cores where reactivity feedbacks are strong enough to expedite the drop in power, the Metal core's reactivity feedbacks are unable to provide the necessary power drop to avoid fuel melting. In the Oxide core the maximum fuel temperature achieved was 1,658.7 K. In the Nitride core the maximum fuel temperature was 1,476.5 K.

A final natural circulation test was performed to determine if a less conservative mass flow rate decay scheme would allow the Metal core to withstand fuel melting when the scram reactivity insertion rate was negative \$0.02/s. Core power during a negative \$0.02/s scram is shown in Figure 17. Using the less conservative six second halving time decay scheme for the coolant mass flow rate in the primary loop, the Metal core performed like the first test where fuel temperatures never exceeded their nominal steady-state values.

Because the Oxide and Nitride cores have stronger reactivity feedbacks that assist the control rod scram following a pump trip, both cores are able to sufficiently cool themselves via natural circulation, even if the control rods scram at the slower \$0.02/s rate. The Metal core, however, requires that the control rods are scrammed at the gravity-fed four second rate, otherwise fuel melting will quickly ensue. The other option to ensure core integrity in the Metal core is to slow down the mass flow rate decay following a loss of pump trip.

6.2.2.2 Loss of Flow Accidents with GEM

Loss of Flow Accidents (LOFA) with GEM were simulated as the failure of one or more of the four primary loop coolant pumps with a corresponding reactivity insertion provided by the Gas Expansion Module assemblies. The reactivity insertion provided by the GEM assemblies is governed by Equation 16 in Section 6.1.2. Because the GEM assemblies will rapidly void following a decrease in the coolant mass flow rate, there is no delay in the GEM reactivity insertion. These anticipated transients without scram used the conservative coolant coast down rate for all transients.

Due to the strong reactivity effect from the GEM assemblies, each S-PRISM core was capable of tolerating the failure of any number of primary loop EM pumps without exceeding failure limits. The GEM's rapid negative reactivity insertion leads to maximum fuel temperatures that do not increase until the four pump LOFA, and even then not at all in the Oxide core. Maximum coolant temperatures begin to rise during a one pump LOFA, but only very slightly. Even in the four pump LOFA, the maximum coolant temperature achieved in any core is 1,061 K, well below the sodium boiling temperature.

Because the GEM assemblies provide such a strong and rapid negative reactivity insertion, each S-PRISM core can withstand the very rapid drop in the coolant mass flow rate. Maximum temperatures obtained during the four pump LOFA are given in Table 39. A good indication of the comparatively weaker reactivity feedbacks in the Metal core is illustrated by the Oxide and Nitride cores reestablishing criticality 250 and 400 seconds, respectively, after the start of a one pump LOFA, while the Metal core in unable to reestablish criticality.

6.2.2.3 Loss of Flow Accidents without GEM

In this Beyond Design Basis Accident, a series of Loss of Flow Accidents were simulated without the reactivity assistance of the GEM assemblies. The transients were

Table 39: Results of complete LOFA with GEM

	T_{fuel}^{max} (K)	Δ RFT	T_{cool}^{max} (K)
Metal (BOC)	1,058	0.364	955
Metal (MOC)	1,076	0.398	949
Metal (EOC)	1,066	0.358	1,042
Oxide (BOC)	1,346	0.000	1,016
Oxide (MOC)	1,328	0.000	1,011
Oxide (EOC)	1,311	0.000	1,008
Nitride (BOC)	1,086	0.035	1,061
Nitride (MOC)	1,081	0.036	1,047
Nitride (EOC)	1,085	0.041	1,056

simulated as the failure of one or more of the four primary loop sodium pumps but unlike the previous transient, reactivity feedbacks are solely responsible for decreasing the thermal power and maintaining acceptable temperatures in the core. The conservative mass flow rate decay scheme was used in all simulations. In the event that the transient led to fuel melting, the six second halving time scheme was used to determine if a slower mass flow rate decay would allow the core to survive the transient without exceeded failure limits.

In the first LOFA without GEM simulation, a single primary EM pump fails leaving the other three pumps responsible for providing adequate cooling to the core. Results of this transient are summarized in Table 40 and the maximum fuel temperatures are plotted in Figure 18. Each of the cores remained an acceptable margin from their failure limits during this transient. The reactivity feedbacks of the Oxide and Nitride cores provided the strongest response to the transient, decreasing the power approximately 60 MW, while the Metal core experienced the largest increase in fuel temperature relative to its melting temperature. The bump in the maximum Metal fuel temperature at eight seconds can be attributed to a shift from the average driver fuel assemblies to the radial blanket assemblies as the hottest assemblies.

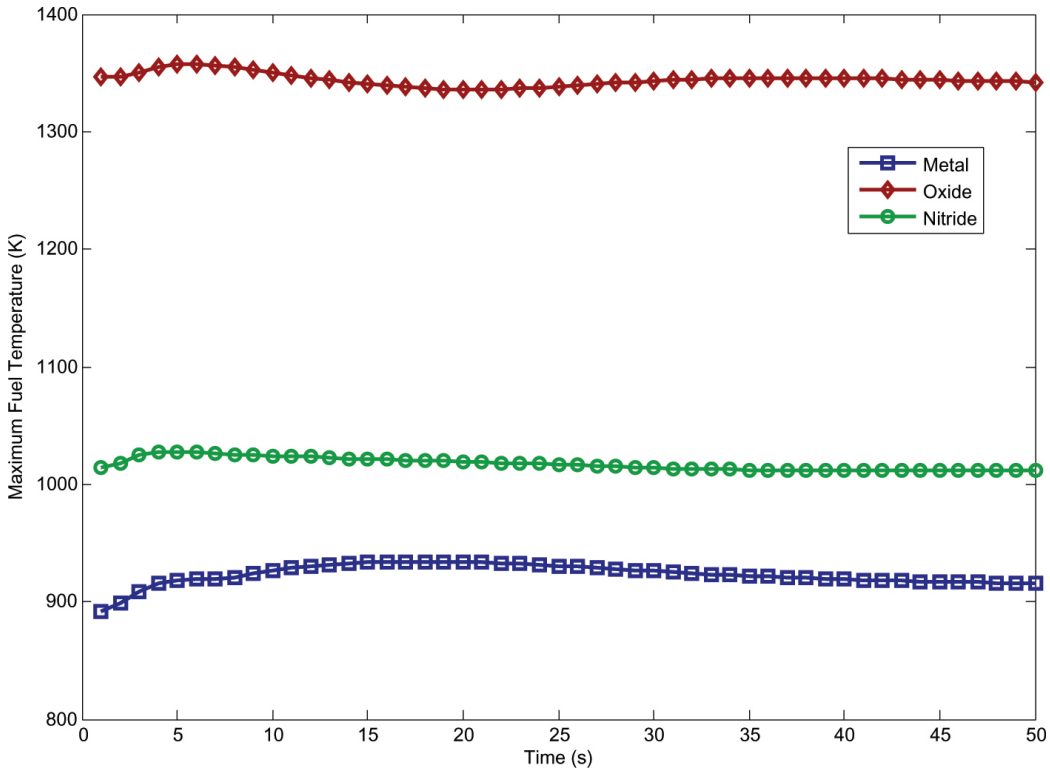

Figure 18: Peak fuel temperatures during single pump LOFA

Table 40: Results of single pump LOFA

	T_{fuel}^{max} (K)	Δ RFT	T_{cool}^{max} (K)	Δ P (MWt)
Metal (BOC)	934	0.093	881	-45
Metal (MOC)	927	0.069	874	-53
Metal (EOC)	932	0.055	872	-34
Oxide (BOC)	1,358	0.007	890	-59
Oxide (MOC)	1,338	0.006	896	-60
Oxide (EOC)	1,323	0.007	902	-57
Nitride (BOC)	1,028	0.007	861	-60
Nitride (MOC)	1,020	0.006	871	-60
Nitride (EOC)	1,014	0.007	880	-55

The scenario of a single primary loop pump seizing due to debris blocking the coolant flow channel was also simulated to determine if a more rapid flow decay would change the results. Because the mass flow rate already decays very quickly, the results of a single pump seizure were not much different from the standard single pump LOFA. The magnitudes of the change in power and temperatures for a single

pump seizure accident were slightly larger than if the pump did not seize, though not enough to change the outcome of this transient significantly. Multiple pump seizures were not simulated because a scenario in which multiple pumps were simultaneously and completely blocked could not be contemplated. Any other scenario with all pump seizing at similar times would result in a similar progression to the four pump LOFA due to the rapid decay in coolant mass flow rate in that transient.

Table 41: Results of single pump seizure

	T_{fuel}^{max} (K)	Δ RFT	T_{cool}^{max} (K)	Δ P (MWt)
Metal (BOC)	935	0.095	882	-46
Metal (MOC)	928	0.070	875	-54
Metal (EOC)	933	0.060	873	-35
Oxide (BOC)	1,361	0.009	890	-60
Oxide (MOC)	1,340	0.007	896	-61
Oxide (EOC)	1,325	0.008	902	-58
Nitride (BOC)	1,031	0.008	861	-61
Nitride (MOC)	1,024	0.008	871	-61
Nitride (EOC)	1,018	0.009	881	-56

A two pump LOFA without GEM will quickly leave the core with half of its nominal coolant mass flow rate. The Oxide and Nitride cores did not experience significant increases in fuel temperatures. The Metal core did, however, experience a significant fuel temperature increase relative to its melting temperature. Like the one pump LOFA, this transient illustrates the difference between the reactivity feedbacks of the Oxide and Nitride cores relative to the Metal core, with smaller changes in power occurring in the Metal core. In fact, the reactivity feedbacks in the Oxide core are so strong that fourteen seconds after the start of the transient, the maximum fuel temperature is lower than the steady-state maximum temperature. In the Nitride core this happens after sixty seconds.

The results of the two pump LOFA are summarized in Table 42 and the maximum fuel temperatures are plotted in Figure 19. Figure 20 illustrates the change in power over the progression of the transient in the Metal, Oxide and Nitride cores. Because

the coolant exiting the four EM pumps mixes before entering the lower plenum, the results of a two pump LOFA are the same for any combination of two failing pumps. This is also true for a three pump LOFA.

Table 42: Results of two pump LOFA

	T_{fuel}^{max} (K)	Δ RFT	T_{cool}^{max} (K)	Δ P (MWt)
Metal (BOC)	1,028	0.297	964	-138
Metal (MOC)	1,013	0.258	950	-156
Metal (EOC)	1,023	0.262	958	-108
Oxide (BOC)	1,380	0.020	969	-165
Oxide (MOC)	1,358	0.018	978	-169
Oxide (EOC)	1,344	0.019	987	-162
Nitride (BOC)	1,058	0.022	931	-174
Nitride (MOC)	1,050	0.021	944	-173
Nitride (EOC)	1,045	0.022	959	-162

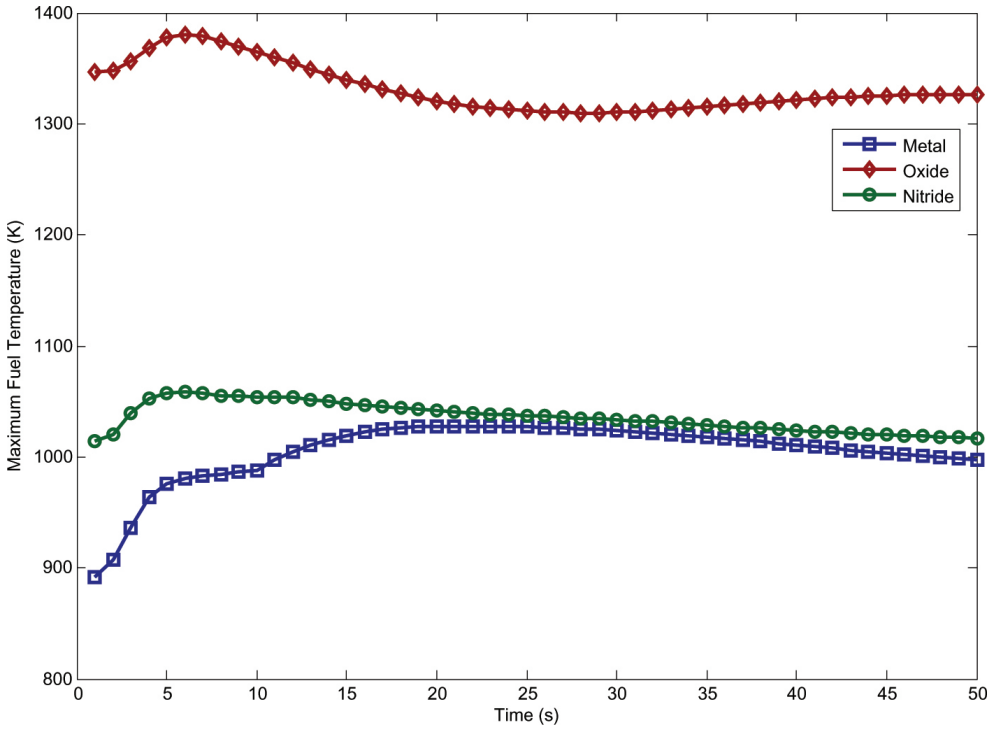

Figure 19: Peak fuel temperatures during two pump LOFA

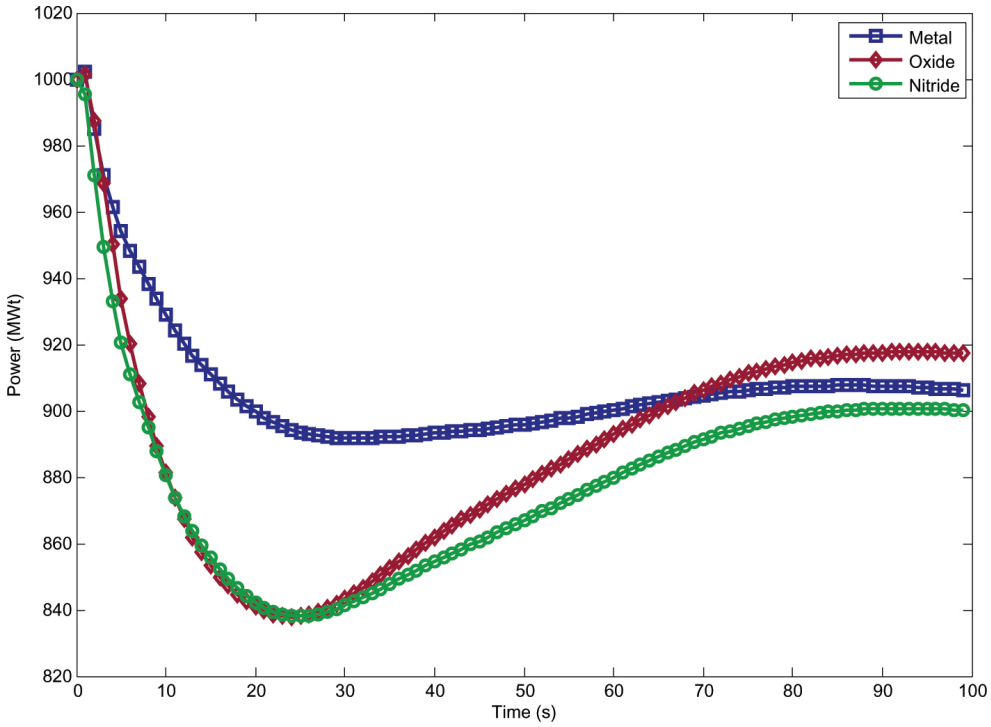

Figure 20: Power during two pump LOFA

In the three pump LOFA, the Metal core approaches its fuel melting temperature, with temperatures exceeding 1,200 K. The maximum fuel temperature in the Metal core is achieved 31 seconds into the transient. Temperatures in the Oxide and Nitride cores are similar but much lower relative to their fuel melting temperatures. All three cores are successful in staying below their failure limits during this transient but the Metal core is no longer an acceptable margin from those limits. Safe operation of the Metal S-PRISM core requires that no less than two primary loop pumps are functional at any one time.

Table 43: Results of three pump LOFA

	T_{fuel}^{max} (K)	Δ RFT	T_{cool}^{max} (K)	Δ P (MWt)
Metal (BOC)	1,236	0.752	1,129	-374
Metal (MOC)	1,200	0.670	1,097	-399
Metal (EOC)	1,254	0.783	1,147	-323
Oxide (BOC)	1,440	0.056	1,051	-393
Oxide (MOC)	1,411	0.049	1,058	-398
Oxide (EOC)	1,402	0.053	1,071	-387
Nitride (BOC)	1,139	0.062	1,063	-422
Nitride (MOC)	1,151	0.071	1,081	-421
Nitride (EOC)	1,183	0.090	1,108	-405

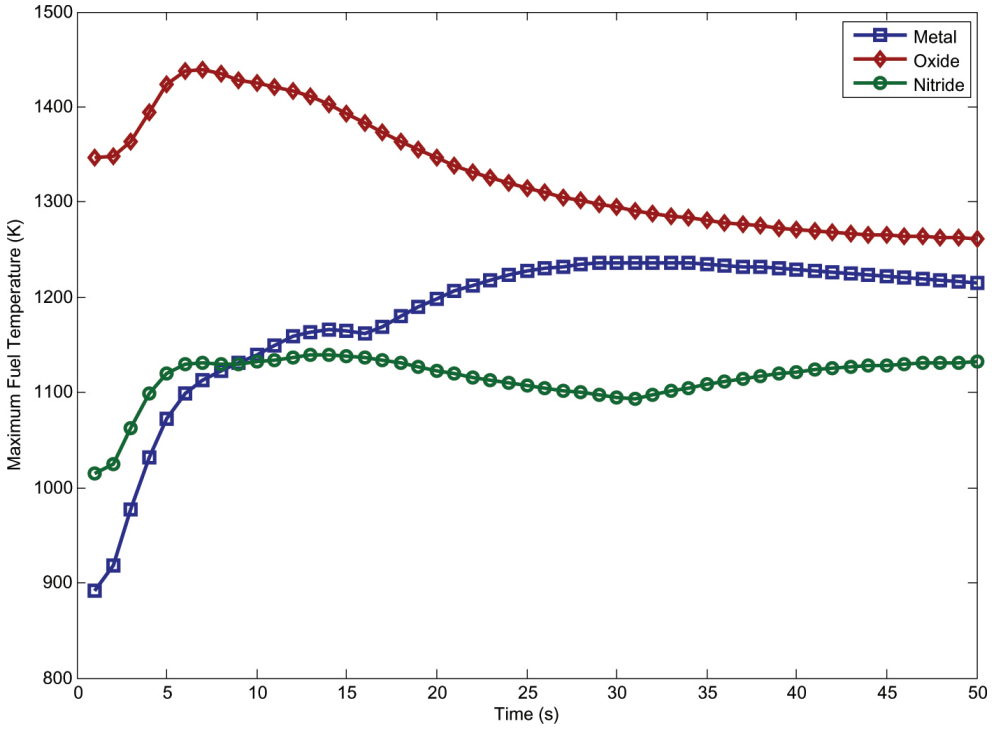

Figure 21: Peak fuel temperatures during three pump LOFA

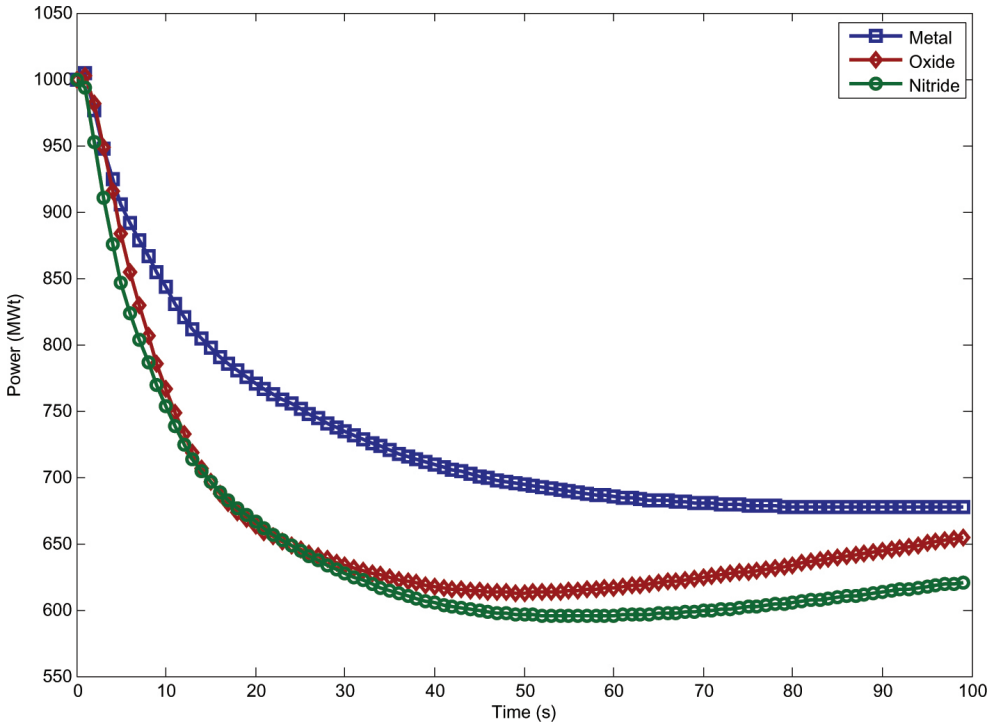

Figure 22: Power during three pump LOFA

The ultimate Loss of Flow Accident is a loss of pumping power to all four primary loop coolant pumps leading to a rapid drop in coolant mass flow rate. Reactivity feedbacks must be strong enough to decrease the core power to decay heat levels so that natural circulation alone can cool the core. As with previous transients, the Oxide and Nitride core performance was vastly superior to the Metal core performance. In the Oxide and Nitride cores, the margin to fuel melting only decreased by 25%.

Table 44: Results of complete LOFA

	T_{fuel}^{max} (K)	Δ RFT	T_{cool}^{max} (K)	Δ P (MWt)
Metal (BOC)	> 1,350	> 1.000	> 923	-284
Metal (MOC)	> 1,350	> 1.000	> 901	-350
Metal (EOC)	> 1,350	> 1.000	> 900	-191
Oxide (BOC)	1,769	0.252	1,278	-641
Oxide (MOC)	1,708	0.224	1,379	-609
Oxide (EOC)	1,715	0.236	1,382	-595
Nitride (BOC)	1,539	0.260	1,475	-685
Nitride (MOC)	1,521	0.253	1,453	-684
Nitride (EOC)	1,531	0.261	1,466	-667

Table 45: Failure modes of Metal core during complete LOFA

	Time to Failure (s)	Failure Mode	Which Assembly
Metal (BOC)	5.7	Fuel Melting	Average Driver Fuel
Metal (MOC)	5.9	Fuel Melting	Average Driver Fuel
Metal (EOC)	5.1	Fuel Melting	Hot Driver Fuel

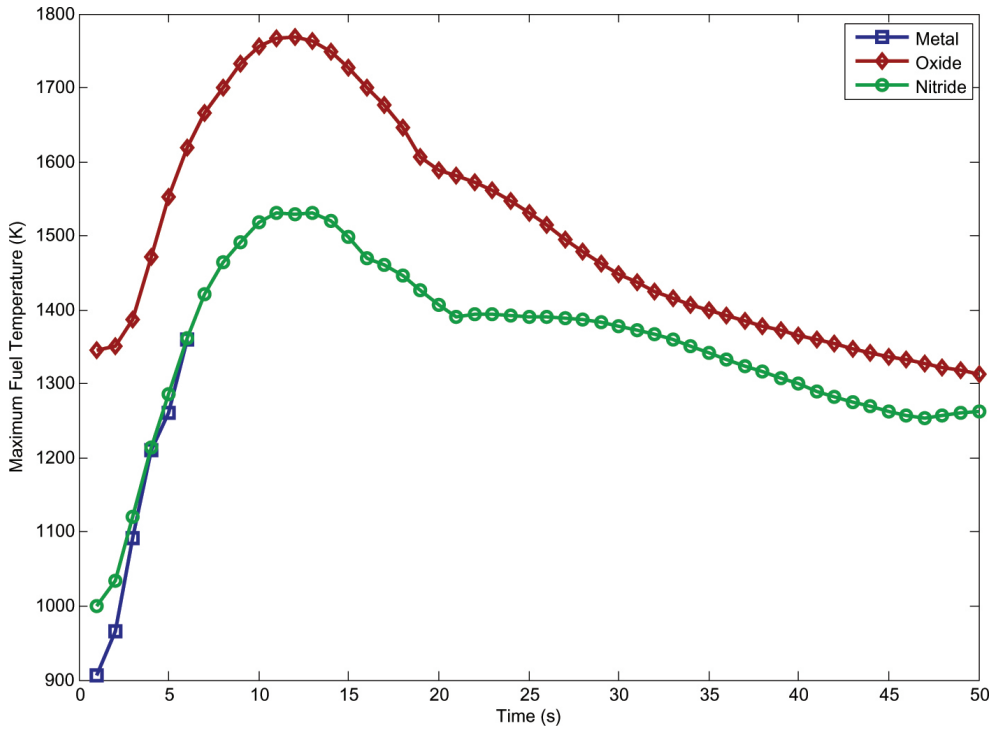

Figure 23: Peak fuel temperatures during complete LOFA. Metal simulation ends when fuel melting occurs.

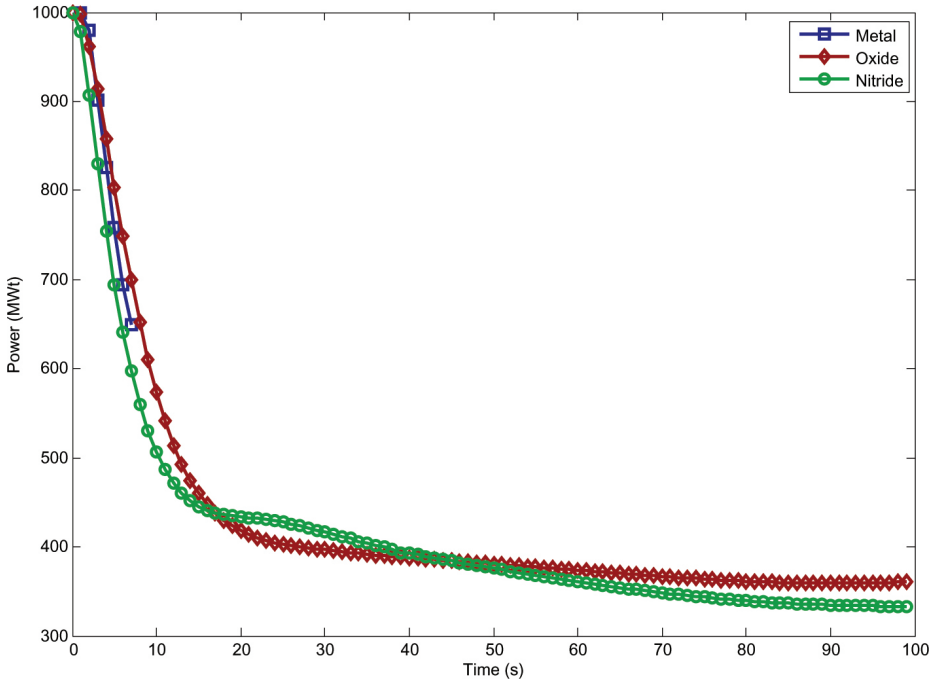

Figure 24: Power during complete LOFA. Metal simulation ends when fuel melting occurs.

Because the Metal core's reactivity feedbacks are not strong enough to curtail the temperature increases in the reactor, the Metal core experiences fuel melting less than six seconds after the start of the transient. The failure mode of the Metal core is summarized in Table 45. To determine if a slower mass flow rate decay would provide the necessary margins to core safety for the Metal core, the four pump LOFA was simulated using the six second halving time flow coast down scheme. Despite providing an addition 35-40 seconds before fuel melting, the Metal core still experiences fuel melting during this accident. The results of this transient are given in Tables 46 and 47.

Table 46: Results of four pump LOFA with slower flow rate decay

	T_{fuel}^{max} (K)	Δ RFT	T_{cool}^{max} (K)	Δ P (MWt)
Metal (BOC)	$>$ 1,350	$>$ 1.000	$>$ 999	-448
Metal (MOC)	$>$ 1,350	$>$ 1.000	$>$ 998	-549
Metal (EOC)	$>$ 1,350	$>$ 1.000	$>$ 1,000	-346

Table 47: Failure mode of Metal core during complete LOFA

	Time to Failure (s)	Failure Mode	Which Assembly
Metal (BOC)	40	Fuel Melting	Radial Blanket
Metal (MOC)	47	Fuel Melting	Radial Blanket
Metal (EOC)	36	Fuel Melting	Average Driver Fuel

There is not a significant difference in the performance of the Oxide and Nitride cores during the Loss of Flow Accidents. Both cores maintained acceptable margins to fuel melting in all cases due to strong negative reactivity insertions from the feedbacks. The Metal core however was only able to maintain an acceptable margin to fuel melting during the one and two pump LOFA transients. The failure of more than two primary loop EM pumps will take the Metal core close to or beyond its fuel melting temperature.

6.2.3 Loss of Heat Sink Accidents in the Intermediate Loop

Loss of Heat Sink Accidents (LOHSA) were simulated in a similar way as Loss of Flow Accidents except coolant mass flow was lost in the intermediate sodium loop instead of the primary sodium loop. In this anticipated transient without scram, diminished coolant flow in the intermediate loop led to inadequate heat removal across the heat exchanger, elevating fuel and coolant temperatures in the core. These elevated temperatures triggered a negative reactivity feedback, thereby decreasing core power. The different S-PRISM cores needed to have strong enough reactivity feedbacks to curtail the fission power enough so that core limits are not exceeded.

The first LOHSA scenario was a failure of the sodium pumps in one of the two intermediate coolant loops, requiring the other heat exchanger to remove the majority of heat production from the primary loop. The mass flow rate of an intermediate loop with failed coolant pumps is illustrated in Figure 16. Core power and reactivity are illustrated in Figures 25 and 26 and maximum temperatures are given in Figure 27.

The ten second delay before the effects of the transient had a significant impact is

a result of the delay before the hotter inlet sodium reached the core. Core reactivity decreased once inlet sodium temperatures began to rise. The Metal, Oxide and Nitride cores were all able to generate adequate negative reactivity responses from the increased inlet coolant temperatures and consequently all three cores maintained acceptable margins to fuel melting. The Metal core experienced the largest fuel temperature increases relative to its melting temperature at around 7%.

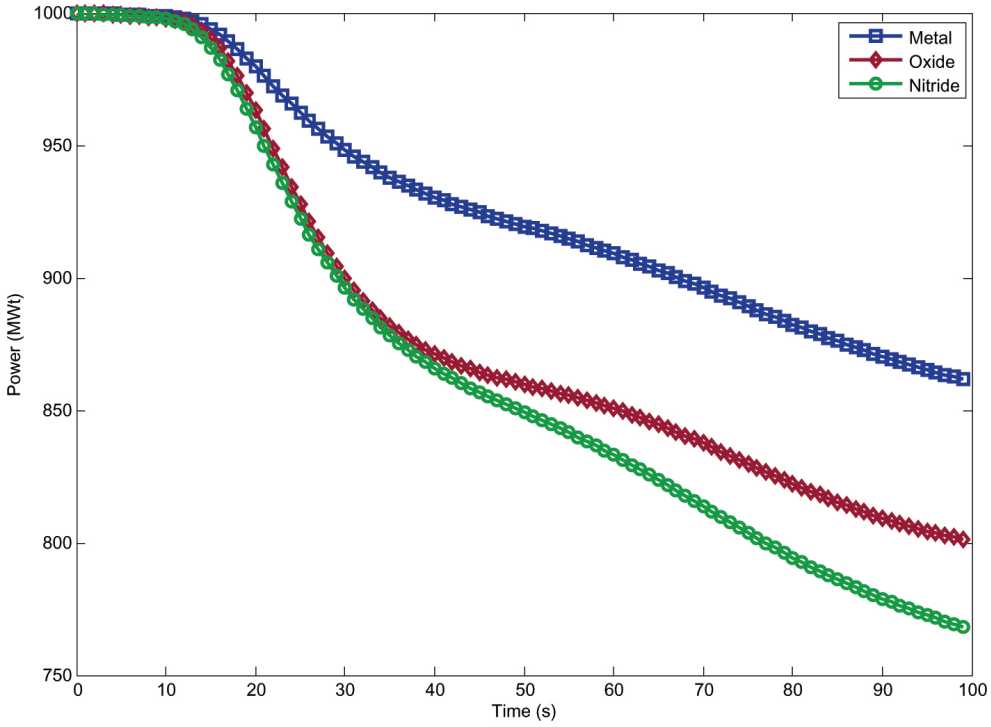

Figure 25: Power during single side LOHSA

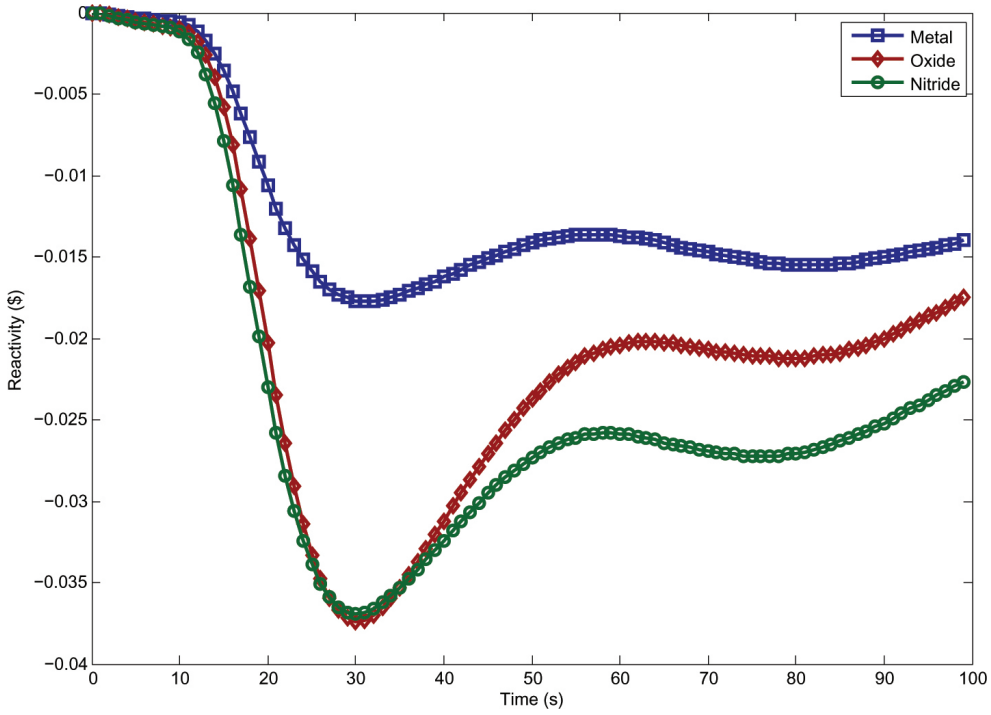

Figure 26: Reactivity during single side LOHSA

Table 48: Results of single side LOHSA

	T_{fuel}^{max} (K)	Δ RFT	T_{cool}^{max} (K)
Metal (BOC)	923	0.070	872
Metal (MOC)	923	0.061	863
Metal (EOC)	943	0.082	874
Oxide (BOC)	1,347	0.000	872
Oxide (MOC)	1,328	0.000	875
Oxide (EOC)	1,312	0.000	880
Nitride (BOC)	1,021	0.003	849
Nitride (MOC)	1,014	0.003	855
Nitride (EOC)	1,010	0.005	862

At thirty seconds, the average fuel temperatures in the core began decreasing, triggering a positive reactivity insertion, but not enough to reestablish criticality at that time. Over the remainder of the transient, competing effects of the fuel and coolant reactivity feedbacks combined with the time required for coolant to travel from the heat exchanger to the inlet plenum led to the cyclical reactivity versus time. Eventually criticality was restored in each core and the reactor established a new

steady-state. Reestablishment of criticality occurred at 460, 360 and 310 seconds in the Metal, Oxide and Nitride cores, respectively. Core power after 1,000 seconds in the Metal, Oxide and Nitride cores was at 770, 766 and 716 MW, respectively, while inlet and outlet coolant temperatures rose to an average of 706 and 817 K for all three cores. Maximum values obtained during this transient are given in Table 48.

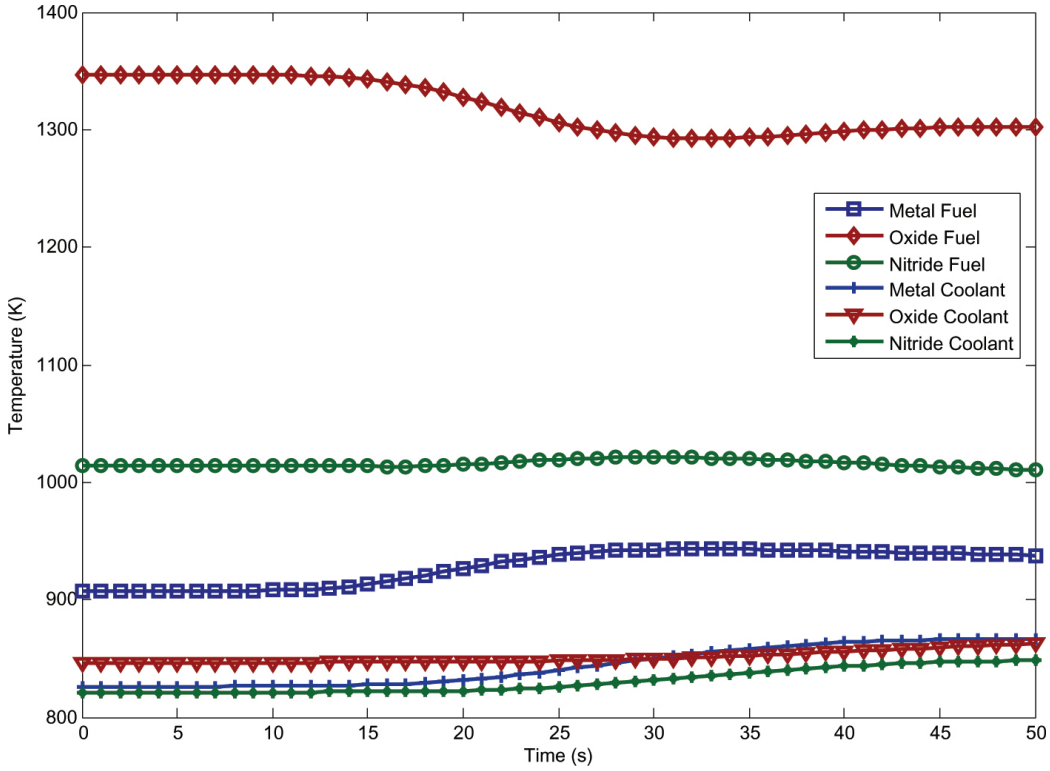

Figure 27: Maximum fuel and coolant temperatures during single side LOHSA

The next Loss of Heat Sink Accident was a loss of coolant mass flow in one of the two intermediate coolant loops but due to debris in the coolant pipes, the mass flow suddenly seized completely. This transient was designed to test whether a more rapid flow decay would lead to significantly different results than the previous transient. In the previous transient natural circulation in the failed intermediate loop provided added heat removal that was not available in this transient. Because the drop in mass flow in the intermediate loop was nearly instantaneous, the decrease in primary loop cooling was much quicker leading to higher inlet temperatures.

The lack of natural circulation in the failed intermediate loop meant the primary loop experienced less efficient heat removal leading to increased coolant inlet temperatures in the single side seizure LOHSA. Maximum coolant temperatures in the Metal, Oxide and Nitride cores were between 14 and 30 K higher than in the previous non-seizure LOHSA. Maximum fuel temperatures also increased although not as much as for the coolant. Larger temperature increases than in the previous transient led to a much stronger negative reactivity feedback during the ten to thirty second period and as a result power levels during this transient were lower than in the non-seizure LOHSA.

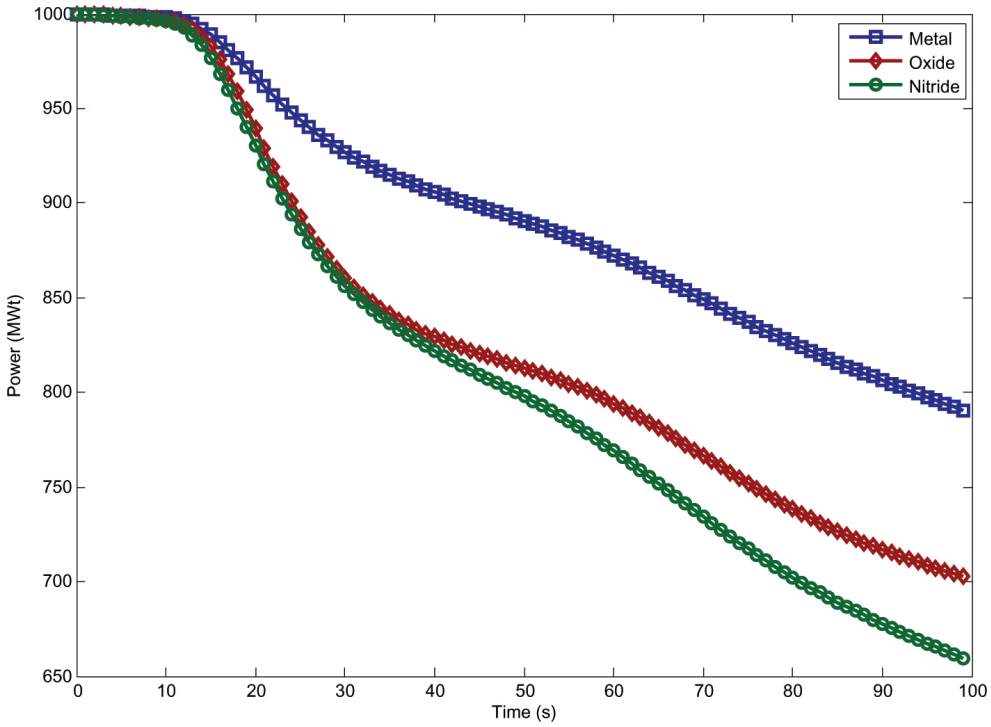

Figure 28: Power during single side seizure LOHSA

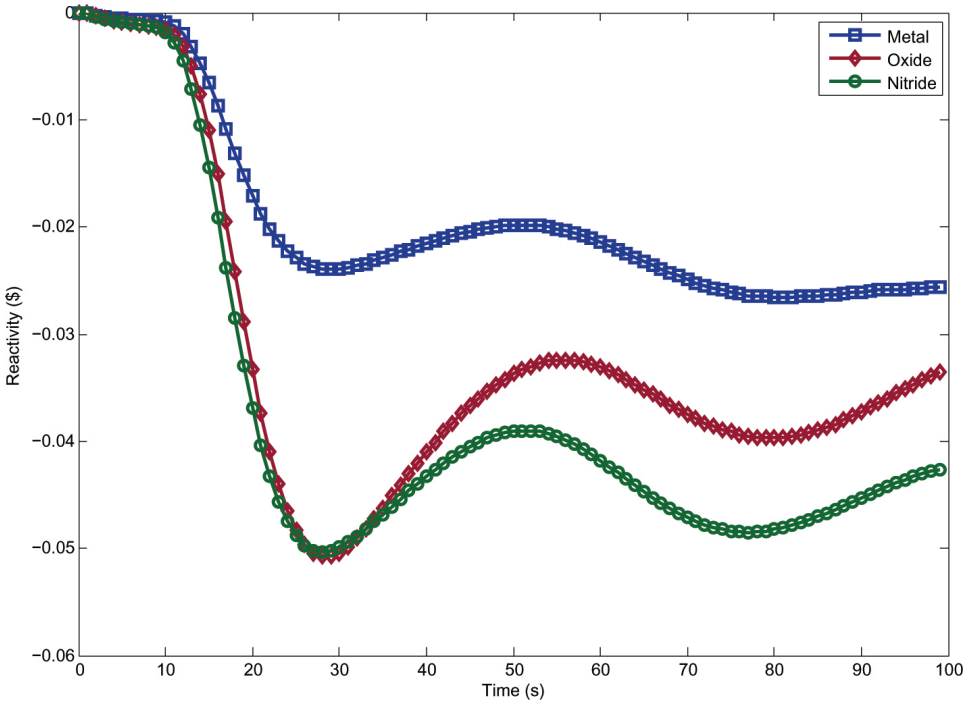

Figure 29: Reactivity during single side seizure LOHSA

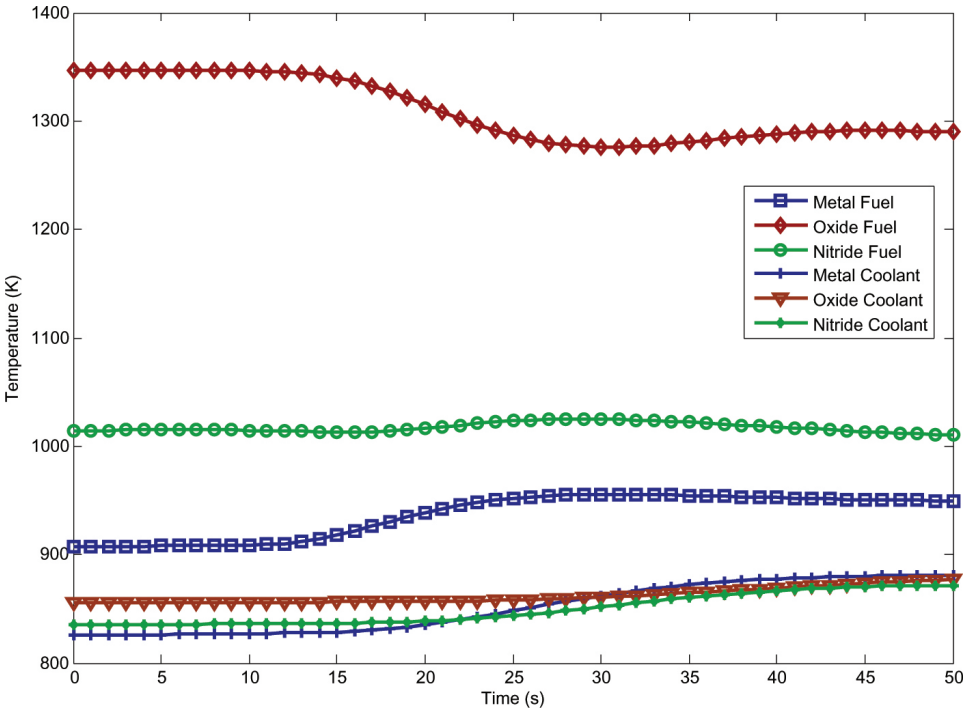

Figure 30: Maximum fuel and coolant temperatures during single side seizure LOHSA

Due to the stronger reactivity feedback, after 1,000 seconds power in the Metal, Oxide and Nitride cores was at 600, 594 and 537 MW, respectively, each approximately 70 MW lower than the previous transient. Inlet temperatures at 1,000 seconds rose to 755 K and outlet temperatures to 839 K, compared to 706 and 817 K in the non-seizure LOHSA. Despite the lower power throughout this transient, the lower fuel and coolant temperatures resulted from increased heat removal in the non-seizure single side LOHSA resulting in a more desirable core state in the non-seizure single side LOHSA. However, strong enough reactivity feedbacks were generated that all cores in both accidents maintained acceptable margins to fuel melting.

Table 49: Results of single side seizure LOHSA

	T_{fuel}^{max} (K)	Δ RFT	T_{cool}^{max} (K)
Metal (BOC)	937	0.099	896
Metal (MOC)	936	0.083	884
Metal (EOC)	966	0.133	904
Oxide (BOC)	1,347	0.000	888
Oxide (MOC)	1,328	0.000	889
Oxide (EOC)	1,312	0.000	895
Nitride (BOC)	1,025	0.005	866
Nitride (MOC)	1,018	0.005	870
Nitride (EOC)	1,015	0.007	878

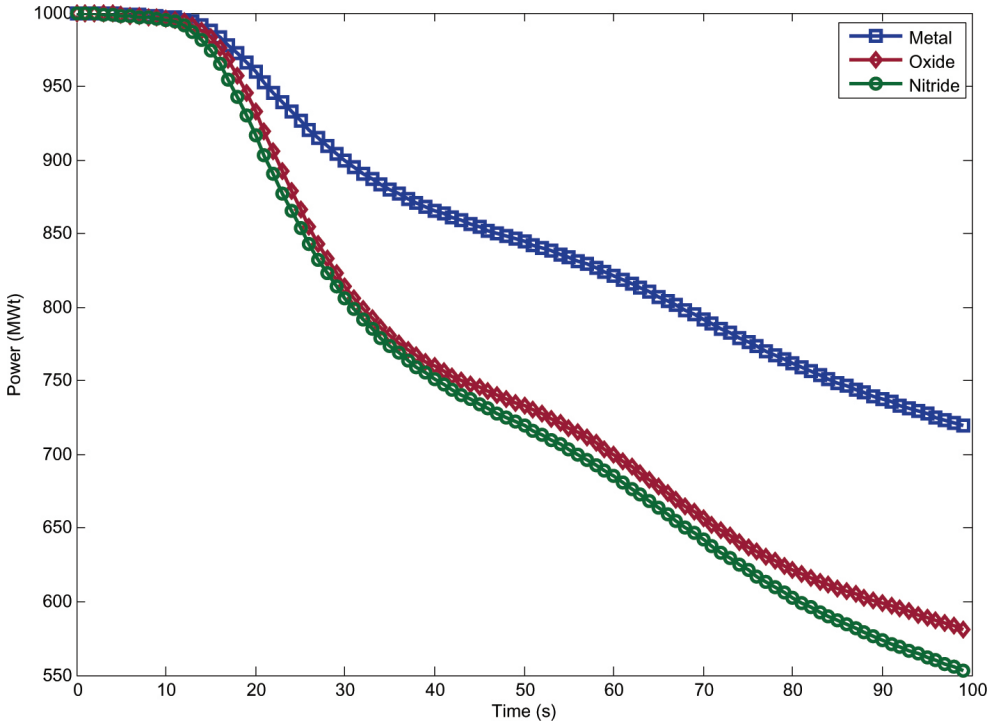

Figure 31: Power during complete LOHSA

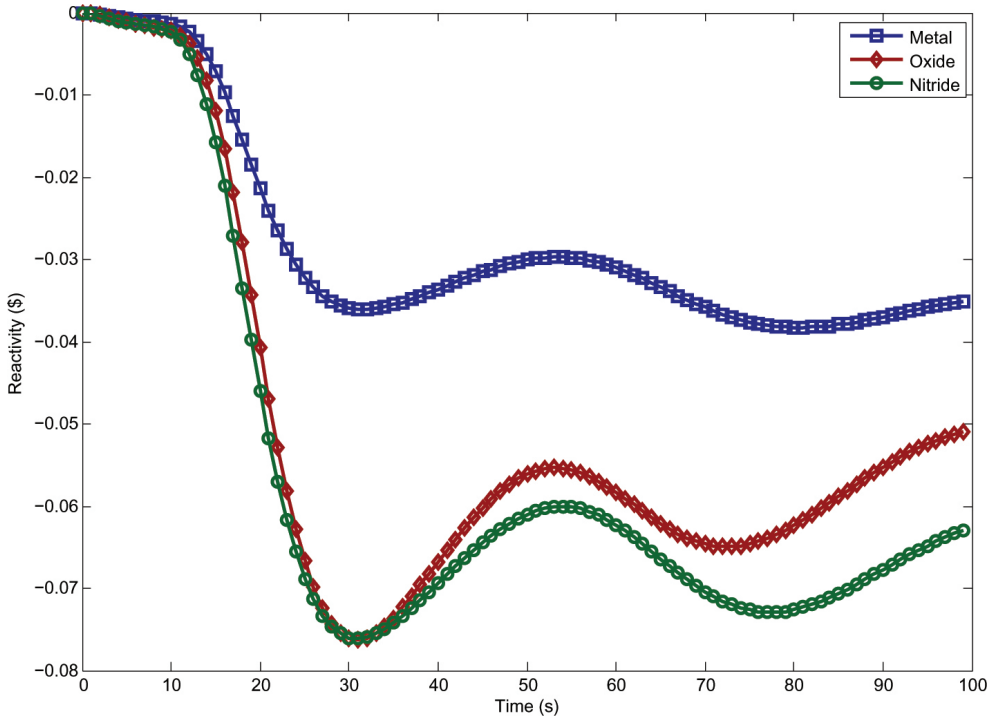

Figure 32: Reactivity during complete LOHSA

The final intermediate loop Loss of Heat Sink Accident was a failure of the coolant pumps in both intermediate sodium loops. Following pump failure, coolant mass flow coasted down at the rate shown in Figure 16 in both intermediate loops and heat removal across both intermediate heat exchangers was significantly decreased. Inlet temperatures increased significantly more than in the previous Loss of Heat Sink Accidents leading to a stronger negative reactivity feedback response.

The progression of the complete Loss of Heat Sink Accident was similar to the two previous Loss of Heat Sink Accidents, but slightly larger in magnitude. Reactivity feedbacks eventually decreased core power to 50% where natural circulation in the intermediate coolant loops was sufficient to remove all heat generation. After 1,000 seconds, natural circulation in the intermediate coolant loops had established a mass flow rate at 20% of nominal. Peak temperatures in this transient were slightly higher than the two previous LOHSA transients but due to the stronger reactivity drop at the start of the transient, all cores were again able to maintain a safe margin to fuel melting.

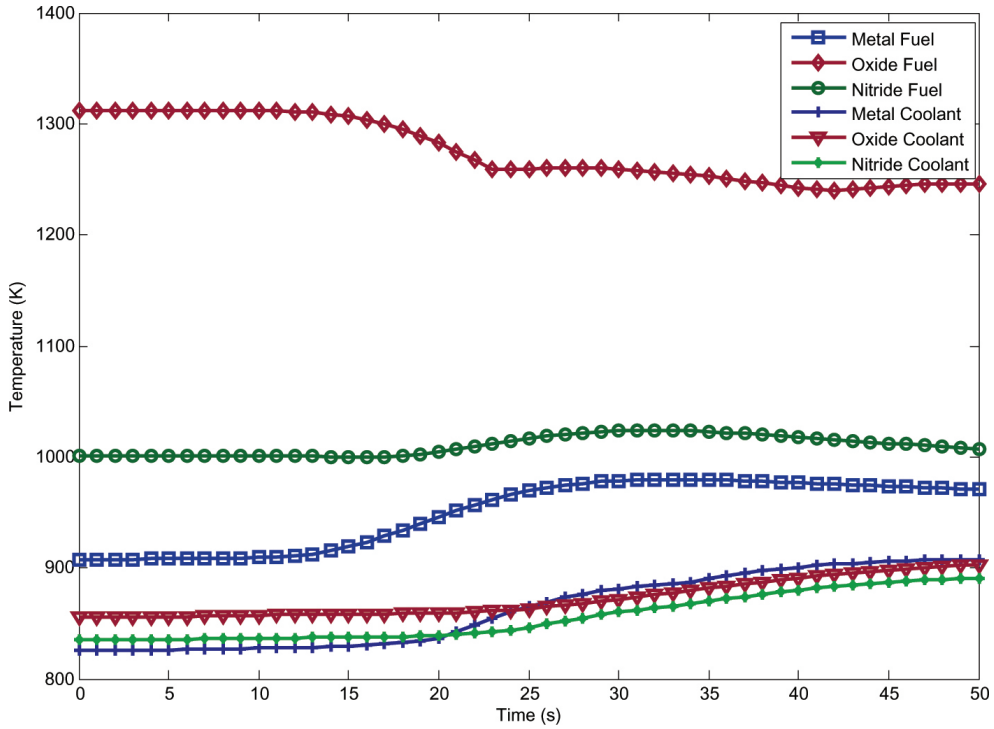

Figure 33: Maximum fuel and coolant temperatures during complete LOHSA

Table 50: Results of complete LOHSA

	T_{fuel}^{max} (K)	Δ RFT	T_{cool}^{max} (K)
Metal (BOC)	958	0.145	921
Metal (MOC)	953	0.126	907
Metal (EOC)	990	0.188	933
Oxide (BOC)	1,347	0.000	915
Oxide (MOC)	1,328	0.000	914
Oxide (EOC)	1,312	0.000	923
Nitride (BOC)	1,033	0.009	888
Nitride (MOC)	1,025	0.009	890
Nitride (EOC)	1,024	0.012	899

Because Loss of Heat Sink Accidents were slower to progress than Loss of Flow Accidents, each core had enough time for reactivity feedbacks to decrease core power to manageable levels. All S-PRISM cores can tolerate the failure of any number of coolant pumps in the intermediate sodium loop or even a complete blockage of one of the loops. The corresponding decrease in power was strong enough that melting

temperatures were not approached in any core.

6.2.4 Loss of Heat Sink Accidents in the Secondary Loop

Loss of Heat Sink Accidents affecting one or both of the secondary water loops were simulated as a loss of water mass flow leading to a reduction in the steam generator's ability to decrease temperatures in the intermediate sodium loop. Because the secondary loop was not modeled as a complete loop, the six second halving time was used to approximate the mass flow decay rate. As with the intermediate loop Loss of Heat Sink Accidents, Loss of Heat Sink Accidents of the secondary loop (LOHSA-SL) led to increased coolant inlet temperatures, under-cooling of the fuel and a negative reactivity feedback. In this anticipated transient without scram, the magnitude of the reactivity feedback must be strong enough to decrease core power to the point that a less functional steam generator can adequately cool the reactor.

The first LOHSA-SL transient simulation was a loss of flow in one of the two water loops with the other secondary loop remaining unchanged. Because of the added delay for intermediate loop sodium to travel from the steam generator to the heat exchanger, the delay before the transient affected a reactivity change in the core was larger than in the LOHSA transients. The results of this transient are summarized in Table 51 and the power of the three S-PRISM cores is illustrated in Figure 34. Coolant and fuel temperatures during the transient are illustrated in Figure 35.

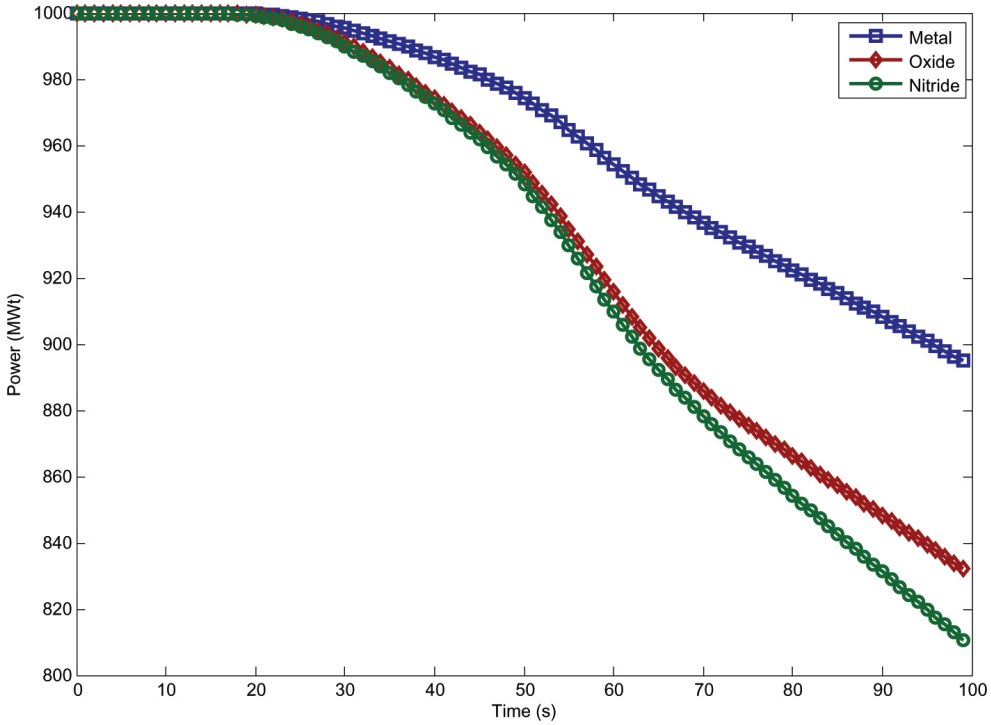

Figure 34: Power during single side LOHSA-SL

The gradual coast down of the water in the secondary loop combined with the delay before the primary loop experienced temperature changes led to a more gradual decrease in core temperatures than in the LOHSA transients. Because changes were slower to occur, maximum temperatures did not increase as much in this transient and consequently, none of the three S-PRISM cores experienced significant temperature increases. The EOC Metal core experienced the largest temperature increases with an 8% reduction in the margin to fuel melting and an average peak coolant temperature rise of 37 K. Average peak coolant temperatures rose in the Oxide and Nitride cores by 21 and 26 K, respectively.

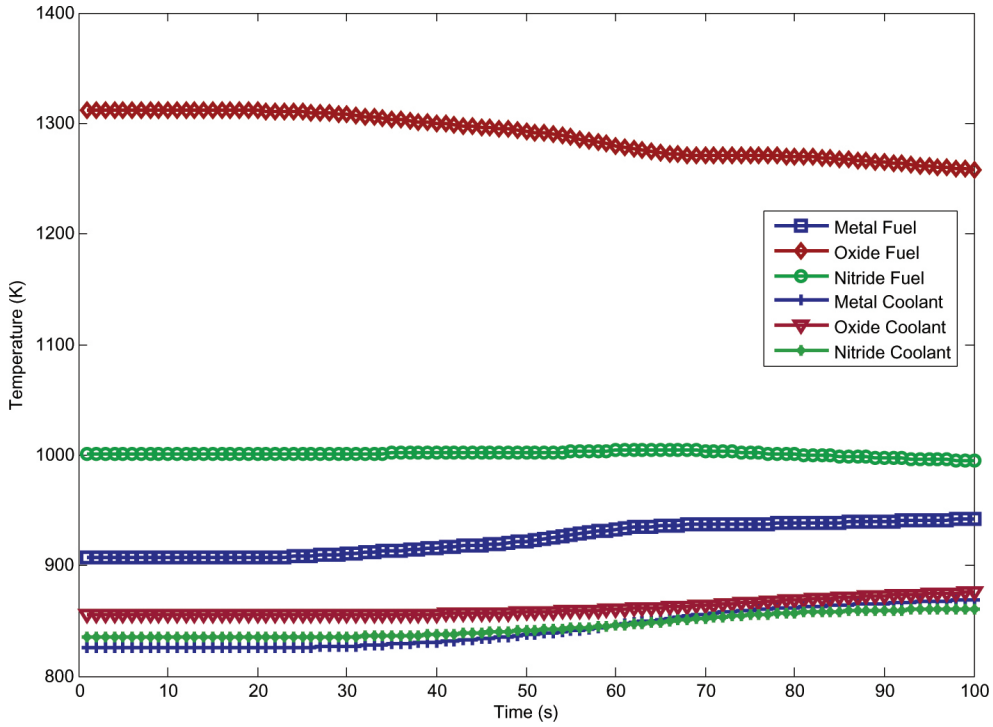

Figure 35: Maximum fuel and coolant temperatures during single side LOHSA-SL

Table 51: Results of single side LOHSA-SL

	T_{fuel}^{max} (K)	Δ RFT	T_{cool}^{max} (K)
Metal (BOC)	919	0.060	871
Metal (MOC)	917	0.047	863
Metal (EOC)	942	0.080	869
Oxide (BOC)	1,346	0.000	868
Oxide (MOC)	1,328	0.000	871
Oxide (EOC)	1,311	0.000	876
Nitride (BOC)	1,016	0.001	848
Nitride (MOC)	1,009	0.001	854
Nitride (EOC)	1,005	0.002	861

A LOHSA-SL affecting both secondary water loops was also simulated. As with the single side LOHSA-SL, the core needed to provide an adequate reactivity feedback response to the diminished heat removal across the steam generator. With both steam generators performing at a diminished capacity, the reactivity response of the core was even more important. The six second halving time decay scheme was again used

to simulate the mass flow rate of the two secondary water loops after pump failure. The results of this transient are summarized in Table 52 and the power of the three S-PRISM cores is illustrated in Figure 36. Coolant and fuel temperatures during the transient are illustrated in Figure 37.

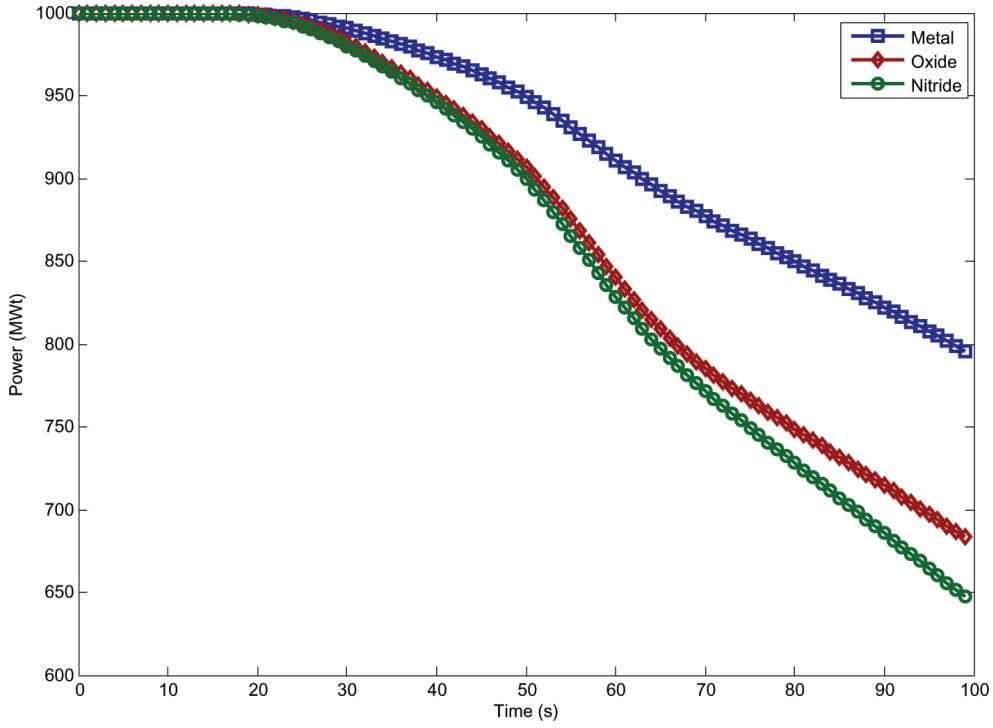

Figure 36: Power during complete LOHSA-SL

The strong reactivity feedback in the Oxide and Nitride cores prevented significant fuel temperature increases during the Complete LOHSA-SL while the margin to fuel melting in the Metal core decreases by at most 17%. Peak temperature in the coolant only increased to 914 K in the Metal core and in the Oxide and Nitride cores that number dropped below 900 K. The initial negative reactivity insertion occurred gradually such that after one minute the power level in the Oxide and Nitride cores had dropped to around 800 MW and in the Metal core the power level was around 900 MW and all cores maintained strong negative reactivities. As the transient continued, power in all three cores continued to drop off steadily and criticality was never

reestablished. Eventually the failed secondary loop was only responsible for removing decay heat production.

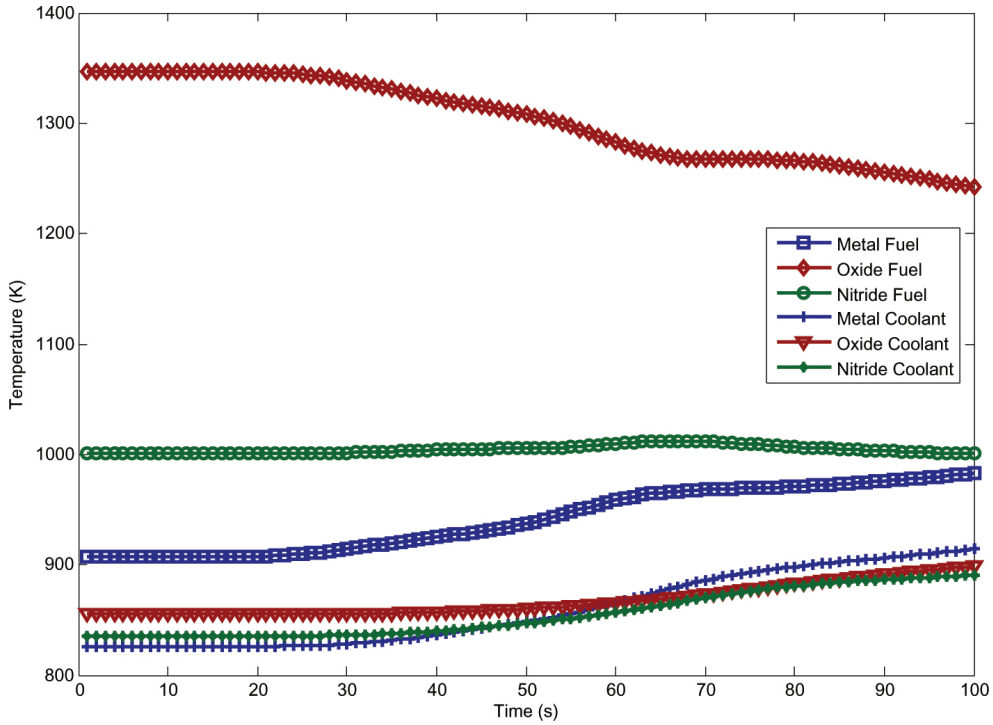

Figure 37: Maximum fuel and coolant temperatures during complete LOHSA-SL

Loss of Heat Sink Accidents affecting the secondary loop did not present the possibility of fuel melting. Like the previous LOHSA transients, large negative reactivity insertions occurring before core temperatures had a chance to significantly increase prevented fuel melting margins from decreasing substantially. While all cores maintain sub-melting temperatures, the Oxide and Nitride cores maintained larger limits to fuel melting than the Metal core. Unless natural circulation in both secondary loops is somehow prevented, all cores were capable of experiencing LOHSA-SL transients without serious risk to core safety.

6.2.5 Loss of Power Accidents

The beyond design basis event Loss of Power Accident (LOPA) was simulated as a complete loss of power to all sodium EM pumps to determine if natural circulation in

Table 52: Results of complete LOHSA-SL

	T_{fuel}^{max} (K)	Δ RFT	T_{cool}^{max} (K)
Metal (BOC)	954	0.136	909
Metal (MOC)	946	0.110	898
Metal (EOC)	983	0.171	914
Oxide (BOC)	1,346	0.000	891
Oxide (MOC)	1,328	0.000	893
Oxide (EOC)	1,311	0.000	899
Nitride (BOC)	1,021	0.003	879
Nitride (MOC)	1,014	0.003	883
Nitride (EOC)	1,012	0.006	891

the primary and intermediate coolant loops was sufficient to cool the reactor. Because the natural circulation tests covered loss of primary and intermediate pumping power with a simultaneous large negative reactivity insertion, simulating the Loss of Power Accident with the corresponding GEM reactivity insertion was considered trivial. Therefore, the Loss of Power Accident was simulated with no external reactivity assistance from GEM or control rod assemblies. The conservative flow coast down scheme was used for both sodium loops. In the event that this resulted in fuel melting, the six second halving time decay scheme was used to determine if a slower mass flow rate coast down in the primary loop would allow the reactor to successfully endure this transient.

During the first several seconds of this transient, before the inlet sodium temperature was affected by the less efficient heat exchanger, this transient was very similar to the Loss of Flow Accident without GEM. Once the effects of the intermediate loop reach the reactor core, the LOPA results deviate from the LOFA without GEM results. In the LOFA without GEM transient the Metal core experienced fuel melting after 5 seconds and the results were no different for this transient. The failure mode of the Metal core at different points in the fuel cycle is given in Table 54. This calculation was then repeated with the six second halving time decay scheme and the results were again similar to the Loss of Flow without GEM. For the LOPA without

GEM simulation, using the less conservative flow coast down scheme allowed time for the effects of the intermediate loop failure to percolate to the primary loop, leading to a slightly more severe accident than if the intermediate loops had not failed.

Table 53: Results of LOPA

	T_{fuel}^{max} (K)	Δ RFT	T_{cool}^{max} (K)
Metal (BOC)	$>$ 1,350	$>$ 1.000	898
Metal (MOC)	$>$ 1,350	$>$ 1.000	899
Metal (EOC)	$>$ 1,350	$>$ 1.000	893
Oxide (BOC)	1,759	0.246	1,434
Oxide (MOC)	1,725	0.235	1,411
Oxide (EOC)	1,730	0.244	1,413
Nitride (BOC)	1,555	0.267	1,495
Nitride (MOC)	1,539	0.262	1,479
Nitride (EOC)	1,551	0.270	1,492

Table 54: Failure mode of Metal core during LOPA

	Time to Failure (s)	Failure Mode	Which Assembly
Metal (BOC)	5.7	Fuel Melting	Average Driver Fuel
Metal (MOC)	5.9	Fuel Melting	Average Driver Fuel
Metal (EOC)	5.0	Fuel Melting	Hot Driver Fuel

Table 55: Results of LOPA with slower flow rate decay

	T_{fuel}^{max} (K)	Δ RFT	T_{cool}^{max} (K)
Metal (BOC)	$>$ 1,350	$>$ 1.000	1,235
Metal (MOC)	$>$ 1,350	$>$ 1.000	1,273
Metal (EOC)	$>$ 1,350	$>$ 1.000	1,294

For the Oxide and Nitride cores, the decreased flow in the primary loop generates such a large negative reactivity insertion that the effects of the intermediate loop pump failure do not significantly change the results of this transient. Peak fuel temperatures in both cores increased by an average of 13 K more than the LOFA without GEM results. Peak coolant temperatures were an average of 49 K higher due to the decreased cooling from the IHX. The margin to fuel melting in both the Oxide and Nitride cores decreased by only 24 and 27%, respectively, which was acceptable

Table 56: Failure modes during LOPA with slower flow rate decay

	Time to Failure (s)	Failure Mode	Which Assembly
Metal (BOC)	40	Fuel Melting	Radial Blanket
Metal (MOC)	46	Fuel Melting	Radial Blanket
Metal (EOC)	31	Fuel Melting	Average Driver Fuel

for this transient. Both cores experienced the beginning of coolant boiling during the most severe part of the transient but in both cases the sodium vapor fraction remained less than 1% due to the higher than atmospheric pressures.

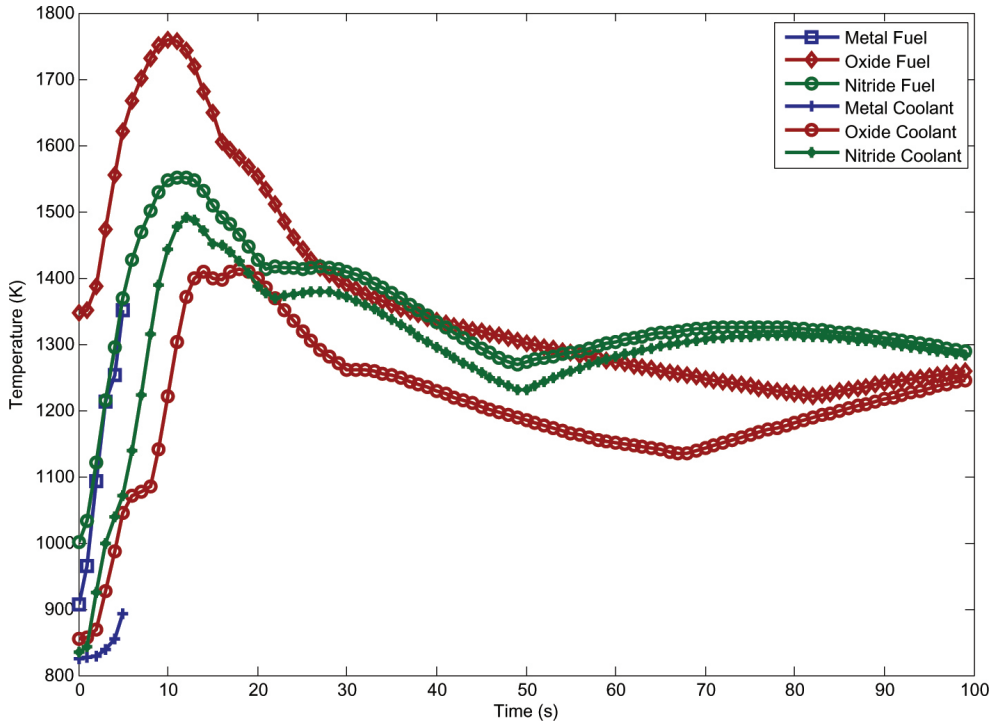

Figure 38: Maximum fuel and coolant temperatures during LOPA. Metal simulation ends when fuel melting occurs.

After temperatures in the core at peaked around ten seconds into the transient, temperatures and reactivities generally decreased until the power production in the core was only due to decay heat. Because natural circulation in the primary and intermediate coolant loops was sufficient to remove the decay heat, the transient progression after ten seconds posed little threat to core safety. Despite the elevated

coolant temperatures at the beginning of the transient, both the Oxide and Nitride cores were successful in enduring a complete loss of power to all sodium EM pumps without experiencing fuel or clad melting.

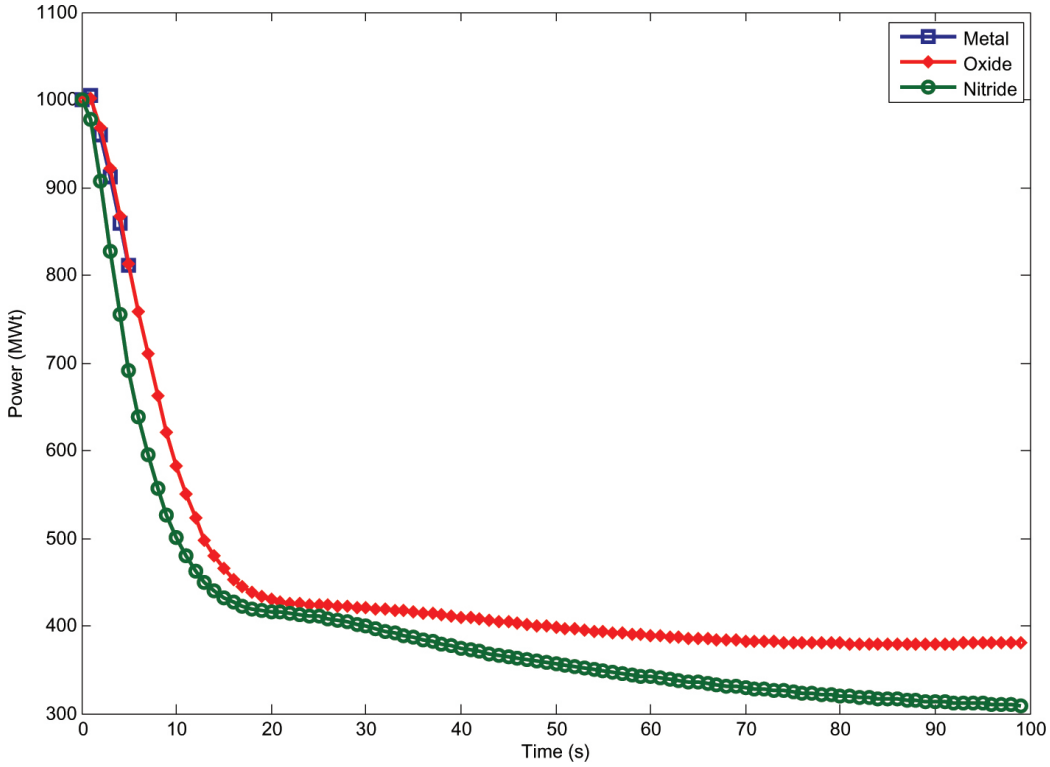

Figure 39: Power during LOPA. Metal simulation ends when fuel melting occurs.

CHAPTER VII

CONCLUSIONS AND RECOMMENDATIONS

7.1 Conclusions

When compared by their thermal properties and reactivity feedbacks, the Metal, Oxide and Nitride S-PRISM cores each have advantages and disadvantages. While the Metal core has the highest thermal conductivity, it has by far the lowest melting temperature. In fact the melting temperature of the cladding is several hundred degrees higher than the Metal fuel's melting temperature. In the Oxide core things are reversed. The Oxide fuel has an extremely low thermal conductivity but with a very high melting temperature, it has a large margin to fuel melting. The Nitride core is the clear winner when it comes to thermal properties with a melting temperature only slightly lower than Oxide's and a thermal conductivity similar to the Metal fuel's.

The Metal S-PRISM fuel experienced much stronger reactivity feedbacks from axial and radial core expansion. Reactivity feedbacks from radial core expansion were 20% higher in the Metal core and for axial core expansion, the Metal core's feedback coefficient was more than 40% greater than in the Oxide and Nitride cores due to a much higher thermal expansion coefficient. But while those reactivity feedbacks were stronger in the Metal core, the Oxide and Nitride cores were stronger in the remaining feedbacks.

The higher content of light atoms in the Oxide and Nitride fuels led to greater neutron moderation and a softer neutron spectra allowing for more neutrons to reach U^{238}'s absorption resonances. Without the moderating atoms that Oxide and Nitride possess, the Metal fuel's Doppler coefficient was not nearly as strong. The

biggest differentiator between the cores was the combined coolant Doppler and thermal expansion feedback effects. During all points of the fuel cycle, the Nitride core experienced a slightly less positive coolant feedback coefficient than the Oxide fuel while the Metal fuel, especially at EOC, had a much stronger positive feedback effect that was the primary contributor to its weaker isothermal reactivity coefficient.

The transient simulations revealed several trends in the different S-PRISM cores. In most of the transients, the Metal core came closer to its melting temperature while the strong reactivity feedbacks of the Oxide and Nitride cores limited the fuel temperature increases. In the Over-power to Scram transient, the Oxide core experienced the largest fuel temperature increases due to its low thermal conductivity, but once 113% of nominal power was reached, its reactivity feedbacks provided the strongest assistance to the control rods in bringing the power level under control. The other anticipated transient with scram, the establishment of natural circulation tests, illustrated the short comings of the Metal core with respect to fuel melting. While the Oxide and Nitride cores could tolerate a slow insertion of the control rods coupled with a trip of the primary and intermediate coolant pumps, the Metal core required a gravity fed four second control rod scram to curtail the temperature increases in the core. Unless a reliable method is found to maintain adequate coolant mass flow levels following a pump failure, the Metal core will be incapable of withstanding a slower control rod insertion.

In the anticipated transients without scram, the three cores performed similarly in the LOFA with GEM, LOHSA and LOHSA-SL transients. The GEM assemblies provided an initiating condition for a strong and rapid enough reactivity insertion that the melting temperatures were never approached. In the LOHSA and LOHSA-SL transients, the effects of the transient were slow enough to affect the reactor core that reactivity feedbacks had a chance to limit core power to safe levels. The distinction between the Metal core and the Oxide and Nitride cores was seen in

the All-rods Withdrawal transient where at BOC and MOC the Metal core came dangerously close to its fuel melting temperature. And in the EOC core, the Metal core did experience fuel melting 88 seconds after the start of the transient. While 88 seconds is plenty of time for reactor operators to take corrective measures against the transient, it is unacceptable that the reactor could not tolerate a \$0.30 reactivity insertion without reestablishing a safe power level.

In the final set of transient, Beyond Design Basis Accidents, the Metal core experienced fuel melting extremely quickly. The Oxide and Nitride cores performed very similarly in the LOFA and LOPA without GEM transients and in both cases, the two cores maintained more than acceptable margins to fuel melting. The Unprotected Transient Over Power Accident is the transient that established the Nitride core's larger margin to fuel melting than the Oxide core. In previous transients the Oxide core's reactivity feedbacks provided such a strong counter to core temperature changes that its melting temperature never became a factor. The three S-PRISM cores were intentionally pushed to their failure limits in the UTOPA and while the Oxide core tolerating a \$0.02/s reactivity insertion for almost a minute before fuel melting occurred was very good, the Nitride core tolerated the accident for more 70 seconds before clad melting occurred and there was still an almost 500 K margin to fuel melting remaining.

There are several methods for improving the safety characteristics of the Metal core and they start with the fuel's thermal properties. The thermal conductivity is already very high and compared to the other two fuel types, it is the Metal fuel's biggest advantage. But the melting temperature is far too low for a core with marginal reactivity feedbacks. More recent fast reactors throughout the world have focused on oxide fuels primarily. Additional focus into metal fuels could lead to increases in the sub-par temperature limits.

Without changing the thermal properties of the Metal fuel, several changes could

be made to the Metal S-PRISM core design presented here that would provide additional safety benefits. A larger core would allow for additional U^{238}, which would strengthen the Doppler reactivity feedback. With a larger core there would be more room for fertile isotopes as well as the possibility of a larger coolant to fuel volume ratio, which would slightly soften the spectrum. A larger core would also allow for smaller linear power requirements on the fuel assemblies, which would decrease peak fuel temperatures. But enlarging the core would be moving away from the desirable characteristics of fast reactors: high power densities and hard spectra to improve breeding and burning characteristics. Another potential change to the Metal core design would be a shorter and wider 'pancake' core, which would improve the coolant thermal expansion reactivity feedback but this could introduce other thermal hydraulic issues. A flatter core coupled with efforts to move the peak power generation radially outward would help compensate against the significant spectral hardening term that leads to such a positive coolant reactivity feedback effect. As the reactivity feedback associated with bowing of the fuel was not addressed in these calculations, with careful design of the structure constraining the fuel assembly ducting, a negative reactivity feedback could be induced that, while smaller than other feedbacks, could improve the overall performance of the Metal core due to its larger thermal expansion coefficient.

While the Nitride and Oxide cores performed remarkably and similarly well in all transients, the Nitride core established its superiority in the Unprotected Transient Over-Power Accident due to the larger margin to fuel melting. But experience with Nitride fuels is very limited and as of now, research has not determined the optimum N^{15} enrichment levels that would appropriately balance the Doppler feedback, C^{14} generation and economic issues associated with Nitride fuel production. Oxide fuel technology is much more advanced with fabrication techniques that have been in effect for several decades. While the Nitride S-PRISM core performed best in the transients

simulated with regard to the given failure criteria, the Oxide S-PRISM core is a more realistic option with nearly comparable safety characteristics.

7.2 Recommendations for Future Investigations

The conclusions presented in this reserach should be viewed with the understanding that there are important Fast Reactor transient phenomena that RELAP5-3D is unable to simulate, with its main limitation being events beyond fuel or clad melting. During the low probability accidents that initiate core melting, these events would not be the end of the transient. It is possible for molten cladding to be carried upwards into cooler areas of the core where it can resolidify and block coolant flow. Because of its high melting temperature, Oxide fuels that have melted may also be carried to cooler regions of the core and resolidify. If coolant flow is blocked, the remaining molten fuel will fall towards the lower plenum where it presents recriticality risk. [47]

Metal fuel will act differently at temperatures exceeding its melting temperature. At these elevated temperatures, liquid Metal fuel that comes into contact with the cladding will form new alloys with melting temperatures below the coolant boiling temperature. Because of the relatively low melting temperature of the new fuel-cladding material, resolidification in the upper areas of the core will not occur. Not only is coolant flow not blocked, but the dispersion of fuel limits recriticality risk. [47]

Due to its very high melting temperature, Nitride fuels take much longer to melt, eliminating the possibility of fuel dispersion to counteract the transient. In the case of the unprotected transient over-power accident, the Nitride core was able to avoid fuel or clad melting until core power reached 6,000 MWt. By this point the Metal core would have experienced significant enough melting to distribute fuel in a geometrically favorable way and decrease reactivity permanently. Without this early counter to extreme transients, accidents in Nitride cores may continue beyond desirable core

states.

While these fuel and clad relocation simulations are difficult to accurately model, especially in extreme cases, it is something that needs to be addressed for the S-PRISM transient simulations. RELAP5-3D was initially intended for light water reactor analysis; other thermal hydraulics codes [30] were created specifically for liquid metal reactor simulations. Beyond fuel and clad relocation, there are several capabilities not available within RELAP5-3D that would improve the calculations presented in this study. For example, there is limited sodium vapor data available within RELAP5-3D. Severe tranisents will require this data. The ability to calculate individual reactivity feedbacks instead of a lumped fuel and lumped coolant feedback would allow for more detailed analyses of the events occurring during transient scenarios. The conclusions presented in this study based on the assumption of fuel or clad melting as the failure criteria in S-PRISM are a valid first calculation. However, further work is required to simulate these transients more accurately, not just prior to melting, but after as the S-PRISM core undergoes drastic changes.

REFERENCES

[1] "American national standard for decay heat power in light water reactors, ANSI/ANS-5.1-94," tech. rep., August 1994.

[2] "Technical bulletin: incoloy alloy ma956." Special Metals Corporation, 2004. http://www.specialmetals.com/documents/Incoloy%20alloy%20MA956.pdf , February 2010.

[3] "Generation IV technology: Systems," April 2009. http://www.gen-4.org/Technology/systems/index.htm.

[4] "IAEA fast reactor database," April 2009. http://www-frdb.iaea.org/index.html.

[5] "NEA-1683: ERANOS 2.0, Modular code data system for fast reactor neutronics analyses," April 2009. http://www.nea.fr/abs/html/nea-1683.html.

[6] "RELAP5-3D home page," April 2009. http://www.inl.gov/relap5/.

[7] A. E. Dubberley, e. a., "SuperPrism metal core margins to severe core damage," *Proceedings of ICONE 8: 8th International Conference on Nuclear Engineering*, April 2000.

[8] Boardman, C. E., "A description of the S-PRISM plant," *Proceedings of ICONE 8: 8th International Conference on Nuclear Engineering*, April 2000.

[9] Boardman, C. E., "Optimizing the size of the Super-Prism reactor," *Proceedings of ICONE 8: 8th International Conference on Nuclear Engineering*, April 2000.

[10] Carmack, W. J., "Metallic fuels for advanced reactors," *Journal of Nuclear Materials*, vol. 392, pp. 139–150, 2009.

[11] CEA, *ERANOS 2.0 Documentation du code*.

[12] D. C. Wade, e. a., "The safety of the IFR," *Progress in Nuclear Energy*, vol. 31, pp. 63–82, 1997.

[13] Dubberley, A. E., "SuperPrism oxide and metal fuel core designs," *Proceedings of ICONE 8: 8th International Conference on Nuclear Engineering*, April 2000.

[14] Dubberley, A. E., "Transient Performance of S-PRISM," *Proceedings of ICONE 9: 9th International Conference on Nuclear Engineering*, April 2001.

[15] Hummel, H. H., *Reactivity Coefficients in Large Fast Power Reactors*. Hinsdale, Ill.: American Nuclear Society, 1970.

[16] Idaho National Laboratory, Idaho Falls, ID, *RELAP5-3D Code Manual Volume I: Code Structure, Systems Models, and Solution Methods*, June 2005.

[17] J. K. Fink, e. a., "The enthalpy and heat capacity of solid UO_2," tech. rep., Argonne National Laboratory, Downers Grove, Illinois, May 1981.

[18] James J. Duderstadt, L. J. H., *Nuclear Reactor Analysis*. New York: Wiley, 1976.

[19] Jin Sik Cheon, e. a., "Sodium fast reactor evaluation: core materials," *Journal of Nuclear Materials*, vol. 392, pp. 324–330, 2009.

[20] Kawakita, T., "Feasibility study on nitride fuel core and recycling system toward self-consistent nuclear energy system," *Progress in Nuclear Energy*, vol. 40, pp. 597–606, April 2002.

[21] Kittel, J., "History of fast reactor fuel development," *Journal of Nuclear Materials*, vol. 204, pp. 1–13, Sept 1993.

[22] Kurosaki, K., "A molecular dynamics study on uranium-plutonium mixed nitride," *Journal of Alloys and Compounds*, vol. 319, pp. 253–257, 2001.

[23] Kwant, W. and Boardman, C., "Prism-Liquid metal cooled reactor plant design and performance," tech. rep., General Electric Company, San Jose, California, Sept 1990.

[24] Leo G. LeSage, e. a., "Current status of fast reactor physics reactivity coefficients," *Progress in Nuclear Energy*, vol. 16, pp. 231–250, 1985.

[25] Martin, D. G., "A re-appraisal of the thermal conductivity of UO_2 and mixed (U,Pu) oxide fuels," *Journal of Nuclear Materials*, vol. 110, pp. 73–94, 1982.

[26] Meneghetti, D. and Kucera, D. A., "PRD components of a homogeneous U10Zr-fueled 900 MWt LMR: CONF-880506–15," tech. rep., Argonne National Laboratory, Argonne, Illinois, May 1988.

[27] Muta, H., "Thermal and mechanical properties of uranium nitride prepared by SPS technique," *Journal of Nuclear Materials*, vol. 43, pp. 6429–6434, Oct. 2008.

[28] R. Gajapathy, e. a., "Thermal hydraulic investigations of intermediate heat exchanger in a pool-type fast breeder reactor," *Nuclear Engineering and Design*, vol. 238, pp. 1577–1591, 2008.

[29] R. L. Klueh, e. a., "Ferritic/martensitic steels - overview of recent results," *Nuclear of Nuclear Materials*, vol. 307–311, pp. 455–465, 2002.

[30] Reactor Analysis Division, Argonne National Laboratory, Argonne, IL, *The SAS4A/SASSYS-1 LMR Analysis Code System*, August 1996.

[31] RIMPAULT, G., "Algorithmic features of the ECCO cell code for treating heterogeneous reactor subassemblies," tech. rep., International Conference on Mathematics and Computations, Reactor Physics and Environmental Analyses, Portland, OR, May 1995.

[32] RIMPAULT, G., "The ERANOS code and data system for fast reactor neutronic analyses," tech. rep., Proceedings of the International Conference PHYSOR 2002, Seoul, Korea, October 2002.

[33] Ruggieri, J., "ERANOS 2.1: International code system for GEN IV fast reactor analysis," tech. rep., Proceedings of the 2006 International Congress on Advances in Nuclear Power Plants, ICAPP '06, Reno, NV, June 2006.

[34] Smith, M. A., "Low conversion ratio fuel studies, ANL-AFCI-163," tech. rep., Argonne National Laboratory, Downers Grove, Illinois, January 2006.

[35] Steiner, H., "The begin-of-life-behaviour of fast breeder reactor fuel pins: Irradiation tests and verification of restructuring models," institut fur material-und festkorperforschung, Transactions of the 7th International Conference on Structural Mechanics in Reactor Technology, Downers Grove, Illinois, August 1983.

[36] Steven B. Ross, e. a., "Thermal conductivity correlation for uranium nitride fuel between 10 and 1923 K," *Journal of Nuclear Materials*, vol. 151, pp. 313–317, 1988.

[37] Streit, M., "Nitrides as a nuclear fuel option," *Journal of the European Ceramic Society*, vol. 25, no. 12, pp. 2687–2692, 2005.

[38] Su'ud, Z., "Neutronic performance comparation of MOX, nitride and metallic fuel based 25-100 MWe Pb-Bi cooled long life fast reactors without on-site refueling.," *Progress in Nuclear Energy*, vol. 50, pp. 276–278, March 2008.

[39] T. C. Chawla, e. a., "Thermophysical properties of mixed oxide fuel and stainless steel type 316 for use in transition phase analysis," *Nuclear Engineering and Design*, vol. 67, pp. 455–465, 1981.

[40] Takano, H., "A concept of nitride fuel actinide recycle system based on pyrochemical reprocessing," *Progress in Nuclear Energy*, vol. 32, no. 2–4, pp. 373–380, 1998.

[41] Takano, H., "Symbiosis system for transmutation on nitride fuel FBR and ADS," *Progress in Nuclear Energy*, vol. 40, pp. 473–480, April 2002.

[42] Tanaka, K., "Fission gas release and swelling in uranium-plutonium mixed nitride fuels," *Journal of Nuclear Materials*, vol. 327, pp. 77–87, May 2004.

[43] Tentner, A. M., "Severe accident approach: Final report evaluation of design measures for severe accident prevention and consequence mitigation: ANL-GENIV-128," tech. rep., Argonne National Laboratory, Argonne, Illinois, March 2010. http://www.ipd.anl.gov/anlpubs/2010/01/65912.pdf.

[44] Todreas, N. E. and Kazimi, M. S., *Nuclear Systems II: Elements Of Thermal Design*. Reading, Massachusetts: Taylor & Francis, 1990.

[45] W. M. Stacey, e. a., "Advances in the sub-critical, gas-cooled, fast transmutation reactor concept," *Nuclear Technology*, vol. 159, pp. 72–105, July 2007.

[46] Waltar, A. E. and Reynolds, A. B., *Fast Breeder Reactors*. New York: Pergamon Press, 1981.

[47] Wigeland, R. and Cahalan, J., "Fast reactor fuel type and reactor safety performance," *Proceedings of Global 2009*, September 2009.

[48] Williford, R., "Compliance characteristics of cracked UO_2 pellets," battelle pacific northwest laboratories, Transactions of the 7th International Conference on Structural Mechanics in Reactor Technology, Downers Grove, Illinois, August 1983.

[49] Winter, M., "WebElements periodic table of elements: Uranium: Uranium nitride," April 2009. http://www.webelements.com/compounds/uranium/uranium_nitride.html.

[50] Y. Arai, e. a., "Dependence of the thermal conductivity of (U,Pu)N on the porosity and plutonium content," *Journal of Nuclear Materials*, vol. 195, pp. 37–43, April 1992.